UCLouvain

epl

École polytechnique de Louvain

Ultra-low-power miniaturized vagus nerve sensing platform for treating refractory epilepsy

Author: **Louise Coppieters de Gibson**
Supervisor: **David Bol**
Readers: **Laurent Françis, Rémi Dekimpe**
Academic year 2019–2020
Master [120] Electrical Engineering

Abstract

Epilepsy is a disease that concerns 50 million people worldwide and can lead to severe complications in everyday life. One third of the epileptic patients cannot be cured with anti-seizure drugs. For those patients an alternative consist in stimulating the vagus nerve to lower the seizure frequency. Using neural data to detect the seizure onset can considerably improve the impact of the vagus nerve stimulation. The innovation of this study is to propose a digital implementation of the adaptive tripole to recover the neural signal with a microcontroller. Besides, the analog amplification level in front of the microcontroller is designed in order to match with the biological signal specifications. Tracks are given to further improve the performances of the system and consequently enhance the impact of vagus nerve stimulation for epileptic patients or for other peripheral nerve recording applications.

List of Abbreviations

ADC Analog to Digital Conversion

ASD Antiseizure drugs

AT Adaptive Tripole

CNS Central Nervous System

DAC Digital to Analog Conversion

DBS Deep Brain Stimulation

DMA Direct memory access

ECoG Electrocorticogram

EEG Electroencephalogram

EMG Electromyogram

ENG Electroneurogram

IA Instrumentation amplifier

LFP Low Field Potentials

LSB Least significant bit

MSI RC mode Multispeed internal resistance capacitor (oscillator) mode

NT Neurotransmitters

PNS Peripheral nervous system

QT Quasi Tripole

SAR Successive Approximation Register

TT True tripole

UART Universal asynchronous receiver-transmitter

VCORE Core voltage of the microcontroller

VENG Vagus nerve electroneurogram

VNS Vagus nerve stimulation

Contents

Introduction

Epilepsy is a disorder caused by disturbed electrical rhythms in the central nervous system (CNS)[1]. Typical symptoms are convulsions, blackouts and uncontrolled jerking movements who can lead to severe complications in everyday life. A seizure can be the origin of a car accident, it can lead to complications during pregnancy and those suffering from epilepsy are more likely to suffer from psychological troubles such as depression, anxiety or suicidal thoughts [2]. Epilepsy concerns about 1% of the worldwide population [3]. Two third of those patients can be cured with antiseizures drugs (ASD), but one third of epileptic persons suffer from **refractory epilepsy** (also called drug-resistant epilepsy) [4]. For those patients doctors try to find alternative solutions to lower the frequency of the seizures. Since the seizures are due to disturbed electrical rythms, doctors found out that stimulating the disturbed brain area can stop a seizure. The brain can directly be stimulated through deep brain stimulation (DBS) and the vagus nerve, a nerve that is directly connected to the brain (cranial nerve), can be stimulated through vagus nerve stimulation (VNS) [5].

Stimulation can be regulated with an open loop (without taking the start of seizures into account) or with a closed loop (by stimulating when the initiation of a seizure is detected). Closed loops, also called feedback loops, are already subject of research for DBS [6], while VNS applications mainly works in open loop. In some VNS applications heart rate information is used to detect the start of a seizure. In some cases, the heart rate of the patient increases at the start of a seizure, this phenomenon is called ictal tachycardia. The heart rate can thus be extracted and be used for seizure detection. This technology is already used in commercialised VNS systems [7, 8].
The interesting part of the feedback loop is to stimulate when the initiation of a seizure is detected. In order to achieve this, the neural signal has to be recorded. **Neural signal recording** concerns as well the brain as peripheral nerves. For the brain, multiple possibilities exist and such as the electroneurogram (EEG), the electrocorticogram (ECoG) and the implanted electode arrays. Concerning the peripheral nerve the main issue is the the very low signal-to-interference value. The neural signal has an amplitude in the μV-range while the artefacts (mainly due to the surrounding muscles, the heart beats and the breath) are in the mV-range. Extracting the neural signal information out of the measured signal is consequently a huge challenge.

Recently (2020), a method to record vagus nerve electroneurogram (VENG)

and detect induced seizures with a **true tripolar cuff electrode** has been studied [9]. A tripolar cuff electrode is a cuff electrode with 3 equidistant electrodes. The main advantage of this type of electrode, besides being non-invasive with respect to the nerve and suited for long term implants [10, 11], is the linearization of the surrounding artefacts. Combined with a tripolar model design, those artefacts can be removed or considerably be lowered. In [12, 13] three tripolar model designs are presented: the quasi tripole (QT), the true tripole (TT) and the adaptive tripole (AT). The QT and TT are both implementations with fixed gains while the AT takes the **cuff imbalance** into account. The cuff imbalance is a general term that includes all non-idealities linked to the cuff. The specificity of the AT implementation, the gains of the neural amplifiers are modified in function of those cuff imbalances.

In [12, 13] an analog implementation of this adaptive tripole is presented. The inovation brought in this master thesis is the **digital implementation** of the adaptive tripole on a STM32L073 Nucleo Board [14]. The signals are first acquired and sampled with two analog-to-digital converters (ADC). The data is then transferred with a direct memory access (DMA) to a buffer in memory. The DMA launches interrupts when the buffer is half or completely filled. Those interrupts are called callbacks and execute automatically the corresponding callback function. The cuff imbalance is computed in those callback functions and the recorded ADC values are then combined with adapted gains to retrieve the neural signal. This signal is stored in an output buffer which can be accessed either by connecting a DAC or UART peripheral through the DMA.

To acquire the signal with the micro-controller, the cuff electrode differential signal must be **amplified**. The supply voltage of the micro-controller has been fixed at 1.8 V. The ADC values are coded on 12 bits, this means that one least significant bit (LSB) unit has an amplitude of 0.4mV. While the amplitude of measured artefact signal between tho electrodes is typically around 100 μV (based on [13]) and the neural signal in VENG are typically around 5.5 +/- 0.2 μV and 11.4 +/- 3.1 μV depending on the type of recording [9]. The signal must consequently be considerably amplified. The amplification is done through 2 instrumentation amplifiers (IA): a custom integrated differential IA previously designed in the ECS group at UCLouvain (integrated IA) and an IA built using discrete components (discrete IA). This second IA implements two high-pass filters in order to remove a part of the cardiac, muscular and breath artefacts. After those two IA, a second order Sallen-Key low-pass filter is added to remove the high-frequency noise.

Concerning the **measures and results**, the tests on the IA built using discrete components as well as the low-pass Sallen-Key filter have been performed separately. Due to the Covid-19, the tests concerning the retrieving of the neural signal could not be performed on the STM32 Nucleo board, since only one waveform generator was available. The global system has thus been simulated on matlab.

The obtained performances of the system blocks and simulation can be summarized in the following items:

- The total **gain** of the analog amplification is $4.77 \cdot 10^3 V/V$ composed of:
  - Integrated IA gain: 63.8 V/V
  - Discrete IA gain: 75 V/V
- The **bandwith** goes from $159Hz$ to $13.4kHz$
- The **input referred noise** is $2.5\mu V_{RMS}$
- The total **power consumption** is 3.8 mW composed of:
  - Microcontroller power consumption: 2.59 mW
  - Discrete IA + Sallen-Key power consumption: $2 \cdot 0.28mW$
  - Integrated IA power consumption: $2 \cdot 0.023mW$
- The **signal-to-interference ratio** (SIR_{out}) simulation output ratio is of 4 dB.

This master thesis is divided in 5 chapters: **Chapter 1** gives an overview about refractory epilepsy, the anatomy of the nervous system and the available treatments to cure epilepsy. **Chapter 2** gives a state of the art concerning the neural signal recording in the brain and of the vagus nerve and stimulation of the vagus nerve. It also introduces the different kind of electrodes and more particularly the cuff electrode. **Chapter 3** details the different tripolar model designs and gives more explanations about the cuff imbalance in the context of the adaptive tripole model. The digital implementation of the adaptive tripole model on the microcontroller is described in the second part of Chapter 3. **Chapter 4** details the different amplification levels and more specifically the discrete IA. Finally, **Chapter 5** contains the measures obtained on the micro-controller and the discrete IA, the global system simulations, a comparison with other similar works and a discussion of the obtained results.

Chapter 1

Epilepsy: an overview

Worldwide, about 50 million people are concerned by epilepsy [3]. In Belgium, the prevalence of epilepsy is around 1% (0.9% in 2010 and 1.1% in 2014) [15]. Among those patients, more than 30 percent suffer from refractory epilepsy, i.e. they can not control the epileptic seizures with drug therapy [4]. Epilepsy is defined by the occurrence of several seizures in a given time-lapse [16, 17]. Refractory epilepsy is the most difficult type of epilepsy to cure and increases the risk of structural damage to the brain. Moreover it also increases the risk of comorbidity and mortality as well as psychological, educational, social and vocational disorders [18].

This chapter first gives a brief explanation about epilepsy (symptoms and causes) and details the specific case of refractory epilepsy. Then the anatomy of the nervous system is developed and finally an overview of the available treatments to cure epilepsy is presented.

1.1 Symptoms, causes and the specific case of refractory epilepsy

1.1.1 Symptoms

The symptoms linked to refractory epilepsy vary from person to person. Seizures can affect any process coordinated by the brain, but the symptoms are often linked to the brain area where the seizures originates and type of seizure. This is why epileptic patients often have the same type of seizure over time. Typical symptoms are convulsions, blackouts, temporary confusion, uncontrolled jerking movements of arms and legs, etc. [2] Appendix A illustrates typical epicenter-related symptoms. Epilepsy can lead to several complications for the patient himself like falling and drowning, but some complication can also impact the life of others. It can be the origin of a car accident, it can lead to complications during pregnancy and those suffering from epilepsy are more likely to suffer from psychological troubles such as depression, anxiety or suicidal thoughts [2].

1.1.2 Causes

Epilepsy is a disorder caused by disturbed electrical rhythms in the central nervous system [1]. Seizures can be focal (linked to a precise area of the brain) or generalized (involves all the parts of the brain) [2]. Epilepsy has different origins: 40% are symptomatic, caused by a brain injury. 5% to 10 % are idiopathic[1] with a probability of genetic origin. In the other cases, when the origin is presumed, but not certain, the epilepsy is called cryptogenic [2] [16]. Other risk factors increases the risk of epilepsy such as the age, a vascular disease, dementia, brain injuries or infections [2].

1.1.3 Refractory Epilepsy

One third of epileptic patients are resistant to drug treatment. This kind of epilepsy is also called uncontrolled, intractable or drug-resistant epilepsy [5]. Researches analyses different hypotheses to find the origin of some refractory epilepsy (as for example the expression of drug resistant proteins [19]) but doctors still do not exactly know why some patients suffer from refractory epilepsy while other do not.

Nevertheless doctors try to lower the frequency of seizures by prescribing some drug combinations or a special diet. Other methods consist in removing the brain area where the seizures originate or to stimulate either the brain (DBS) or the vagus nerve (VNS) with electrical pulses [5].

1.2 Anatomy: Nervous system

As mentioned in Subsection 1.1.2, epilepsy is a neural disorder. In order to understand the impact of the different treatments to lower the number of seizures, it is useful to first give an overview of the working of the nervous system. The nervous system is divided into two subsystems: the central nervous system (CNS) and peripheral nervous system (PNS) (Figure 1.1). The CNS is composed of the brain and the spinal cord and performs the data processing and storage while the PNS consists of a cluster of nerves carrying afferent (from the PNS to the brain) and efferent (from the brain to the PNS) information between the brain and the different parts of the human body [21]. In the specific case of epilepsy, the seizures are initiated in the brain. They are caused by a temporary disruption in the normal brain

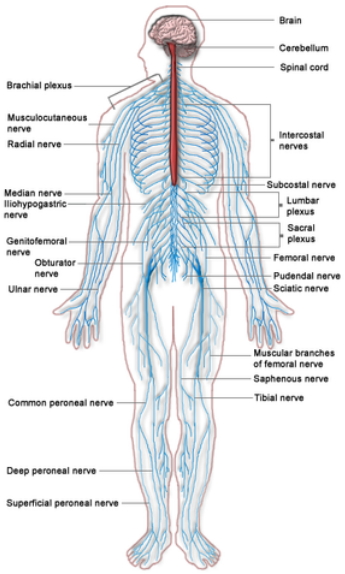

Figure 1.1: *Illustration of the nervous system composed of the CNS (red) and PNS (blue) (Source: [20])*

[1]Idiopathic disease : disease from which the origin is unknown

[2]Cryptogenic disease: disease from which the origin is presumed but not certain

activity and are accompanied by several symptoms such as those presented in Subsection 1.1.1. This disruption creates electrical pulses going from the brain to different parts of the body, depending of the epicentre [22]. The epicentre of the seizures can vary from patient to patient and the epicentre is a determining factor concerning the symptoms. The electrical pulses are conducted by neurons; the building bloc of the nervous system [21].

This section first briefly introduces the neuron and the action potentials. Then, the CNS and PNS are further detailed in the specific context of epilepsy. The brain is further detailed in the CNS subsection and the importance of the vagus nerve in the context of epilepsy is explained in the PNS subsection.

1.2.1 The neuron and action potential

The neuron is the basic structure of the neural network. A neuron consists of a cell body, dendrites and axons and is connected through synapses to other neurons (see Figure 1.3 for the illustration of a neuron). The signals are transmitted by action potentials through the axons. Figure 1.2 details a typical action potential (from inside the cell membrane) and gives an idea of the time lapse of a typical action potential [23].

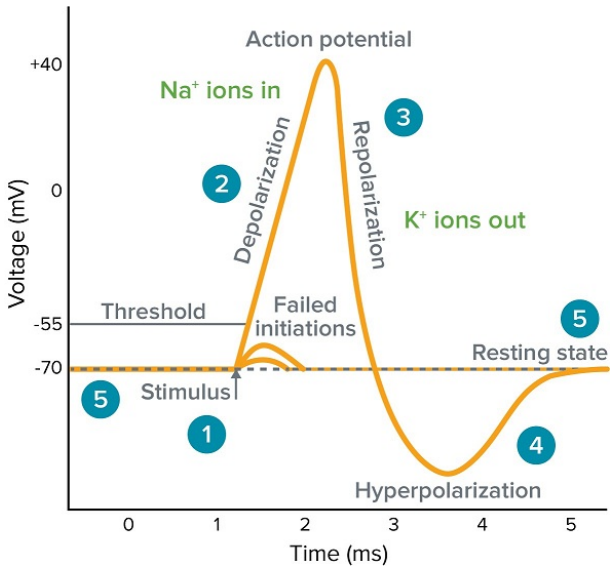

Figure 1.2: *Illustration of an action potential. If the stimulus exceeds a threshold, the neural membrane depolarizes (Na^+ channels are opened and ions flow massively into the cell) the voltage accross the cellular membrane reaches a value up to 40 mV. Then the cell mebrane repolarizes (K^+ channels are opened and K^+ ions flow in their turn massively outside the cell). This depolarizing and repolarizing movement form the typical action potential peak. The typical time lapse of an action potential is around 1ms - 2ms. The action potential is then followed by a refractory period (hyperpolarization). This period is used to rebalance the ion concentrations inside and outside the cell (Source: [24]).*

The ion concentration variation due to an action potential influences the ion concentration of the direct environment. The surrounding membrane potential consequently also reaches the action potential initiation threshold and another action potential is initiated. This procedure generates a flow of action potentials through the axons and transmits neural signals (see Figure 1.3). Due to the refractory period the propagation can only go in the direction where no action potential has occurred. Nerves can be myelinated or not. On Figure 1.3, a myelinated nerve is represented. In myelinated nerves, the action potentials only occur at the nodes of Ranvier [25].

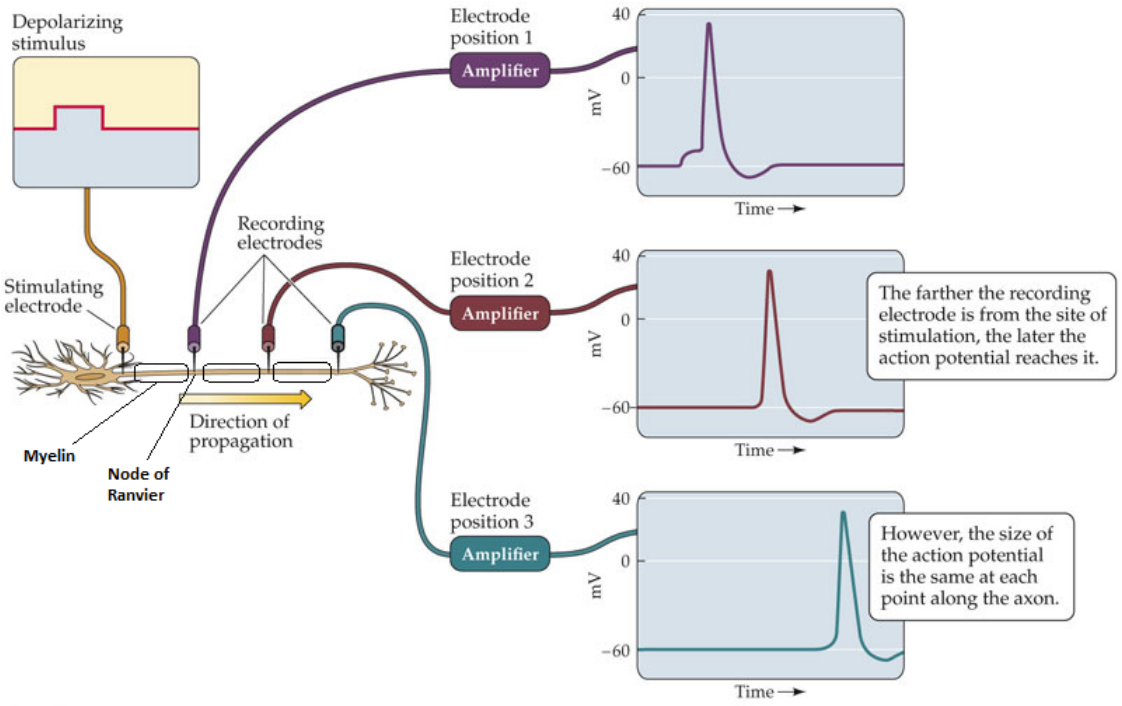

Figure 1.3: *Illustration of the propagation of an action potential through a nerve. As shown on the figure the action potentials are delayed in time depending on the place of the electrode on the nerve (Source: [26]).*

1.2.2 Central nervous system (CNS) - Brain

The CNS is composed of the brain and the spinal cord. The human brain is a huge cluster composed of approximately 86 billion neurons [27]. Neurons are then connected to between 1 and 200 000 other neurons [28]. Those neurons are organised in different areas and layers and they process all the afferent and efferent data. Moreover, they are constantly adapting themselves thanks to neural plasticity and store a lot of data. The complexity of the brain organisation is then further increased

by the inter-individual variations [28].

As mentioned Subsection 1.1.2, seizures are initiated in the human brain. To determine the exact epicenter of the epileptic seizures it is interesting to analyse the way brain signals are recorded.
Taking the complexity of the brain organisation into account, it is quite impossible to measure the action potentials of single neurons inside the brain.

For brain measurements, doctors analyse low field potentials (LFPs) measured with an electroencephalogram (EEG, see Figure 1.4) or an electrocorticogram (ECoG [3]).

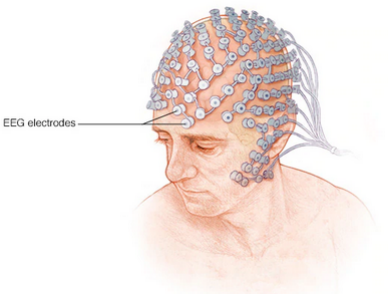

Figure 1.4: *Illustration of the electrode placing of an electroencephalogram (EEG) (Source: [29])*

LFPs are the result of a huge amount of neurons spiking together. The typical frequency range is lower than the frequency range of one action potential, generally, the typical frequency range of LFPs as 1 - 100Hz and the amplitude is in the mV range. Figure 1.5 shows a typical measure of seizure onset. EEG helps to confirm the occurance of a seizure and to determine the epicenter in case of focal epilepsy [16].

Figure 1.5: *Example of typical EEG signals of a seizure onset. The arrow indicates the electrographic ictal onset over the left temporal region (Source: [31]).*

[3] An electrocorticogram measures the neural activity on the surface of the scale while an EEG measures the neural activity on the scalp. ECoG requires the removal of a part of the scull to measure the neural activity. An ECoG is consequently more precise but also more invasive [30]

1.2.3 Peripheral Nervous System (PNS) - Vagus Nerve

The PNS is the system that includes all the nerves of the human body except the brain and the spinal chord. The function of those nerves is to transfer the neural signals from the brain or spinal chord to the different parts of the human body. In the case of an epilepsy, the epicenter of the seizure generates disrupted signals that are send through the nerves to the corresponding part of the body (as illustrated on Figure A.1). On some of those nerves it can thus be possible to detect the start of some seizures. An easily accessible cranial nerve carrying seizure information is the vagus nerve (see Figure 1.6).

Figure 1.6: *Location of the vagus nerve (Source: [32]).*

The vagus nerve consists of 20% efferent and 80% afferent nerve fibers. Efferent fibers send signals from the brain to the human body while afferent fibers (also called sensory fibers) give feedback from the body to the brain [33].

Compared to the CNS, the amount of neurons spiking together in the PNS is much lower. The signals detected on a peripheral nerve is the result of one or a few neurons spiking at the same time [34].

1.3 Available treatments

There exist several traitments agains epileptic seizures. In Belgium, the commonly proposed treatments are: medicine treatment, ketogenic diet, deep brain stimulation, vagus nerve stimulation and surgery [35].

1.3.1 Medicine traitments

The most common approach to treat epilepsy is medication. There exist a large panel of antiseizure drugs (ASD) that lowers the frequency of the seizures or even eradicate them. The choice of medication depends on the nature of the epilepsy and of the previous medical treatments. The effect of medication vary from person to person. If seizures can not be controlled with medication, the neurologist considers often a surgery or VNS. To avoid a too large amount of side effects, doctors often prefer to prescribe a monotherapy (one type of ASD) but some types of epilepsy require a combination of different drugs [36, 35].

1.3.2 Ketogenic diet

A ketogenic diet consists in lowering the ingestion of sugar and proteins and increases the amount of fat. The ketogenic diet is often used to treat a ASD-resistant epilepsy.

The human body then starts to break down fats instead of carbohydrates [36]. This process modifies the metabolism and induces a ketosis: a destruction of fat in the human body. This modification in the metabolism lowers the frequency and intensity of the seizures. This method is effective on young children [35].

1.3.3 Epileptic surgery

Surgery is generally recommended when focal seizures persist despite at least two seizure-specific well-tolerated medications trials or if an identified brain lesion is believed to cause the seizures. Surgery consists in removing the region of the brain that initiates the epileptic seizure. The exacts brain region to be removed is defined by implanted electrodes. Surgeons often avoid to remove brain regions necessary for speech, movements, memory and thinking and every surgery implies a level of risk, but the advantage of surgery is that the patient is more likely to become seizure-free than with any of the other treatments [37, 36].

1.3.4 Deep Brain Stimulation (DBS)

DBS is a treatment where electrodes are implanted deep into the brain as illustrated on Figure 1.7. Besides electrodes, DBS also involves a pulse generator implanted under the skin of the upper chest (same place as a battery for pacemakers). The DBS use mild electrical pulses to control abnormal brain activities [36, 35].

Epilepsy is one of the conditions to be elective for DBS. DBS is often very accurate, but has also a non-negligeable number of risks linked to the electrode implantation into the brain [38].

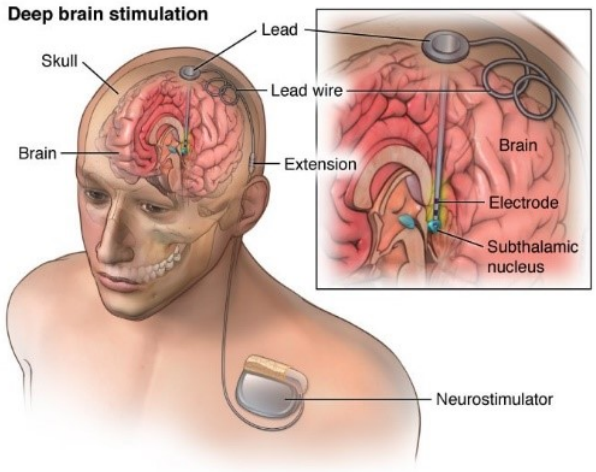

Figure 1.7: *Illustration of deep brain stimulation (Source: [38]).*

1.3.5 Vagus Nerve Stimulation (VNS)

VNS is a therapy that stimulates the vagus nerve in order to prevent epileptic seizures. It is composed of a cuff electrode that wraps around the vagus nerve and a pulse generator placed under the skin of the upper chest (as illustrated on Figure 1.8). VNS

has the advantage to be less invasive than surgery or DBS and is less constraining than a ketonic diet. The VNS device delivers short electrical pulses to the vagus nerve. Since the vagus nerve is a cranial nerve (see Subsection 1.2.3), this signal is directly transmitted to the brain. On average, VNS reduces the number of seizures of 20 % to 40 %. VNS is often combined with some ASD [36, 35].

The exact mechanism of action of the vagus nerve in the case of pharmacoresistance epilepsy remains still unknown. Actually VNS is a system that sends impulses on regular time basis. In [34] findings show that a combination of the VNS with a recording of the vagal nerve compound action potentials may help the medical team to find the optimal intensity for each patient specifically.

This thesis will in the further concentrate about the vagus nerve in the following chapters. In order to have an idea of number of potential patients it is interesting to mention (or recall) the following elements. In Belgium about 100 epileptic patients are implanted with VNS every year, those patients could benefit from the closed loop system measuring the neural activity on the vagus nerve [15]. Worldwide about 50 million people are affected by epilepsy. One third of those patients suffer from refractory epilepsy. Approximately the half of this population can be cured with a surgery, the other half could be treated with a closed loop implant on the vagus nerve [3].

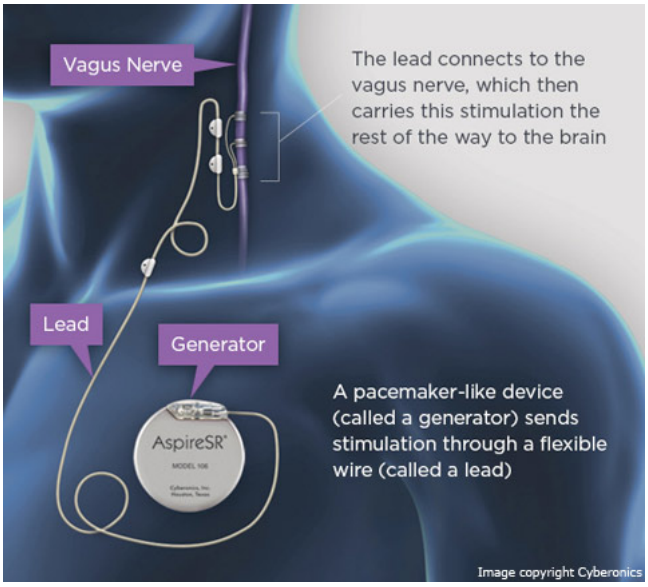

Figure 1.8: *Illustration of the VNS implant proposed by Cyberonics composed of electrodes wrapped around the vagus nerve and a pulse generator (Source: [39]).*

Chapter 2

State of the Art: recording and stimulation

As mentioned in Subsection 1.3.5, VNS is one of the solutions to prevent seizures. The main limitation of VNS This thesis focus on the vagus nerve, more specifically on the recording of the neural activity on the vagus nerve in order to improve VNS treatment.

This chapter gives an overview of the different methods to detect seizures and get more in details concerning the recording of neural activity on peripheral nerves. It gives then an overview about the stimulation of the vagus nerve. Finally a section concludes this chapter by presenting two examples feedback loops to stop seizures.

2.1 Recording

The goal of recording is to capture the neural signal with a high SIR. As seen in previous chapter, the neural signal consists of action potential travelling though the nerves. The interferences, in the specific case of biomedical neural signals, are mainly provoked by the muscles, the cardiac rhythm and the human breath. Those interferences are also called artefacts. The main challenge is to get rid of those artefacts.
A typical recording device is composed of one or several electrodes and a neural amplifier. This subsection gives an overview of the mainly used recording electrodes for neural signals.

2.1.1 Most common cortical and peripheral nerve electrodes

The electrodes recording neural signals can be divided in two groups: the cortical electrodes and the peripheral nerve electrodes.

Cortical electrodes

The most common cortical electrodes are illustrated on Figure 2.1 with the corresponding neural signals: the EEG, ECoG and the LFP spikes. The EEG, as

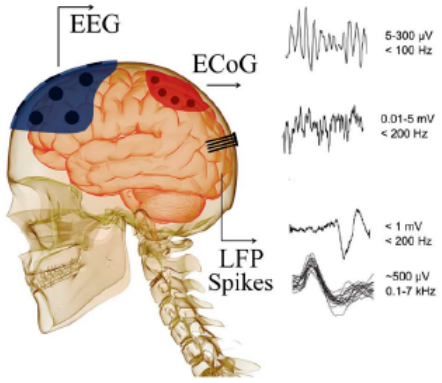

Figure 2.1: *Image illustrating the difference between EEG, ECoG and electrode arrays. (Source: [40])*

presented and illustrated on Figure 1.4 in Subsection 1.2.2 is a non-invasive measure of the brain activity. ECoG is quite similar, but the electrodes are placed under the skull and finally there exist a lot of different implantable electrodes as the electrode arrays, the microwires and multisite probes [40]. The main trade off is to have rather precise signals with a high SNR while not being to invasive. The choice of electrode consequently depends always of the patient and the application.

In the context of epilepsy, cortical recording electrodes are used to detect epileptic activity by combining the recorded signals with specific detection algorithms [41]. Some studies also uses those measures and compare them to other technics as magnetoencephalography [42] to localise the source of the seizures typically for surgery.

Peripheral nerve electrodes

Concerning the recording of peripheral nerves, there exist different types of electrodes. The most common are those presented in Figure 2.2. As shown on the figure, the ideal electrode must not be invasive and must be as much selective as possible, but the selectivity increases with the invasiveness. The different types of electrodes are detailed in the following items :

- **Regenerative or Sieve electrodes** are electrodes that are inserted between two separate parts of a nerve. The nerve is first cut, the electrode is placed between the two parts and the nerve regenerates through microvias in multichannel silicon devices. The devices have integrated cables to ensure an interface with the regenerating nerve [44]. This type of electrode gives consequently very precise signals, but it is the most invasive electrode with respect to the nerve [45].

- **Intrafascicular and Interfascicular electrodes** are inserted inside the nerve bundle. There are two main types of penetrating electrodes: the interfas-

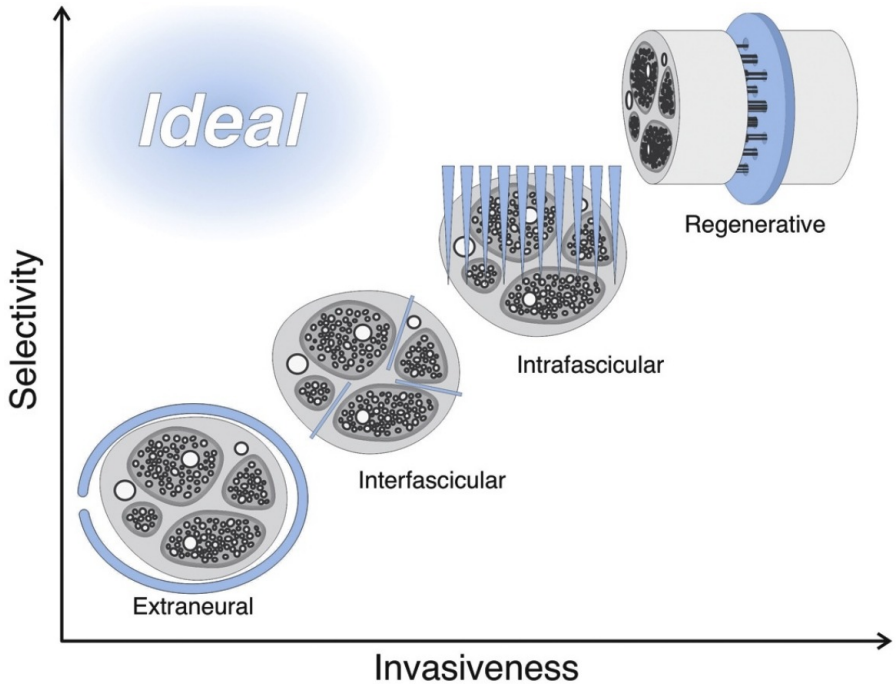

Figure 2.2: *Illustration of the different types of electrodes and ranking in function of the selectivity and invasiveness (Source: [43]).*

cicular and intrafascicular electrodes. The difference lies in the invasiveness with respect to the fascicles [46, 45].

- **The Extraneural or cuff-style electrodes** are electrodes that wrap around the nerve. This kind of electrodes are the less invasive type of peripheral nerve electrode since they do not penetrate the nerve membrane. At the other hand, the signal level is very low (μV_{RMS}) [47, 9, 13]. Having some reference electrodes amplifies the apparent nerve signals and reduces the interference noise if the signal is further combined with a tripolar model design.
  The different types of cuff-electrodes are based on their shape. The typical forms are: cylindrical, helical and FINE (rectangular crossection). The FINE type of cuff-electrode is the most selective of the three because flattening the nerve inside the electrode improves the SNR but is less suited for log term implants [45]. An advantage of the cylindrical and helical cuff electrodes is their suitability for long-term implants [10].

By combining cuff electrodes with a tripolar model, the selectivity will increase while the invasiveness stays the same this

2.1.2 Other epileptic seizure recording possibilities

A lot of alternative methods to neural activity recording have been proposed to detect epileptic seizures. In this section two of them are presented.

Heart rate

Heart rate analysis devices can also be considered to detect seizures. The heart rate changes frequently around the time or even before any other clinical or electrographic sign [48]. Some VNS devices use this characteristic to send supplementary pulses when a seizure is detected by n increasing heart rate [7, 8].

Night watch

The nightwatch is a bracelet placed on the upper arm, detecting epileptic seizures during the night by a combination of heart rate and movement analysis. This combination of heart rate and movement during the night result in a reliable detection of a broad range of seizure. The median sensitivity [1] was around 86%. This multimodal sensor showed better results than a more classical bed sensor [50].

2.2 Stimulation

Stimulation is used in two of the different available treatments for epilepsy: DBS and VNS. This master thesis analyses more specifically the recording of signals in order to stimulate the vagus nerve. This is why this section only gives a brief explanation of VNS.

Peripheral nerve stimulation consists in sending electrical pulses to the nerves by the use of electrodes. Those pulses can either act as neurostimulator (stimulate fibers) or neuromodulators (modulate the neural activity). In the case of epilepsy, the pulses act as neuromodulator. The VNS consist of two main parts: a pulse generator and the electrodes. In some applications, additionaly, an external remote control can also be connected to the implantes pulse generator to adapt the pulse amplitude or frequency [25, 8].

The **pulse generator** as shown on Figure 2.3 encapsulates a battery and some electronics who regulates the electronic pulses. For VNS, the pulse generator is implanted under the upper chest skin. The device must be biocompatible, power efficient and maintain a stable stimulation current over a couple of years [25].

Stimulation electrodes as shown on Figure 2.3 have some requirements in order to reduce as much as possible the charge accumulation. Firstly: they must be perfectly polarizable. This implies a capacitor-like movement of charges, there is no transfer of charges, but rather a charge displacement inside the biologic tissue. Two other typical element required in stimulation electrodes are the decoupling capacitor and the discharge resistor [25].

[1] "*Sensitivity measures how often a test correctly generates a positive result for people who have the condition that's being tested for (also known as the "true positive" rate). [...] Specificity measures a test's ability to correctly generate a negative result for people who don't have the condition that's being tested for (also known as the "true negative" rate).*"[49]

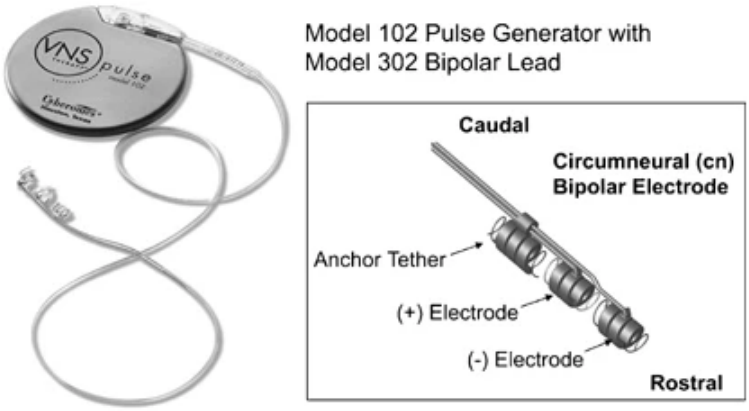

Figure 2.3: *Illustration of a VNS therapy electrode. The electrodes have a helical structure to wrap around the nerve. There are 3 electrodes: a negative electrode, a positive electrode and a anchor tether to maintain the electrodes on the right place. The electrode is connected to a pulse generator who is implanted under the upper chest skin. This specific example is used for VNS (Source: [51])*

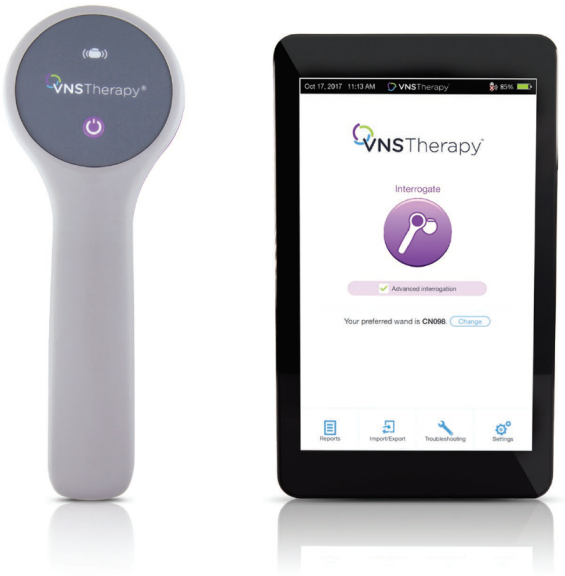

Figure 2.4: *Illustration of the external remote control of Sentiva (a typical VNS system). The left image is the programming wand and the right image is the programmer. This external remote control is compatible with different pulse generators and has different modes: a normal mode with a specific stimulation pattern, a magnet mode with on-demand stimulation and an auto-stimulation mode that depends on the hart rate and is combined with the normal mode. The parameters can be modified on the programmer and the information is sent to the pulse generator via the programming wand (Source: [8])*

An **external remote control** can be added to the system to tune the parameters such as current intensity, stimulation frequency, impulse duration and the duration of stimulation cycles once the device is implanted [34, 37]. An illustration of an external remote control used for VNS is shown on Figure 2.4.

2.3 Closed loop systems

The main idea of the closed loop is to combine the seizure detection and stimulation of the brain or the vagus nerve in one device.

Researches on closed loops between the recording of the brain activity and the stimulation of the brain is already subject of several researches since a couple of years [52]. In [6], for example, a 16-channel implantable seizure control with an intracranial EEG (ECoG) for the signal recording combined with an intracranial biphasic pulse delivery to stop the detected seizures is proposed. In january 2020 the first DBS neurostimulator system with BrainSense technology was accepted by the CE (Conformité Européenne) [53]. In june, this technology has also be approved by the Food and Drug Administration (FDA) to commercialise this technology also in the united states [54]. This technology has 16 independently regulated stimulator channels and 6 noise-limiting sensing channels [55].

Concerning the vagus nerve, the idea to make a closed loop is still at the research stage. Very recently (2020), searchers of UCLouvain studied the feedback loop on the vagus nerve and got concluding results [9]. The neural activity recording was done using a true tripolar cuff electrode. The tripolar design removes an important part of the artefacts and consequently increases the signal-to-interference ratio (SIR). This master thesis further analyses the different tripolar model designs and proposes a digital implementation on a micro-controller of the adaptive tripole.

Chapter 3

Tripolar design and digital implementation

As mentionned in Subsection 2.3, combining a cuff electrode with a tripolar model increases the SIR while keeping a non-invasive electrode w.r.t. the nerve (the main challenge being the recording of neural signals cf. Section 2.1). The purpose of this master thesis is to adapt the tripolar model design presented in [12, 13] on a digital microcontroller in order to reduce the power consumption and the implant size.

This chapter is divided in two main sections: the first section details the tripolar cuff model and more particularly the adaptive tripole taking the cuff imbalance (X_{imb}) into account. The second section proposes a digital implementation of an adaptation of the adaptive tripole on a microcontroller.

3.1 Tripolar model

The tripolar model is composed of two main parts: the tripolar cuff electrode and the tripolar model design. The cuff electrode subsection first details the ideal cuff model and then gives an overview of the several sources of cuff imbalance. In the tripolar model design, the approach of [13] is presented and gives a solution to the problem of cuff imbalance.

3.1.1 Cuff electrode

A cuff electrode as already presented in Section 2.1 is an electrode that wraps around a peripheral nerve as illustrated in Figure 3.1. Studies showed that cuff-electrodes are appropriate for long-term implants [10, 11]. They are stable and non-invasive w.r.t. the nerve. Moreover, cuff electrodes are already used in VNS applications [8].

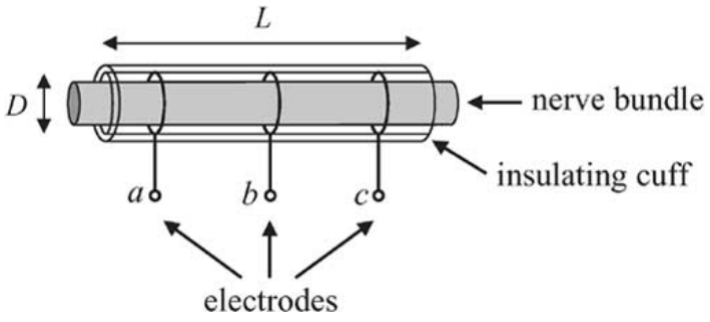

Figure 3.1: *Illustration of a tripolar cuff electrode around a nerve bundel (Source: [56]). The notation of the 3 different connexion points will be a, b and c along the following chapters of this thesis.*

The main disadvantage of the cuff electrode is the very small measured signal amplitude. Inside a neuron (in the axon) the membrane potential varies of approximatively 110mV during an action potential (from -70mV to 40mV cf. Figure 1.2). The problem is that the amplitude decreases with a factor R^2 for an increasing radius R [47]. Besides, to avoid neuropathy, the inner cuff diameter must be 20% larger than the nerve bundel [57]. Cuff electrode signals are consequently in the μV range. In [47] the maximum pulse amplitude obtained for a cuff electrode with a minimal length of 28mm and a diameter of 1 mm is $\approx 1.7\ \mu V$. In a cuff shorter than 28mm, the measured amplitude decreases, while using a longer cuff does not change the results. The main challenge is thus to extract the neural signal (μV range) from the artefacts (mV range).

Ideal cuff model

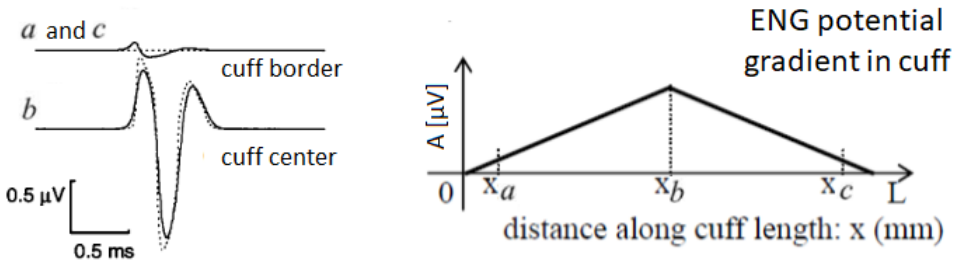

Figure 3.2: *Representation of the signals measured at the electrode connection points a, b and c of Figure 3.1. The signals on the left (Source: [47]) represent the neural signal measured at the border and at the center of the cuff. The Figure on the right represent the amplitude of the neural signal in function of the distance along the cuff (Source: [13, 58]).*

The information is transferred along the nerves by the propagation of action potentials as explained in Subsection 1.2.1. Those action potentials have a constant amplitude along the axon. Inside the cuff, the electrode measures a weighted sum of the action potentials. As shown in Figure 3.2, the measured amplitude of the neural signal at

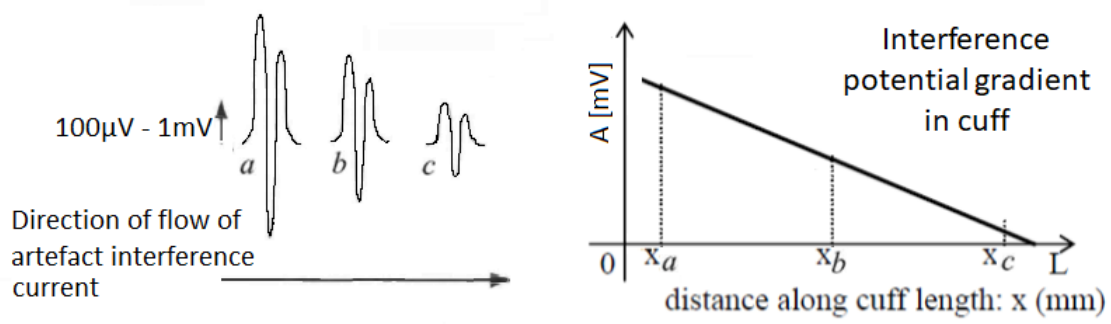

Figure 3.3: *Illustration of the effect of the linearization of an electrical field inside a cuff electrode (Source: [59]). The signals on the left (Source: [12]) represent the artefact signal measured at the three electrode connexion points of the cuff. The Figure on the right represent the linear potential gradient of the artefact signal in function of the distance along the cuff (Source: [13]).*

the central electrode is much more important than the measured amplitude at the borders of the electrode [12].

The artefacts are due to external sources to the cuff electrode. On the vagus nerve, the muscular, cardiac and breath artefact are the main artefacts. The electrode has a linearization effect on those external signals as illustrated in Figure 3.3. If the tripolar cuff electrode is considered as perfect, the distance between the electrodes a and b must be the same as between electrodes b and c. Assuming also the nerve and the cuff electrode as perfectly homogenous and the neural signal as negligeable, the following relation holds:

$$V_a - V_b = V_b - V_c \tag{3.1}$$

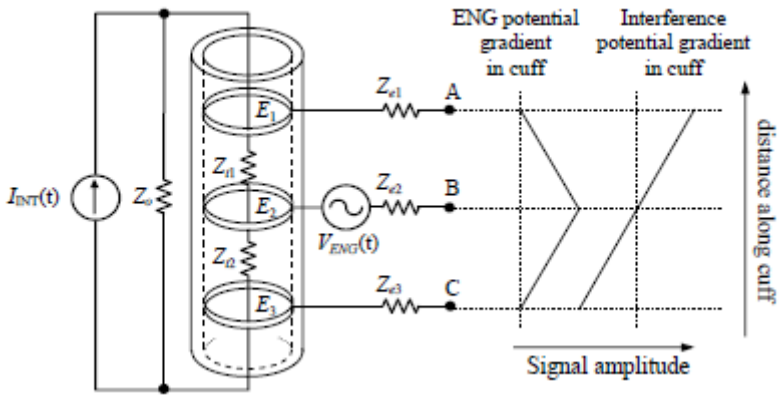

Figure 3.4: *Illustration of the ideal tripolar cuff model. This image summarises the neural signal behaviour inside the cuff (Figure 3.2) as wel as the interfering artefacts from outside the cuff (Figure 3.3). Z_0 represents the tissue impedance outside the cuff. Z_{t1} and Z_{t2} represent the impedance between the middle and the corresponding border electrodes. In this ideal model, Z_{t1} and Z_{t2} are assumed to be equal ($Z_{t1} = Z_{t1} = Z_t$) as well the distance between electrode connection points A and B and the electrode connection points B and C (Source: [13]).*

The advantage of the tripolar cuff electrode is the linearization effect on the potential field inside the cuff. Using this characteristic, the artefact signals can be subtracted with a tripolar model and to only the neural signal are kept. Figure 3.4 summarises the behaviour of the neural and artefact signal in order to get a overall view before the analyse of the cuff imbalances and the tripolar model design.

Cuff Imbalance

The real model must take the non-idealities linked to the cuff electrode into account. Those non-idealities are called cuff imbalances, introduced by [13]. Imbalance is due to cuff asymmetry, tissue growth of the nerve inside the cuff, border effects of the cuff electrode [60] and the proximity and the orientation towards the dipole artefact source [13]. The model of the artefact effect has to be adapted. Figure 3.5 shows how the different sources of imbalance affect the artefact linearization.

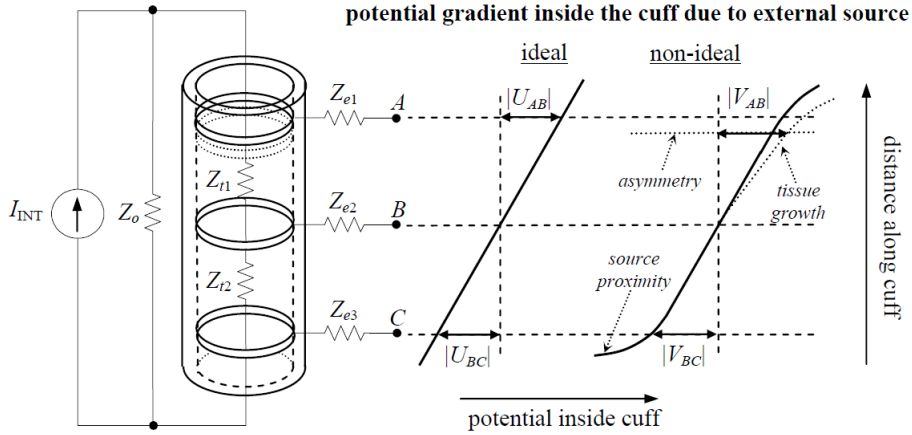

Figure 3.5: *Cuff linearization taking the cuff assymetry, the source proximity and the tissue growth into account [13]. The notations U_{AB} and U_{BC} stand for the voltage differences between the electrodes A and B and between the electrodes B and C respectively with the ideal cuff consideration, while V_{AB} and V_{BC} consider the same voltage differences with the non-ideal cuff consideration.*

Severa studies have been proposed without dealing with cuff imbalance as for example blind source separation (PCA and ICA), but the results were not satisfying [61]. To take the sources of imbalance into account, the concept of cuff imbalance is introduced in [13]. Following the notation of Figure 3.5, the ideal model considers:

$$|U_{AB}| = |U_{BC}| = 0.5|U_{AC}| \tag{3.2}$$

Taking the sources of imbalance into account, equation (3.2) is not valid anymore, the impedances between the pairs of electrodes are not exactly the same: $Z_{t1} \neq Z_{t2}$. Z_{t1} and Z_{t2} are expressed in function of their mean, Z_t, and the cuff imbalance, X_{imb}, in the following equations:

$$Z_t = 0.5(Z_{t1} + Z_{t2}) \quad (3.3)$$
$$Z_{t1} = 0.5(1 + X_{imb})Z_t \quad (3.4)$$
$$Z_{t2} = 0.5(1 - X_{imb})Z_t \quad (3.5)$$

Thanks to equations (3.3) to (3.5), the cuff imbalance, X_{imb}, can be expressed as [13]:

$$X_{imb} = \left[\frac{Z_{t1} - Z_{t2}}{Z_t}\right] \quad (3.6)$$

X_{imb} can further be expressed in function of the different in function of the electrode connection point voltages (V_A, V_B and V_C) [13], one has:

$$X_{imb} = \frac{|V_A - V_B| - |V_B - V_C|}{|V_A - V_B| + |V_B - V_C|} \quad (3.7)$$

3.1.2 Tripolar Model Design

Tripolar model design considering an ideal cuff model: quasi tripole and true tripole

Considering the cuff electrode as perfect, two tripolar model approaches have been proposed: the quasi tripole and the true tripole.

The **quasi tripole** (QT) model links the two border electrodes as illustrated in Figure 3.6. In this figure, hypothetical signals of the cuff recording and behaviour with the combination of the QT are shown [12]. This model assumes that the artefacts at the central electrode and the resulting artefact of the short-circuit are the same. By subtracting them with a differential amplifier, the ENG signal is recovered [12].

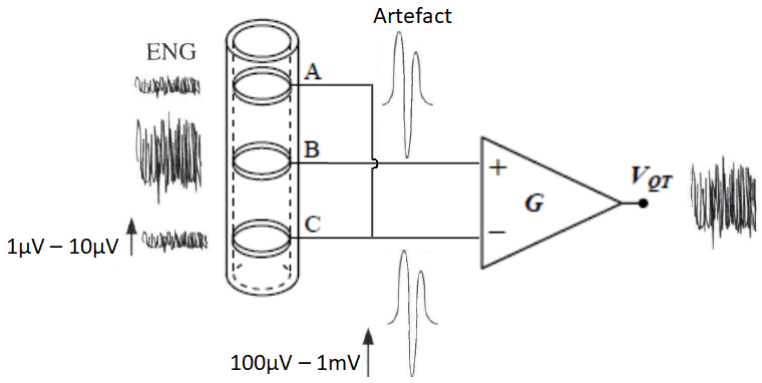

Figure 3.6: *Quasi tripole model design implementation. (Sources: [62, 13, 12]).*

The true tripole (TT) implementation (see Figure 5.9) is a bit different. By not linking the end-electrodes, the TT model is more robust, but uses 3 differential amplifiers instead of one. The difference between the middle electrode and each of the two external electrodes multiplied by a gain (G_1 and G_2 for the respective differential

signal) is first obtained and finally, the combination of those signals through G_{out} suppresses the artefact and gives the ENG signal as output [12, 13], one has:

$$V_{out} = G_{out} \cdot [G_1 \cdot (V_A - V_B) - G_2 \cdot (V_B - V_C)] \tag{3.8}$$

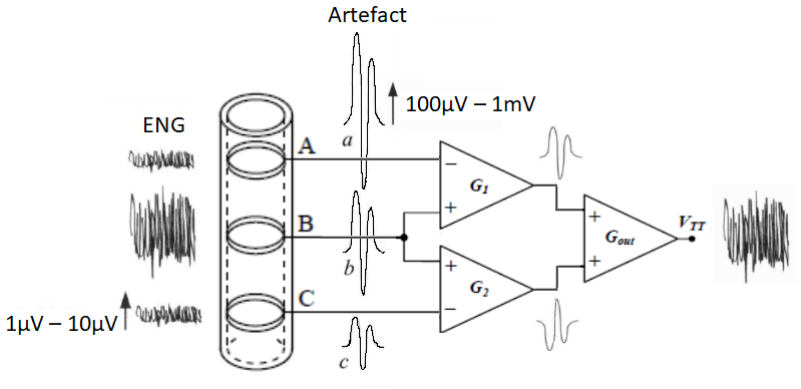

Figure 3.7: *True tripole model design implementation (Sources: [13, 12]).*

Those two models are valid for perfectly balanced tripolar cuff models, the true tripole is more accurate with respect to the artefacts. As seen in Subsection 3.1.1, to be more exact, the cuff imbalances have to be taken into account. Since the artefact signal is much larger than the ENG signal, the QT and TT will not be valid in that case.

Tripolar model design considering a non ideal cuff model: adaptive tripole.

To take the cuff imbalance into account and compensate this imbalance an adaptation of the true tripole model is proposed: the adaptive tripole (shown on Figure B.1 in Appendix B)[12, 13]. This model is based on the TT model, the gains are adapted with a feedback loop on the differential amplifier gains to take the cuff imbalance into account:

$$G_1 = G_0 \cdot (1 + X_{imb}) \tag{3.9}$$
$$G_2 = G_0 \cdot (1 - X_{imb}) \tag{3.10}$$

This model can be interesting for longtime implants. The cuff imbalance varies over time due to electrode movements and de- and regeneration of nerve fibres [11, 10]. The cuff electrode combined with the adaptive tripole model design responds to the need of a non-invasive electrode with respect to the nerve and with a high SIR. To consume less power and to miniaturise this adaptive tripole, the concept can digitally be implemented. The digital implementation is the subject of the following section.

3.2 Digital implementation of adaptive tripolar model design

The main motivations to use a microcontroller are its small size as well as its low power consumption. This section first introduces the Nucleo Board used in this thesis, then details the hardware configuration and software implementation of the adaptive tripole.

The microcontroller used in this application is the STM32L073, an ultra-low-power nucleo board (see Figure 3.8).

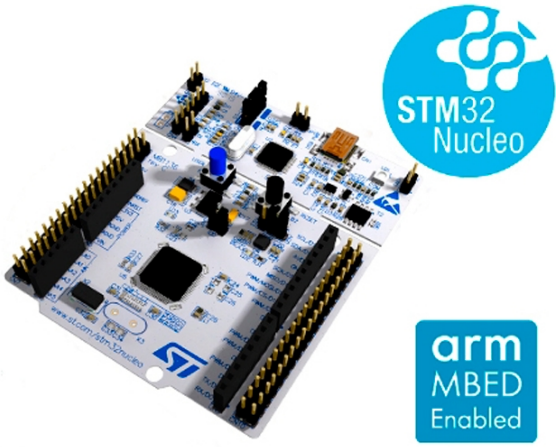

Figure 3.8: Microcontroller used for the adaptive tripole implementation: Nucleo board STM32L073 [63].

The digital implementation compensates the cuff imbalance on the micro controller. The global view of the implementation is shown in Figure 3.9. The signals are recorded with the cuff electrode, amplified and then sampled by the ADC. In the microcontroller, the values of the ADC are transferred to a buffer in memory via the DMA. Then the CPU computes the cuff imbalance and the obtained values are stored in an output buffer. This output buffer can be connected to a DAC or UART to output the data.

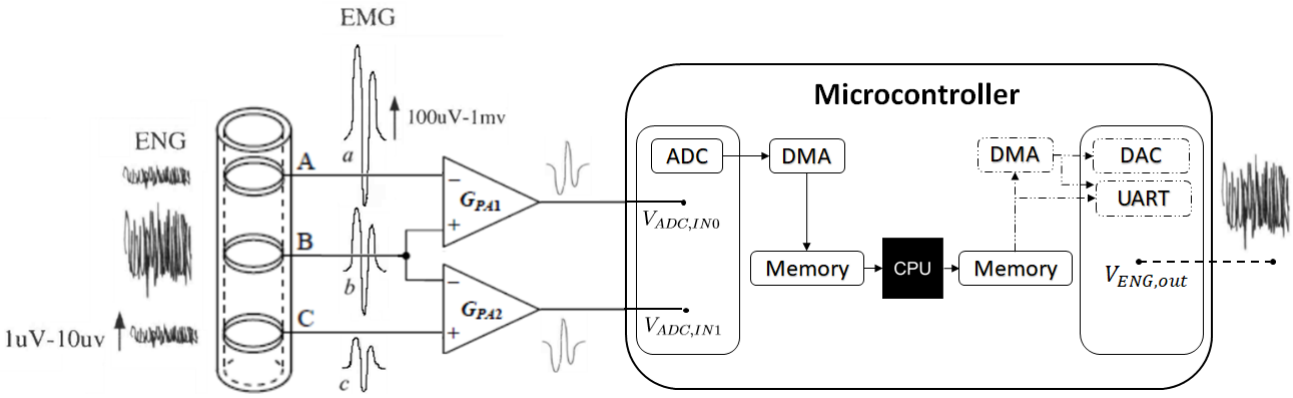

Figure 3.9: *Global view of the digital implementation combined with the cuff electrode and first level amplifiers of the TT/AT (Source: [13, 12]).*

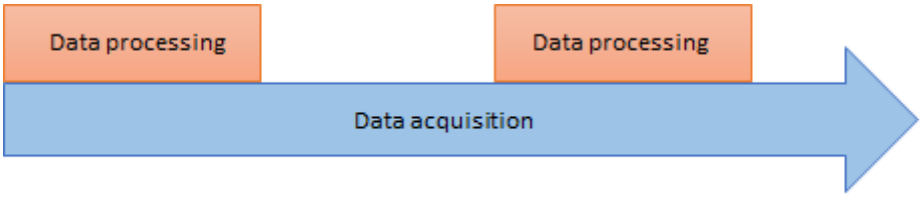

Figure 3.10: *Global view of the two main implementation parts: the blue continuous arrow represents the continuous data acquisition, while the red blocks stand for the data processing, performed periodically.*

The implementation can be divided in two main parts (illustrated on Figure 3.10):

- The continuous data acquisition with the ADC (and data output with the DAC or UART)
- The periodic imbalance compensation data processing

The requirements of the digital implementations are described in the following items:

- The acquisition of the 2 ADC inputs must be as close as possible to each other
- The data acquisition must be continuous and the frequency must be at least of 20 kHz
- The data processing time must be shorter than the data acquisition time of half a buffer
- The power consumption must be as low as possible

3.2.1 Hardware

Pin configuration

The pin configuration consists in selecting the different inputs and outputs of the system. In the chosen analog amplification configuration in front of the microcontroller, two ADCs are needed (see Chapter 4). The analog amplifiers in front of the ADC subtracts and amplifies the electrode input signals as in the following equations:

$$V_{ADC,IN0} = A_0 \cdot (V_A - V_B) + V_{offset} \quad (3.11)$$

$$V_{ADC,IN1} = A_1 \cdot (V_B - V_C) + V_{offset} \quad (3.12)$$

A_1 and A_2 stand for the total gain between the electrodes and the microcontroller and are considered as equal to each other. Those gains will be detailed in Chapter 4. V_{offset} stands for the offset voltage. The ADC acquires data between 0V and 1.8V a DC offset is consequently needed to be able to acquire the signal. Concerning the resulting data, it can be accessed with a DAC or with a UART. Figure 3.11

represents the default mode of the pin configuration with the two inputs selected and without considering the output of the system.

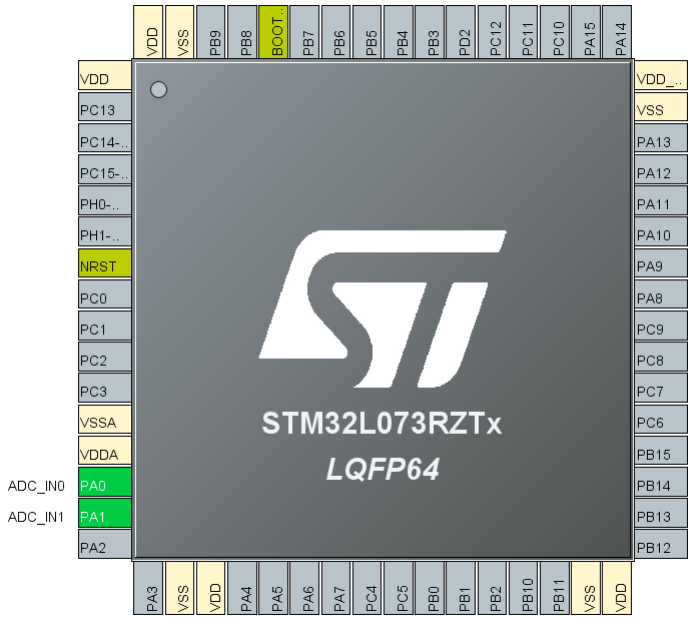

Figure 3.11: *Default pin configuration on STM32cubeMX (only the 2 ADC inputs are considered).*

Clock configuration

Concerning the clock configuration, three different clocks are used. The system clock is configured in Multispeed internal (MSI) resistor, capacitor (RC) oscillator mode. The ADC clock mode consist of a dual clock-domain architecture. The ADC is fed by an ADC synchronous clock who determines the time of the data acquisition at the ADC input while an external clock, Timer 6 defines the data acquisition rate. As illustrated in Figure 3.12, the Timer 6 depends on the system clock while the ADC clock does not. Timer 6 has a frequency of 20kHz, every $50\mu s$, one data of each ADC input (ADC_0 and ADC_1) is consecutively acquired, this acquisition sequence corresponds to the standard conversion mode. The conversion time (t_{CONV}) is determined by the ADC clock frequency (16MHz) and the number of cycles. The time of one ADC clock cycle (t_{ADC_CLK}) is thus 62.5 ns ($= 1/16MHz$). The number of cycles needed for the data acquisition is 14:

- 1.5 cycles for the data sampling (the corresponding sampling time is t_{SMPL})
- 12.5 cycles for the successive approximation (the corresponding successive approximation time is t_{SAR}).

The conversion time of the acquisition of one data is given by the following equations:

$$t_{CONV} = t_{SMPL} + t_{SAR} \tag{3.13}$$
$$= [1.5 + 12.5] \cdot t_{ADC\_CLK} \tag{3.14}$$
$$= 0.875\mu s \tag{3.15}$$

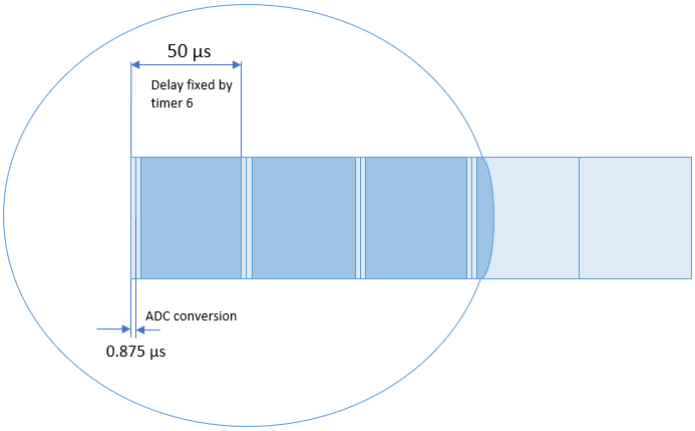

Figure 3.12: *Illustration of the data acquisition timing: the light blue strips represent the ADC conversion time of the 2 input signals at the ADC_0 and ADC_1 inputs. The darker blue parts represents the waiting time between 2 acquisition sequences.*

For the data processing, the Cortex System Timer determines the data processing speed. It depends of the system clock that has a frequency of 4194 kHz.

	Frequency	Used for	Managed by system clock
ADC clock	16 MHz	Data acquisition	No
Timer 6	20kHz	Data acquisition (and Data output)	Yes
Cortex System Timer	4194kHz	Data processing	Yes

Table 3.1: *Summary of the different clocks used in the implementation.*

The connections configuration between the peripherals

The different peripherals used are the **ADC, the Timer 6, the memory and the DAC or UART**. Figure 3.13 illustrates the different relationships between the different used blocks and also illustrates the considered input and output buffers for the data processing that will be discussed in Subsection 3.2.2. The main part of the peripheral configuration is linked to the data acquisition and data output. Concerning the ADC, the following points summarize the configuration:

- The **external trigger conversion source** to acquire data at a rate of 20kHz is the Timer 6, as discussed in Subsection 3.2.1. The trigger detection is configured on the rising edge.
- The **standard conversion mode** is used (as illustrated in Figure 3.12)
- The acquired data is coded on 12 bits.
- Concerning the low power features, the auto-off mode and the low frequency mode are enabled. The **low-power frequency mode** works at reduced clock

frequency while keeping the optimum ADC performance (0.87 μs). The **auto-off mode** powers automatically the ADC off except during the active conversion phase.

- The **DMA continuous request** has been enabled: the ADC generates a DMA transfer request each time a new conversion data word is available.

Table 3.2 gives an overview of the different interrupts and update events with their corresponding functions.

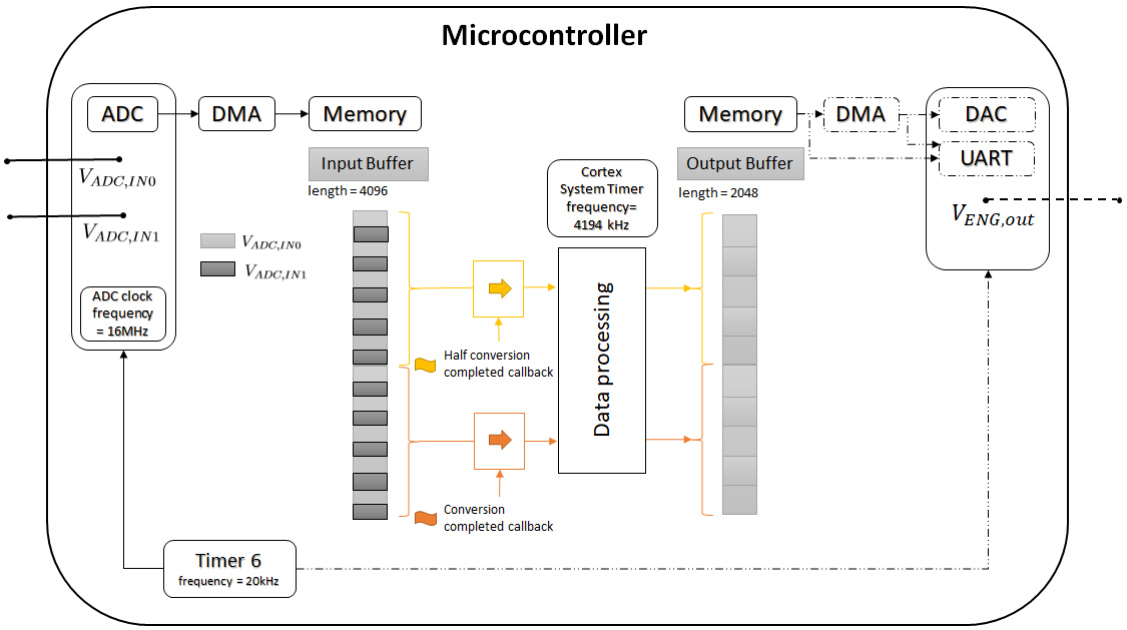

Figure 3.13: *A complete view of the different interactions between the Timer 6, the ADC, the DMA, the memory and the DAC and UART. In the middle the input and output buffers are emphasised. The DMA directly transfers the data of the ADC to the input buffer by alternating between ADC_0 (light grey) and ADC_1 (dark grey) input data. The two callbacks are indicated with flags. At the end of the data processing, the output data is stored in an output buffer. To access these values, a DAC or UART can be used. They can be combined to a DMA and Timer 6 to synchronise the input and output rate.*

	Interrupt/ Update event	Function
Timer 6	Trigger on rising edge	Launches one ADC sequence acquiring Output of one DAC or UART value
ADC	DMA continuous request	DMA request each time the conversion of an ADC data is completed
DMA	Callback	Starts a callback function when the input buffer is half or completely full

Table 3.2: *Overview of the different generated interrupts or events and their corresponding function*

The acquisition of a data sequence with the ADC (ADC_0 and ADC_1) starts at each **rising edge of the Timer 6** and is converted to a digital 12-bit word. Once this data is **converted to a digital 12-bit word**, the data has to be transferred to the memory. To **transfer data from the ADC to the memory**, the **DMA** is used. DMA provides a high-speed data transfer from a peripheral to the memory (from the ADC to a the input buffer) or from the memory to a peripheral (from the output buffer to the DAC or UART) without using the CPU [14]. The ADC sends a DMA request each time a converted data is available (thanks to the enabled continuous DMA request) in order to transfer this data to the input buffer in memory. Concerning the DMA, the following request settings have been chosen:

- The circular mode has been selected
- The memory has been chosen to fix the increment address
- The chosen data width is half a word (16 bits) (to recall, the data was acquired on 12 bits)

An interesting aspect of the DMA is the fact that interrupts are produced when the transfer buffer is half or completely filled [14]. For STM32 devices those interrupts are called **callbacks**. Those callbacks are used in the software implementation to initiate the data processing as illustrated in Figure 3.13.

In memory, the **data processing is launched by DMA interrupts and the corresponding the callback functions**, called by those DMA interrupts. The output data is stored in an output buffer during the data processing (cf. Subsection3.2.2). To access this output buffer data with the DMA at the same frequency as the ADC, the **DAC or UART** are triggered by the Timer 6 (as the ADC) and the DMA setting is configured in circular mode. At each **rising edge of the Timer 6**, the **DMA transmits one value of the output buffer** to either the DAC or the UART in function of which peripheral is activated. The UART can also reach the

data without passing through DMA if the data output timing do not matter or if some specific values in memory must be reached.

3.2.2 Software: the adaptive tripole implementation

The data processing block of Figure 3.13 represents the cuff imbalance compensation and computation. The data processing is launched every time the DMA sends an interrupt (callback). This interrupt calls the corresponding callback function (illustrated on Figure 3.14). The callback function is divided in three main blocks: the callback initialization, the for loop and the gain computation.

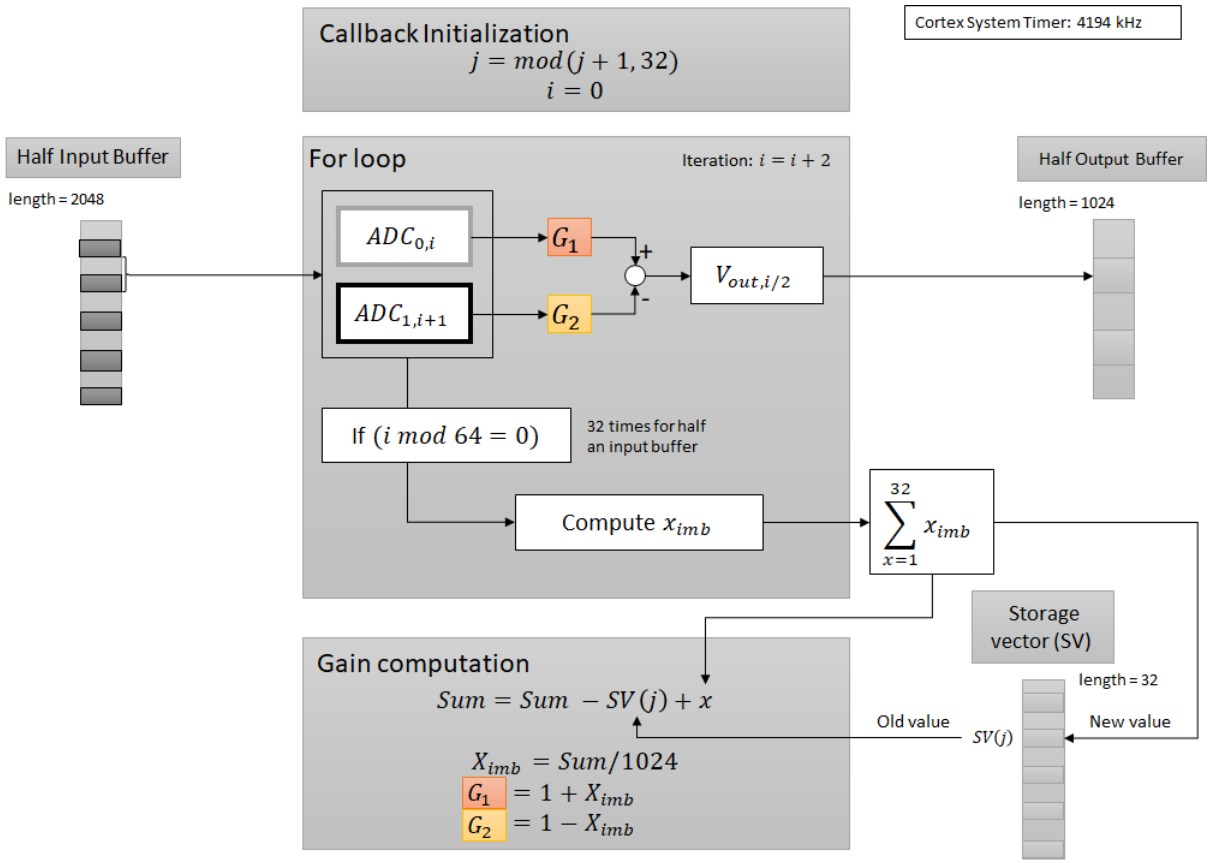

Figure 3.14: *Illustration of the data processing inside a callback function. The details about the different variables are given in Table 3.3.*

Used variables

The variables used for the cuff imbalance compensation implementation are summarised in Table 3.3. With the different sizes, the minimum, typical and maximum values, the variable type and the function in the data processing. The **integer type** has been chosen instead of float for the imbalance computation in order to save memory and computation time. In order to have a precision of **three decimals**, x_{imb} is multiplied by 1000. The output result is consequently divided by 1000 when stored in the output buffer. In the real implementation, the uintxx_t type do not manage negative values, to resolve that problem, a gain g_1 is used to store the imbalance

computation with an offset of 1000: ($g_1 = 1000 + x_{imb}$). The notation used in this section has been chosen to keep a clear link with the imbalance computation and the equations of Section 3.1. (The exact code is given in Appendix C.)

	Name	Size	Min value	Typical value	Max value	Type	Function
Vector	Input Buffer	4096	0	2048	4096	uint16_t	Contains the input values for the data processing
	Output Buffer	2048	0	2048	4096	uint16_t	Contains the output values of the data processing
	Storage Vector	32	-32000	0	32000	uint16_t	Stores the sum of the 32 computed x_{imb} of one for loop
Variables	G_1	1	0	1000	2000	uint16_t	Gain of the ADC_0
	G_2	1	0	1000	2000	uint16_t	Gain of the ADC_1
	x_{imb}	1	-1000	0	1000	uint16_t	Imbalance computed with two input values
	X_{imb}	1	-1000	0	1000	uint16_t	Mean of imbalance over 1024 measures
	Sum	1	-1024000	0	1024000	uint32_t	Sum of 1024 imbalance computations
Index	i	1	0	-	4094	uint16_t	Index iterating on both the input and output buffer
	j	1	0	-	31	uint8_t	Index iterating on the storage vector

Table 3.3: *Summary of the different variables used for the imbalance computation schematics.*

Callback initialisation

In the callback initialization, index j is incremented and index i is reset to 0. Index j, as indicated in Table 3.3, is the index that iterates over the storage vector. Using this vector increases the considered amount of data used to compute the mean of the imbalance value. The maximum value of j has arbitrary been fixed at 32. Index i is the index used to iterate over the input and output buffer. In the code, $g_1$is initialised to 32000 ($= 32 \cdot 1000$: the imbalance is computed 32 times in the for loop and three decimals are considered).

For loop

The for loop iterates over all the values stored in the input buffer. At each iteration the cuff imbalance compensation is computed with two incoming values. Based on equation (3.8), the computation is done by:

$$V_{out,i/2} = G_1 \cdot V_{ADC_0,i} - G_2 \cdot V_{ADC_1,i+1} \tag{3.16}$$

In the code, the offset had to be taken into account. The offset is thus first subtracted from the incoming data before being multiplied by the gains. Since the gains were multiplied by 1000, the result has to be divided by 1000. Finally the offset is added in order to get an output value between and 4096, who can be output either by the DAC or the UART.

$$V_{out,i/2} = \frac{VDD}{2} + \left[G_1 \cdot \left(V_{ADC_0,i} - \frac{VDD}{2}\right) - G_2 \cdot \left(V_{ADC_1,i+1} - \frac{VDD}{2}\right)\right]/1000 \tag{3.17}$$

Every time i is a multiple of 64, an estimation of the cuff imbalance value x_{imb} is computed with one ADC_0 and one ADC_1 sample and added to a variable in memory. Equation (3.7) is used to compute x_{imb} w.r.t. the electrode voltages, to recall:

$$x_{imb} = \frac{|V_A - V_B| - |V_B - V_C|}{|V_A - V_B| + |V_B - V_C|} \tag{3.18}$$

To be mathematically correct w.r.t. the equations (3.11), (3.12) and (3.18), the offset has to be subtracted from the ADC-values. The gains A_0 and A_1 are considered to be equal. The microcontroller takes the difference of the amplifier gain between the two ADC input into account in the imbalance computation. The result is then multiplied by 1000: since x_{imb} is an integer, doing this operation enables to keep three decimals.

$$x_{imb} = \frac{|V_{ADC_0} - \frac{VDD}{2}| - |V_{ADC_1} - \frac{VDD}{2}|}{|V_{ADC_0} - \frac{VDD}{2}| + |V_{ADC_1} - \frac{VDD}{2}|} \cdot 1000 \tag{3.19}$$

As already mentionned, the imbalance is directly summed up with a factor 1000 in the code implementation, this way dealing with negative values is avoided and an estimation of G_1, g_1, is directly computed. At the end of the for loop, this variable contains the sum of 32 computations of x_{imb}. This value was fixed by determining the maximum number of g_1 a uint16_t data type variable (65536) could contain, one has:

$$65536/2000 = 32.7 \tag{3.20}$$

Since i iterates over 2048 values, taking two input samples (one ADC_0 and one ADC_1) every time i is a multiple of 64, gives a sum of 32 values.

Gain Computation

In order to have a quite accurate imbalance value, the mean is taken over 1024 x_{imb} computation. This is done by keeping the sum of the computed x_{imb} values into a storage vector and keeping the sum of the elements of this vector in a Sum variable. At each gain computation the old value stored at index j of the storage vector is subtracted from the Sum and the new computed value is added. Then, this new value is stored at the index j of the storage vector. The imbalance value is then computed:

$$X_{imb} = Sum/1024 \tag{3.21}$$

Finally, the gain computation of the adaptive tripole is done, based on equations (3.9) and (3.9):

$$G_1 = 1 + X_{imb} \tag{3.22}$$
$$G_2 = 1 - X_{imb} \tag{3.23}$$

As already mentioned, in the code, G_1 is directly computed to reduce the computation time and to avoid negative values who cannot be stored in a uint16_t type.

The delay to change of imbalance value is:

$$T = 32 \cdot (1024 \cdot 50\mu s) = 1.64s \tag{3.24}$$

This can be modified by changing the maximum value of index j (fixed at 32), this value can vary between 1 and 256, corresponding to 51.2 ms and 13.1 s respectively.

3.3 Summary

The goal of this chapter was to propose a digital implementation of the adaptive tripolar model design. The first section introduced the different tripolar models (QT, TT and AT) and the notion of cuff imbalance (X_{imb}). Thanks to the linearization effect of the cuff electrode, the cuff imbalance can be compensated. To do so, the imbalance is first computed, the gains are then adapted with the imbalance value and finally the input signal is compensated. The main goal of this compensation was to remove the artefacts despite the cuff imbalance and to recover the neural signal.

In order to record the biological signals with the microcontroller, the cuff electrode signals have to be amplified. Chapter 4 details the different stages of the analog amplifier in front of the microcontroller.

Chapter 4

Analog amplifier implementation

The circuit implementation consist of three building blocks: the cuff electrode, the analog amplifier and the microcontroller (as previously designed in Section 3.2). This section gets more into the details of the analog amplifier. The analog amlifier is divided in three subparts: a custom integrated differential instrumentation amplifier previously designed in the ECS group at UCLouvain (integrated IA), an instrumentation amplifier built using discrete components (discrete IA) and a Sallen-Key low pass filter (see Figure 4.1). The integrated IA has a low power consumption and a very low noise addition with a fixed gain. The discrete IA amplifies further the signal to match the ADC input requirements, reduces the low-frequency artefacts with a second order high-pass filter and implements a differential to single-ended conversion. The Sallen-Key low pass filter has a cut-off frequency at 13.3 kHz. This analog amplification and filter is then followed by the microcontroller which implements the cuff imballance digital compensation.

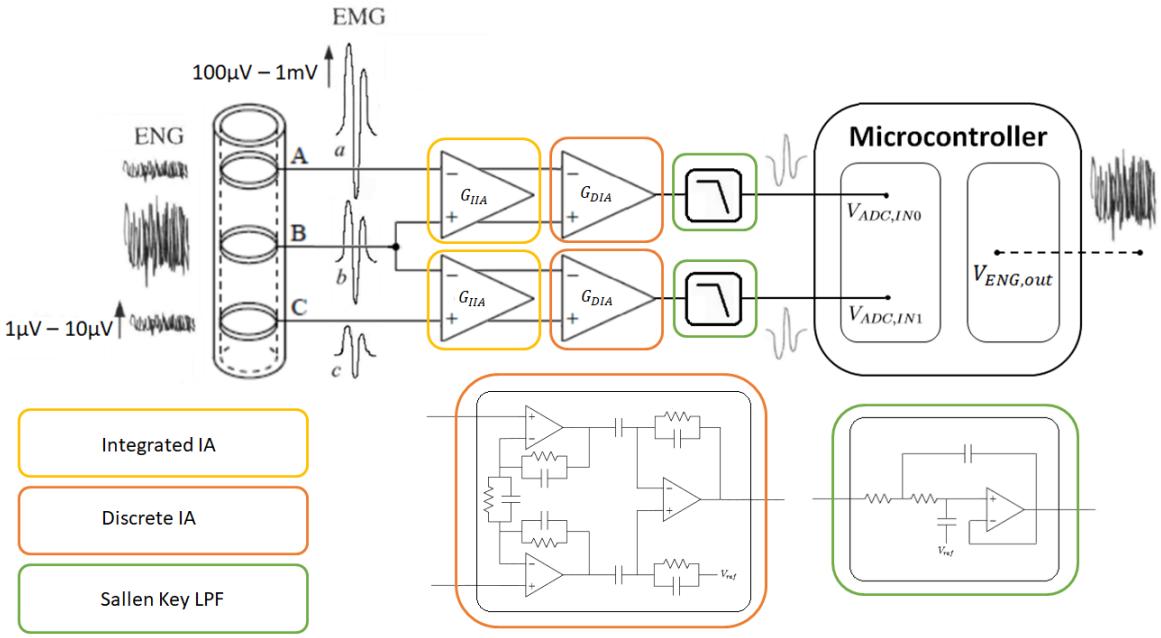

Figure 4.1: *Schema of the analog amplification level with a detail of the second stage instrumentation amplifier and the sallen key configuration.*

4.1 Input signal characterisation and circuit specifications

The signals measured by the cuff electrodes are composed of the artefact signal (that linearly increases or decreases along the cuff) and the neural signal (considered at the middle electrode of the cuff) as discussed in Section 3.1. The considered specifications of the artefacts and neural signal (Table 4.1) are based on a comparison of different works about peripheral nerve recording with tripolar electrodes (cf. Appendix D).

	min	typical	max	unit
Artefact amplitude at an electrode	0.870	1	1.130	mV
Artefact amplitude difference between 2 electrodes	0	100	130	μV
ENG signal amplitude	1		10	μV
Artefact frequency	1	100 - 250	3000	Hz
ENG signal frequency	500	300 - 3000	10000	Hz

Table 4.1: *Bioelectric signal specification.*

The microcontroller is powered with 1.8V and the ADC of the microcontroller takes signals between 0 and 1.8V. The signal has to be amplified in order to be quantized (as previously mentionned in section 3.3). Table 4.2 summarises the main specification at the input of the microcontroller.

	min	typical	max	unit
Input Voltage Range	0.280	0.900	1.520	V
Frequency range	150	800 - 3000	12000	Hz

Table 4.2: *Microcontroller ADC input requirements.*

The maximum amplitude at the input of the microcontroller is fixed at $0.620V$ (cf. Table 4.2) and the maximum considered amplitude between two electrodes is $130\mu V$ (cf. Table 4.1). The total gain of the analog amplification level can be deduced:

$$G_{tot,DM} = \frac{0.620V}{130\mu V} = 4.77 \cdot 10^3 V/V \tag{4.1}$$

This gain can further be divided in two parts: the gain linked to the integrated IA and the discrete IA. Table 4.3 Summarises the different target gain stages as wel as the cut-off frequencies.

		Value	Unit
Gain	Integrated IA	63.8	V/V
	Discrete IA	75	V/V
Frequency	Low cut-off frequency	100 - 200	Hz
	High cut-off frequency	12 - 13	kHz

Table 4.3: *Gain an frequency target specifications.*

4.2 The custom integrated IA

The custom integrated IA is a **fully differential IA** from which the specifications are contained in Table 4.4. The 4 columns correspond to the 4 possible configurations. The main goal is to have a **maximum gain** with this integrated IA in order to **limit the noise addition**. Compared to the consumption of the other instrumentation amplifier because of its low noise addition while keeping a **low power consumption**. Compared to the power consumption of the other parts of the circuit as the microcontroller (2.6 mW), the power consumption of the 4 configurations are much lower. The fourth configuration is consequently chosen for it's high gain and low noise addition.

	C1	C2	C3	**C4**
Power [μW]	0.631	1.31	5.41	**23.9**
Noise [μV,rms]	1.36	0.67	0.36	**0.23**
Gain [V/V]	48.9	32.6	44.3	**63.8**
CMRR [dB]	93.7	105.6	106.2	106.9
Dyn. range [V]	0.96	0.89	0.82	0.79
Harm. Distorsion [%]	1.2	0.7	0.8	1
Input impedance [MΩ]	43.3	27.1	19.1	13.1
Max. bandwidth [kHz]	29.3	82.1	185.6	279.5

Table 4.4: *4 different configurations of the integrated IA.*

The output signals obtained with a fully differential IA are:

$$V_{out,+} = \frac{1}{2}G_{IIA}(V_{in,+} - V_{in,-}) + V_{offset} \tag{4.2}$$

$$V_{out,-} = -\frac{1}{2}G_{IIA}(V_{in,+} - V_{in,-}) + V_{offset} \tag{4.3}$$

As discussed in table 4.4, the gain of the chosen configuration of the integrated IA is $63.8V/V$. The maximum considered artefact amplitude difference between 2 electrodes is $130\mu V$ (cf. Table 4.1). By filling those values in the equations 4.2 and 4.3, the maximum differential output voltages of the integrated IA are:

$$\frac{-8.3mV}{2} \leq V_{out,+/-} - 0.6 \leq \frac{8.3mV}{2} \tag{4.4}$$

$$-8.3mV \leq V_{out,+} - V_{out,-} \leq 8.3mV \tag{4.5}$$

4.3 Discrete IA combined with sallen key lowpass filter

From the target specification mentioned in Table 4.3, the discrete IA implements as wel a gain of 75 V/V as a high-pass filter. The Sallen-Key implements a second order low pass filter to further remove the high frequency noise.

4.3.1 Circuit

The circuit of the discrete IA combined with a low-pass Sallen-Key filter is illustrated on Figure 4.2. The discrete IA is composed of two amplification levels: the input buffer level and the differential amplifier level. The main goal of this circuit is to amplify the signal with a gain of $75V/V$ and to bandpass the signal.

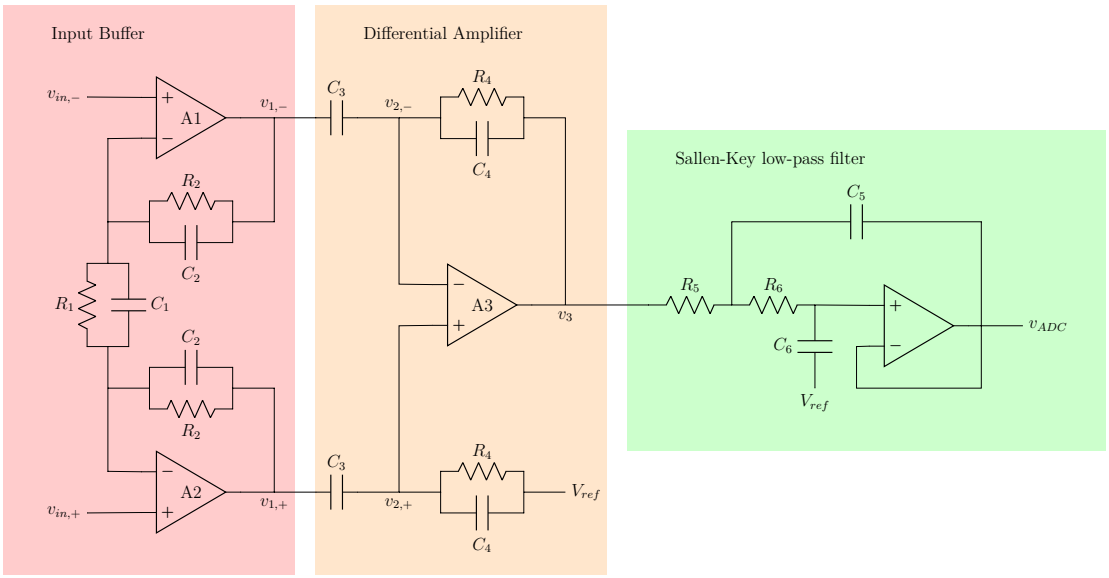

Figure 4.2: *High input impedance Instrumentation amplifier composed of 2 input buffers and a differential amplifier [64] combined with a sallen key filter.*

The specifications fixed and the obtained results are summarised in Table 4.5. The target and chosed values of the different discrete components w.r.t. the circuit on Figure 4.2 are summarised in Table 4.6.

	Target value or target range	Obtained value	Unit
Input buffer gain	15	15.04	V/V
Differential amplifier gain	5	5	V/V
Low cut-off frequency	100 - 200	159	Hz
High cut-off frequency	10 - 13	13.3	kHz

Table 4.5: *Discrete IA specifications. The obtained gain values are quite close to the target value. The low cut-off frequency is in the middle of the target range. The high cut-off frequency does not correspond to the fixed target range.*

	Target value	Chosen value	Unit
R_1	11.29	10	$M\Omega$
R_2	2.82	2.7	$M\Omega$
R_4	1	1	$M\Omega$
R_5	1.4	1.2	$M\Omega$
R_6	1.4	1.2	$M\Omega$
C_1	3.29	3.3	nF
C_2	0.47	0.47	nF
C_3	5	5	nF
C_4	1	1	nF
C_5	10	10	nF
C_6	10	10	nF

Table 4.6: *Discrete IA component value*

Figure 4.3 represents the bode diagram of the circuit of Figure 4.2 with the component values of Table 4.6. The main goal was to chose component values such that the peak power frequency range (between 800 Hz and 3kHz (cf. Table 4.1) had a constant gain of 75V/V. The cut-off frequencies have been chosen in consequence. The neural signal is contained between 500Hz and 10kHz. Since artefacts are present in the low-frequency range and keeping high-frequencies increase the amount of noise, the total ENG signal bandwidth cannot be multiplied by the total gain. This is why the peak power frequency range determines the frequency range in which the gain is constant. Ideally, the bandwidth should further be reduced to limit the noise, but to take this decision, it would be useful to have the exact frequency range of neural signals recorded on the vagus nerve in normal situation and in the case of a seizure.

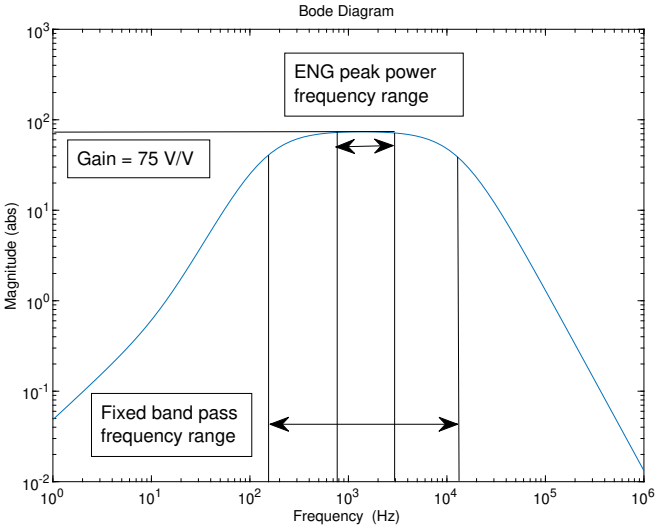

Figure 4.3: *Bode diagram of the total transfer function of the circuit on Figure 4.2.*

Appendix H gives a detailed overview of the equations of the discrete IA and the Sallen-Key low-pass filter. The specifications of the different parts of the circuit with the corresponding bode diagram and the choice of the components are further detailed as wel as the component ratios that fix the gains and cut-off frequencies.

4.3.2 Operational amplifier choice

The different low power consumption DIP-type operational amplifiers found on the Farnell website are compared in table 4.7. By comparing them to the requirements in the last column of table 4.7 (see Appendix G for the computation details), the two most suitable operational amplifiers are the MCP600x [65] and the MCP624x [66]. The MCP624x is finally chosen to perform the different for the amplifier circuit for his lower power consumption.

	MCP600x [63]	MCP604x [67]	MCP624x [66]	LM613x [68]	LM614x [69]	LM10Cx [70]	OP90GPZ [71]/ OP290GPZ [72]	requirements
Supply voltage range [V]	1.8 - 6	1.4 - 6	1.8 - 5.5	1.8 - 24	1.8 - 24	1.1 - 7	1.6 - 36	must comprise: 1.8
Slew rate [V/μs]	0.6	0.003	0.3	12	13	-	0.012	min: 0.0935
Input impedance [Ω]	10^{13}	10^{13}	10^{13}	104M	126M	400k	30M	max
Noise density [$nV/\sqrt{Hz}$]	28	170	45	27	16	42	$3\mu V/V$	max: 52.75
Gain Bandwidth	1MHz	2.8MHz	550kHz	10MHz	10MHz	50kHz	20kHz	min:180kHz
Quiescent power consumption [μW/amplifier]	180	1.08	90	648	1170	486	36	min

Table 4.7: *Comparison of the different DIP operational amplifiers of Farnell.*

4.4 Noise Analysis

The total amount of noise on each input is the result of the combination of the noise accumulated through the different amplifier stages. This section analyses the theoretical noise of the different parts of the global circuit: the integrated IA, the differential IA, the Sallen Key and the microcontroller accuracy. All the noise sources are finally referred at the input to get an idea of the total amount of noise. The different used equations and values are mentioned in this section, for more mathematical details, the equations of the different noise gain factors are detailed in Appendix E. To compute the sum of the different noise sources at the input or output of a circuit, the root sum squared value is taken:

$$v_{n,tot} = \sqrt{\sum_i (v_{n,i}^2)} \tag{4.6}$$

4.4.1 Integrated IA

Concerning the integrated IA, only the voltage noise is taken into account. The voltage noise density of the integrated IA is represented on Figure 4.4.

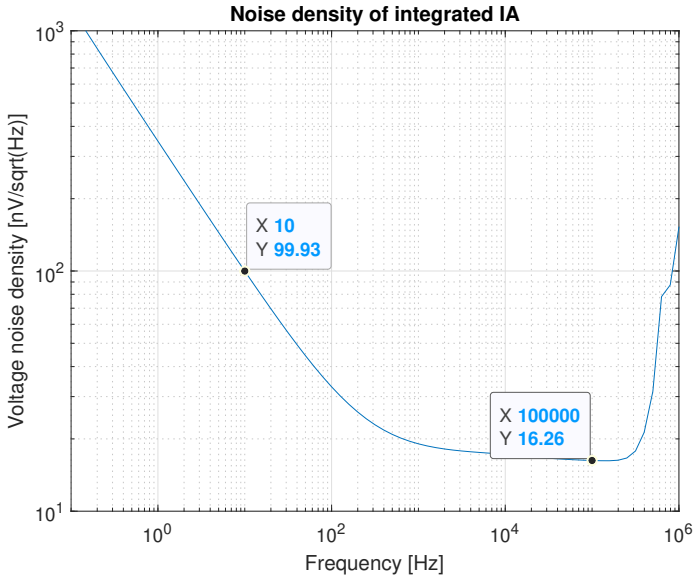

Figure 4.4: *Noise density of Integrated Instrumentation amplifier.*

The total amount of voltage noise of the integrated IA is the combination of the flicker noise ($v_{n,flicker}$) and the thermal noise ($v_{n,thermal}$):

$$v_{n,tot} = \sqrt{v_{n,flicker}^2 + v_{n,thermal}^2} \tag{4.7}$$

The flicker and thermal noise are computed with the following equations;

$$E_{n,flicker} = e_{f_0} \cdot \sqrt{f_0} \cdot \sqrt{\log \frac{f_H}{f_L}} \tag{4.8}$$

$$E_{n,th} = e_{f,th} \sqrt{BW} \tag{4.9}$$

The results obtained with the measures of the integrated IA (Figure 4.4) are summarised in Table 4.8.

	Value $[\mu V_{rms}]$
$v_{n,flicker}$	1.40
$v_{n,thermal}$	2.05
$v_{n,tot}$	2.48

Table 4.8: *Input referred voltage noise of the integrated instrumentation amplifier.*

4.4.2 Discrete IA

For the discrete IA, first the voltage noise of the MCP624 is computed. Then the voltage noise and current noise of the different operational amplifiers referred at the input and output is computed. Afterwards, the noise linked to the components is computed and finally the total input referred noise of the discrete IA is computed.

Voltage noise density of the MCP624x

Since the corner frequency (300Hz) is not much lower than the cut-off frequency (10kHz), both the flicker and thermal noise contributions are considered for the voltage noise computation. Table 4.9 summarises the contribution of both the flicker noise and thermal noise to the total voltage noise.

	Value $[\mu V_{rms}]$
$v_{n,flicker}$	1.47
$v_{n,thermal}$	5.67
$v_{n,tot}$	5.86

Table 4.9: *Input referred voltage noise of the integrated instrumenttation amplifier.*

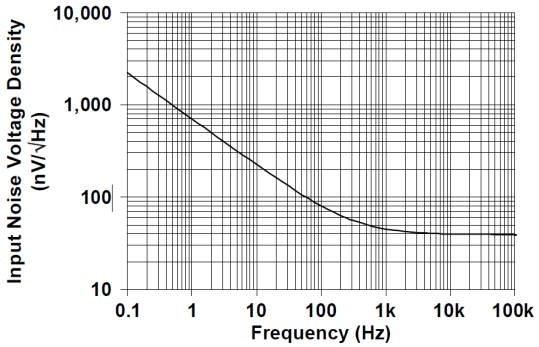

Figure 4.5: *Input noise density of the MCP624x operational amplifier [66].*

Voltage noise density

The contribution of the voltage noise density of each operational amplifier to the total voltage noise density of the discrete IA is given in Table 4.10. The voltage

noise of the two input buffer operational amplifiers contribute the most to the total input referred noise.

	v_n $[\mu V_{rms}]$	Noise gain factor V/V	Output referred noise $[\mu V_{rms}]$	Input referred noise $[\mu V_{rms}]$
A1	5.86	75	439.5	5.86
A2	5.86	75	439.5	5.86
A3	5.86	8.07	47.3	0.63
$v_{n,tot}$			623.3	8.31

Table 4.10: *Voltage noise of the discrete IA referred at the output and output of the discrete IA.*

Current noise density

The current noise density of the MCP624 is $i_{in} = 4fA/\sqrt{Hz}$ according to the datasheet [66]. This current noise density is the same for the positive and negative input of the operational amplifiers. The contribution of the current noise density of each operational amplifier to the total voltage noise density of the discrete IA is given in Table 4.11.

		i_n $[pA_{rms}]$	Noise gain factor $[k\Omega]$	Output referred noise $[\mu V_{rms}]$	Input referred noise $[\mu V_{rms}]$
A1	v_{in+}	52	139	0.088	0.0012
	v_{in-}	52	24307.34	11.09	0.148
A2	v_{in+}	52	139	0.088	0.0012
	v_{in-}	52	24307.34	11.09	0.148
A3	v_{in+}	52	1414.2	0.645	0.0086
	v_{in-}	52	1414.2	0.645	0.0086
$v_{n,tot}$				15.705	0.2094

Table 4.11: *Current noise of the discrete IA referred at the input and output of the discrete IA.*

Resistance noise

The noise contribution of the different resistances of the circuit are given by the following formulla:

$$v_n^2 = 4k_B T R \Delta f \tag{4.10}$$

The noise contribution of the different capacitors of the circuit are given by the following formulla [73]:

$$v_n^2 = \frac{k_B T}{C} \tag{4.11}$$

Table 4.13 summarises the impedance value, the corresponding noise voltage, the noise gain factor and the output referred noise. The main contribution is linked to the impedance Z_1, and more specifically to the resistance R_1 (10 MΩ).

	v_n $[\mu V_{rms}]$	Noise gain factor V/V	Output referred noise $[\mu V_{rms}]$	Input referred noise $[\mu V_{rms}]$
Z_1	4.35	68.8	299.0	3.99
Z_2	2.27	4.94	11.2	0.15
Z_3	0.91	4.94	4.5	0.06
Z_4	1.39	1	1.4	0.02
$v_{n,tot}$			299.2	3.99

Table 4.12: *Noise voltage, the noise gain factor and the output reffered noise.*

Total input referred noise

Taking the three noise sources into account, the total input referred noise of the discrete IA is computed. The result is provided in Table 4.13.

	Input referred noise $[\mu V_{rms}]$
Voltage noise	8.31
Current Noise	0.21
Component noise	3.99
$V_{RMS,\text{Differential IA}}$	9.22

Table 4.13: *Noise voltage, the noise gain factor and the output reffered noise.*

The voltage noise represents the most important noise source, followed by the noise due to resistance R_1.

4.4.3 Sallen-Key

Concerning the Sallen-Key, the voltage noise, current noise and the noise due to the electrical components are summarised in Table 4.14. Since the computation of the different types of noise is similar to the way the noise of the discrete IA has been computed, the different noise sources are summarised in one table. The main source of noise of the Sallen-Key is the voltage noise of the operational amplifier.

			Noise gain factor V/V	Output referred noise $[\mu V_{rms}]$	Input referred noise $[\mu V_{rms}]$
Voltage noise		$5.86\mu V_{RMS}$	1.01	5.86	5.86
Current noise	$i_{in,+}$	52 pA_{RMS}	398.7	0.021	0.021
	$i_{in,-}$	52 pA_{RMS}	15	0.00073	0.00073
Component noise	R1	$4.76\mu V_{RMS}$	0.99	0.00476	0.00476
	R2	$4.76nV_{RMS}$	0.99	0.00476	0.00476
	C1	$64.3nV_{RMS}$	0.08	0.0051	0.0643
	C2	$64.3nV_{RMS}$	0.99	0.0643	0.0643
$V_{RMS,\text{Sallen-Key}}$				5.86	5.86

Table 4.14: Noise of the Sallen-Key low-pass filter

4.4.4 Microcontroller

The noise added at the input of the microcontroller is found by taking the histogram of measured values. The V_{RMS} corresponds to the standard deviation of the measured values. The standard deviation of the measures is equal to 3 LSB. This corresponds to $V_{RMS,\text{Microcontroller}} = 1.3mV$ at the input of the microcontroller.

4.4.5 Global input referred noise

The total input referred noise of the different circuit parts are summarised in Table 4.15. In this table, the noises are all referred at the input of the integrated IA.

	Input referred noise $[\mu V_{rms}]$
$V_{RMS,\text{Integrated IA}}$	2.48
$V_{RMS,\text{Differential IA}}$	0.12
$V_{RMS,\text{Sallen-Key}}$	0.0012
$V_{RMS,\text{Microcontroller}}$	0.27
$V_{RMS,\text{Total}}$	2.50

Table 4.15: *Noise of the different blocks reffered at the input of the circuit*

As conclusion, the total input referred noise is mainly determined by the first amplification level: the integrated IA. The best way to lower the total amount of noise is by further reducing the band pass frequency range.

4.5 Summary

This chapter gives more details about the signal amplification in front of the microcontroller. First the signal specifications were introduced, then the integrated IA, the Discrete IA and the Sallen-Key low-pass filter were detailed and finally a view of the different noise sources is detailed and the total input referred noise is computed. This input referred noise is mainly determined by the integrated IA.

Chapter 5

Measures, simulations and discussion of the results

5.1 Available material

The available material to perform the different tests were:

- Triple output DC power supply: Agilent - E3631A
- 15MHz Function/waveform generator: Hewlett packard - 33120A
- Source meter: Keithley - 2450
- Digital Oscilloscope: Tektronix - TBS2000 series

5.2 Simulations and measures of the Analog amplifier

5.2.1 Measure of bode diagram

To test the performance of the discrete IA, the circuit has been adapted. The circuit adaptations as wel as the measurement scheme and the measures at the different points of the circuit compared to the simulation and the expected equations are developed in appendix F. The obtained output measures are compared with the adapted bode diagram on Figure 5.1. Measures have been performed between the discrete IA and the Sallen-Key low-pass filter (v_3 on Figure 4.2 and the blue line and dots on Figure 5.1) and at the output of the Sallen-Key low-pass filter (v_{ADC} on Figure 4.2 and the red line and dots on Figure 5.1).

The measures at the input of the Sallen-Key do not follow the theoretical curve. First an under-damping phenomenon linked to the closed loop gain appears between 5 and $30kHz$. The values of the capacitors and resistances have been chosen in order to limit this overshoot and avoid its influence in the peak power frequency range while keeping acceptable component values. Then the blue dots gain decreases with 40dB / decade. The gain bandwidth of the MCP624 is 550 kHz as mentioned in chapter 4. Since the gain of the input buffers is around 7 (equation F.4), the

maximum bandwith is $550kHz/7 = 78kHz$. This corresponds to the frequency at which the gain of the measures at the input of the Sallen-Key is at approximately 6dB bellow the expected gain value while the gain of the simulations is constant. Finally, the oscilloscope noise floor is reached around 200 kHz.

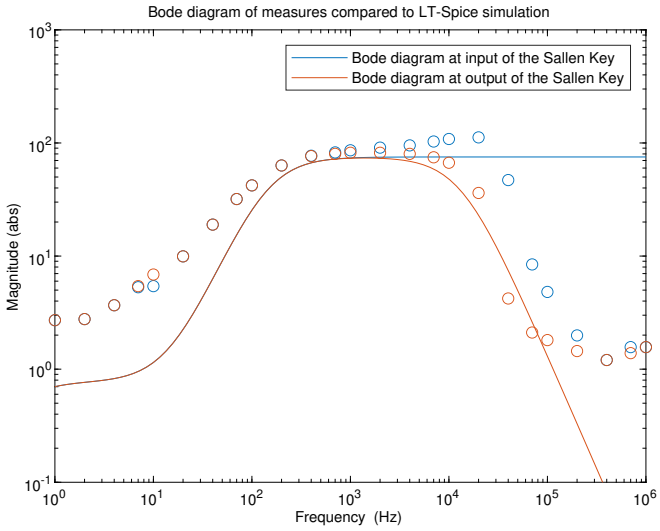

Figure 5.1: *Bode diagram comparing the measures (dots) and the simulations (line).*

5.2.2 Power consumption

The power consumption is measured by the SMU. The SMU is programmed in voltage generator mode and measures the current consumption. The values obtained for signals with an amplitude of 0.3V and 0.15V are given on Figure 5.2. There is a constant consumption of 0.28mA up to 1kHZ. The current consumption then makes a peak with a maximum at 20 kHz approximately. This corresponds to the gain peak on the measured bode diagram (Figure 5.1). As shown on the figure, the current consumption is measured for 2 different wave generation amplitudes. The power consumption has been computed for the maximum artefact value at the input. For frequencies above $250Hz$, (above the peak power frequency range of the artefacts), this amplitude will be much smaller. The current consumption for the half of the maximal amplitude is represented in red in Figure 5.2 since the real amplitude at those voltages will be much smaller (approximately 100 times smaller according to the specifications), the real current consumption can be considered as equal to the baseline: 0.28 mA. The power consumption linked to one discrete IA is:

$$P_{DIA} = 1.8V \cdot 0.28mA = 0.50mW \tag{5.1}$$

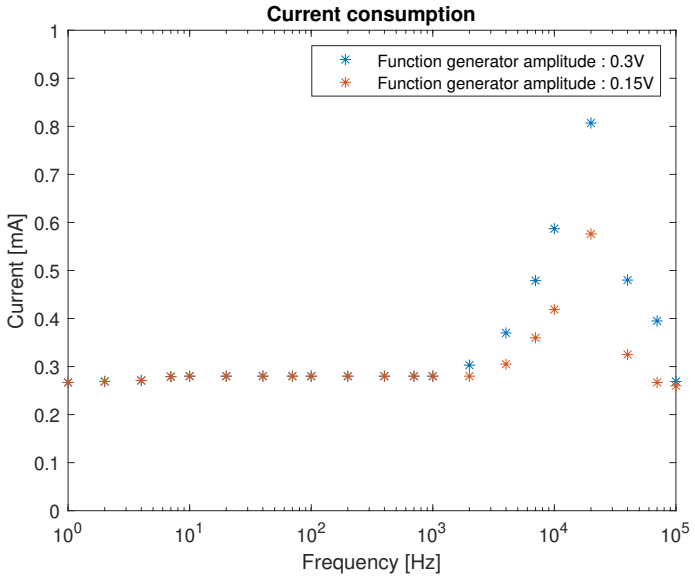

Figure 5.2: *Graph of the consumption in current of the circuit measured by the SMU.*

5.3 Microcontroller

Due to the restriction of material linked to the Covid-19, the adaptive tripole implementation results were simulated with Matlab. Idealy, to verify the real values, tests have to be performed with the global circuit.

Concerning the measures of the power consumption, time management, imbalance correction and ADC noise the test have directly be performed on the microcontroller.

5.3.1 Time management

In order to get a more precise idea of the exact power consumption and the clock frequency to use, it is interesting to perform several tests. To measure the computation time of the different parts of the code, 2 GPIO outputs have been activated as shown on Figure 5.3. The pin were SET and RESET at the beginning and the end of each callback function. Figure 5.4 and 5.5 gives an overview of the time management between the ADC, the interrupts and the cuff imbalance implementation.

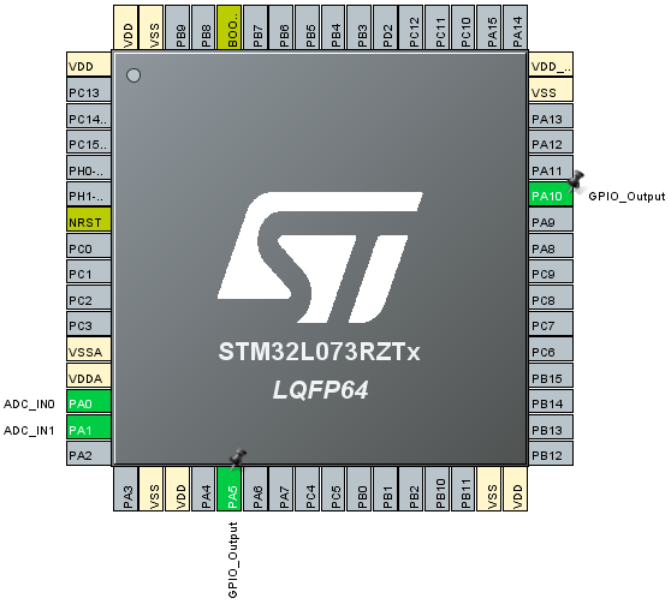

Figure 5.3: *Pin configuration on STMcubeMX for the time management measures.*

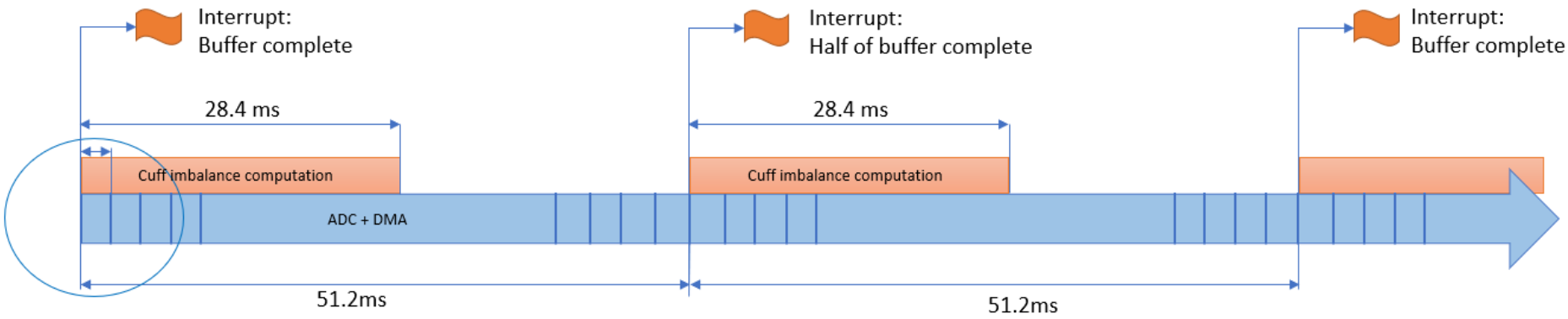

Figure 5.4: *Time overview with in blue the ADC and the transfer of the ADC values with the DMA to a buffer in memory. In red: the time needed for the cuff imbalance computation.*

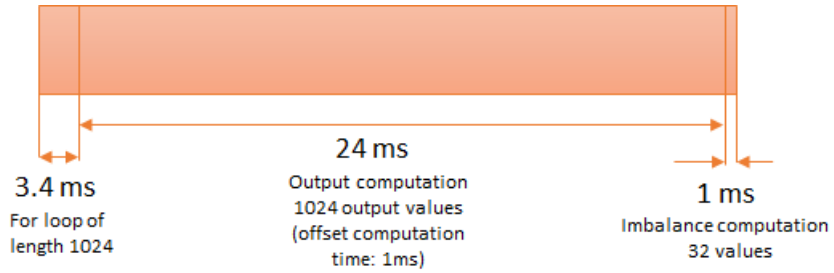

Figure 5.5: *Detailed timing of the cuff imbalance computation.*

The timing of the computation is further detailed in Figure 5.5. The main computation time is spent to the output value computation while the imbalance computation (occuring 32 times on the half of a buffer only needs 1ms computation time). The third main time consuming feature is the for-loop. The other computations outside the for-loop are negligible in comparison to those elements.

5.3.2 Results of some tests to verify the good working of the cuff imbalance implementation

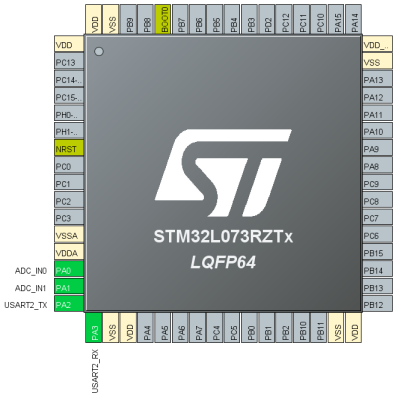

Figure 5.6: *Pin configuration on STM-cubeMX for the cuff imbalance tests.*

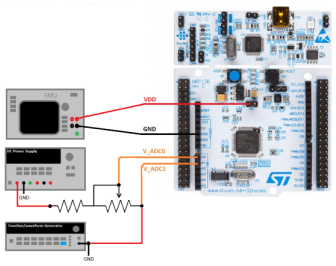

Figure 5.7: *Measurement scheme of a generated imbalanced signal used to verify the good working of the imbalance compensation implementation.*

In order to test the imbalance compensation of the artefact signal, test have been performed on the microcontroller. The ADC still acquires at 20kHz. The data of interest (G_1, G_2, ADC_0, ADC_1 and V_{out}) are transmitted by the UART port without passing by the DMA. The amount of transmitted output data is much more than only the output data, this is the reason why the ADC input signals on Figure 5.8 are distorted. Since the imbalance is constant over time, this does not impact the correctness of the obtained results. The UART pins are consequently activated (as illustrated on Figure 5.6).

For this part, it would be interesting to make some tests on real signals or even to superimpose simulated signals (a signal at 1 kHz with an amplitude of 4.8 mV and a signal at 250 Hz with an amplitude of 0.6 V) and see wether the signal at 1kHz is retrieved or not. Neverthless, the performed tests prove that the imbalance can be computed and the input signals can be correctly compensated with the digital implementation.

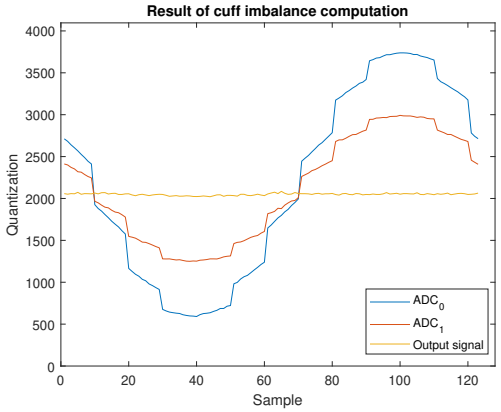

Figure 5.8: *Measures of the two ADC input and the output for a cuff imbalance of 27,6% computed with the microcontroller STM32L073. The used measurement scheme is given in Figure 5.7. As shown on the Figure, the output signal is centred around 2048. With the available material, it was not possible to perform the tests with a small simulated ENG signal. The result was thus supposed to be completely flat, the variance of the signal is only due to noise at the input and the error of the imbalance estimation.*

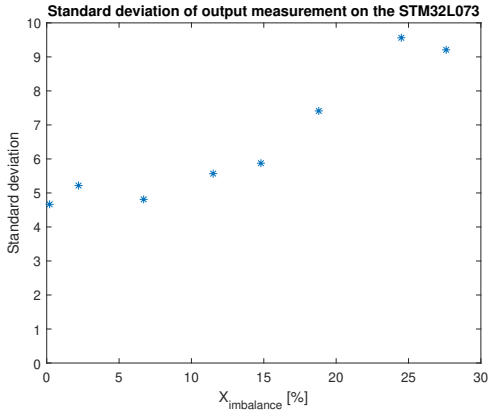

Figure 5.9: *Standard deviation of the output signal in function of the computed imbalance. The standard deviation is given in LSB (1 LSB = 0.44 mV). For a signal with an imbalance of 0%, the standard deviation is equal to 4.7 LSB. In the datasheet, the typical inaccuracy error is 2 LSB and the maximum value is 5 LSB [74]. The variance of one ADC is 3 LSB (see appendix E.3) The variance of the sum of two ADC is 4.24 LSB. This value is close to the measured variance value for small imbalances. When the imbalance increases, the variance of the output signal also increases, this is linked to the imperfect imbalance estimation.*

5.3.3 Low power modes configurations

There are 5 different low power mode configurations: the low power run mode, the sleep mode, the low-power sleep mode, the stop mode and the standby mode. To recall, the ADC clock works at 16MHz[1] and is triggered by Timer 6 at 20 kHz (MSI). The CPU is also drived by an MSI clock (at 4,194 kHz). This is the highest frequency that can be reached with an MSI clock. Since the time of computation is approximately half the time between two callbacks, the CPU frequency cannot be lowered.

- **Low power run mode**: The low power run mode reduces the power consumption in run mode. The clock frequency is lowered to 131 kHz (MSI frequency range 1). This mode can be used in the time lapses where only the ADC is acquired since the ADC peripheral can continues to run besides. During the data processing, this low-power mode cannot be used since the System clock is fixed at 4194kHz.

[1]The ADC clock frequency is independent from the System clock.

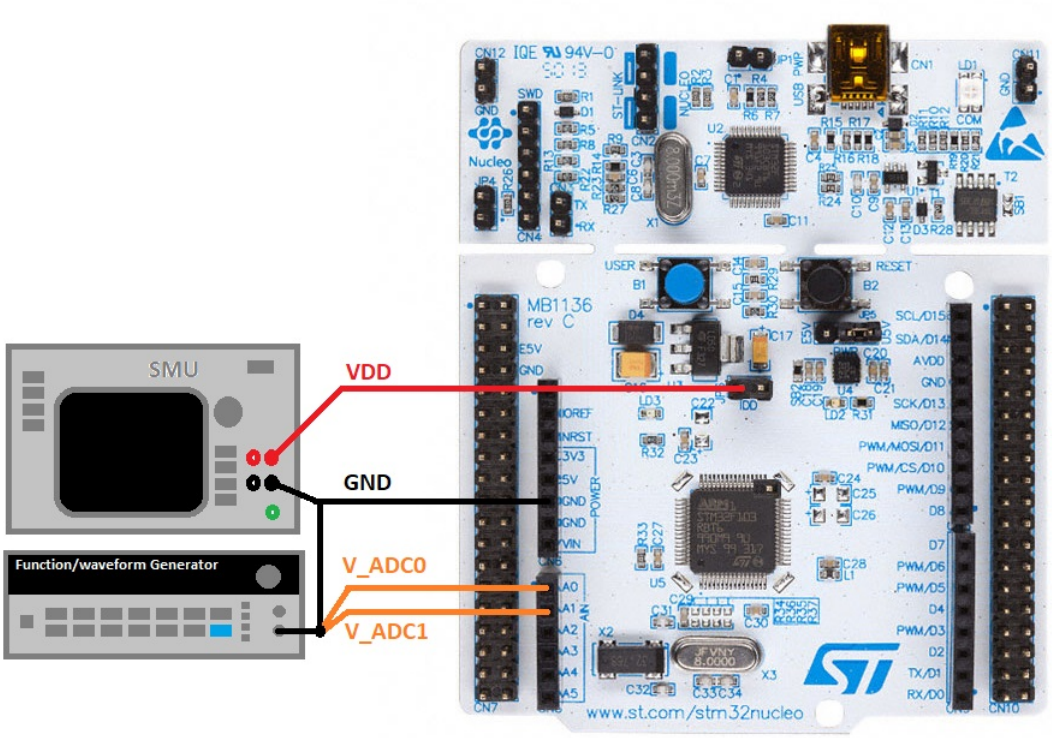

Figure 5.10: *Schematic of the connection of the STM32L073 nucleo board for the power consumption measures.*

	Baseline consumption	Consumption with ADC at 20kHz	Consumption imbalance compensation implementation	Wake up with interrupt	Mean consumption at 20
Nothing	1.42mW	2.78 mW	3.2 mW	Yes	2.99mW
Low power run	1.23 mW	2.42 mW	2.78 mW	Yes	2.60mW
Sleep mode	0.67 mW	1.97 mW	3.2 mW	Yes	2.585mW
Low power sleep	0.67 mW	1.97 mW	3.2 mW	Yes	2.585mW
Stop mode	0.44 mW	-	-	Yes	-
Standby mode	0.33 mW	-	-	No	-

Table 5.1: *Power consumption measured on the microcontroller with the ADC running at 20 kHz.*

- **Sleep mode**: During the Sleep mode, the CPU is stopped. All the peripherals continue to operate and at any interrupt the CPU is woken up. This mode can thus be used for the time lapses where only the ADC is operating.
- **Low power sleep mode**: This mode is a combination of the Sleep mode and the low power run mode: both the clock frequency and the number of enabled peripherals are limited.
- **Stop mode**: In the stop mode, all clocks in the VCORE domain are stopped. Timer 6 (controlled by the MSI) that is necessary for the data acquisition stops running. This mode can consequently not be used for this application.
- **Standby mode**: The VCORE domain powered off, this mode can consequently not be used for this application.

During the data processing, the microcontroller has to work in normal run mode since the CPU cannot run at 4.194MHz in any of the low-power modes. When only the data acquisition is running, the sleep mode can be used. According to the STM32L073 datasheet [74], the ADC is not available in the low-power run and low-power sleep modes. When entering the sleep mode or low-power sleep mode, a wait-for-interrupt or wait-for-event instruction must be given. Each time an event or interrupt occurs, the sleep mode is exit. At each rising edge of the Timer 6, an event is sent to trigger the ADC. Besides, for the DMA request, an interrupt is sent to the DMA at the end of each conversion to send the data to the input buffer in memory (cf. Section 3.2). The power consumption lowering by using a sleep mode for the time lapse when only the data acquisition is consequently quite small (0.3mW) compared to the normal run mode.

5.4 Result of matlab Simulations

The different signals obtained with the matlab simulations are detailed on Figure 5.11. At the input the voltage difference between two electrodes is illustrated, at the output of the integrated IA, the positive and negative output of one IA is illustrated, At the microcontroller level, the amplitudes are given in LSB. The value of one LSB is 0.44mV. The output signal represent the recovered neural signal. The amplitude is also given in LSB since the output can either be given be computed by the DAC or the UART.

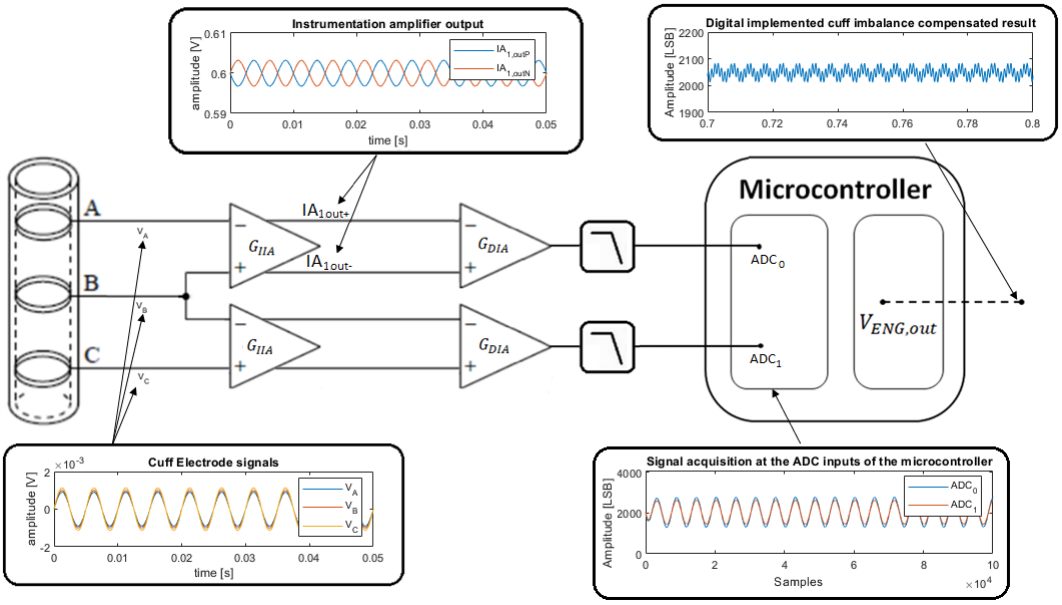

Figure 5.11: *Overview of the different simulated signals at the different stages of the circuit.*

The signal obtained at the output of the microcontroller is compared to the imbalance compensation with the exact cuff imbalance and the result obtained with the true tripole implemetation on Figure 5.12.

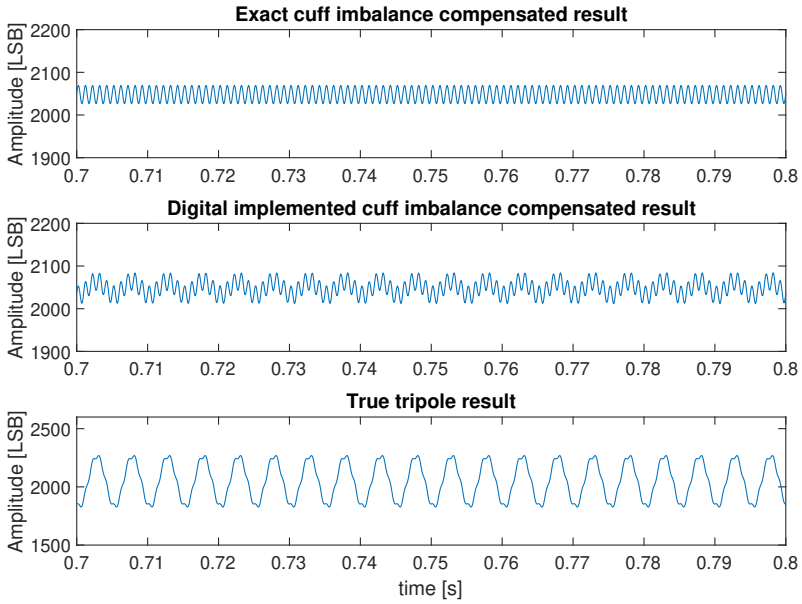

Figure 5.12: *Signals obtained with an imbalance value of 10%. This figure highlights the comparison between the signal compensated with the exact imbalance value, the signal compensated with the gain computed as in the digital implementation and the true tripolar implementation.*

The imbalance computed with the matlab simulation is compared to the real cuff

imbalance on Figure 5.13. Finally, the signal to interference ratio is computed for the true tripole and digital adaptive tripole implementation on matlab (Figure 5.14). For a cuff without imbalance, the result computed with the true tripole is much better than the digitally implemented adaptive tripole. For a cuff with imbalances, the digitally adapted tripole model shows generally better results. The simulations have been performed on a ENG signal of $1\mu V$. The digitally implemented adaptive tripole shows a constant SIR of approximately 4dB while the SIR of the true tripole implementation deteriorates when some cuff imbalance is present.

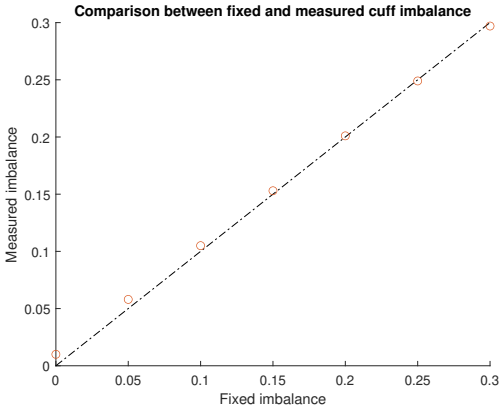

Figure 5.13: *Comparison of the computed imbalance value with the exact imbalance value..*

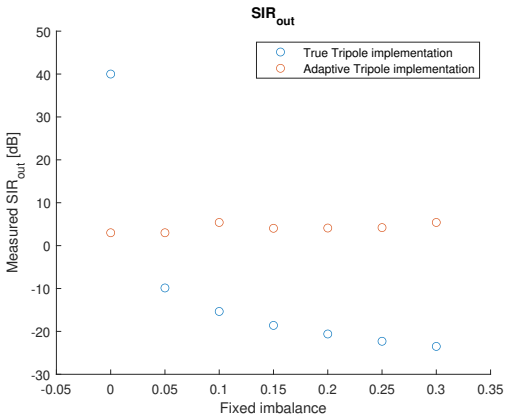

Figure 5.14: *SIR value*

5.5 Result comparison with similar works and discussion of the limitations of the system

The obtained results are compared to similar works in Table: 5.2. The results of this work are only based on simulations and the signal specifications are based on a comparison of different works and has not been tested with real signals. Moreover, the results obtained by the tests are performed on each block separately. Ideally tests have to be made on the global system to validate the correctness of the presented results.

	Rahal [12]	Triantis [13]	Shon [75]	WINeRS8 [76]	Stumpp [9]	This work
Stimulation	No	No	Yes	Yes (before)	Yes	No
Recording	Yes	Yes	Yes	Yes	Yes	Yes
SIRout	2.74dB	5.02dB	5.46 dB	2 dB	-	4dB
Power consumption [mW]	-	5	18.48	18.9	-	3.8
Simulation (S) / Animal tests (A)	S	S + A	S + A	A	A	S
Sampling rate [Hz]	-	20 - 25 k	10k	-	80k	20k
Year	2001	2005	2018	2018	2020	2020

Table 5.2: *Comparison of the obtained performances with other peripheral nerve sensing designs.*

In [75] another neural acquisition combined with a stimulation circuit implementation is proposed. The results were also based on simulated signals. They used a quasi-tripole implementation instead of a cuff-imbalance compensation implementation. They mentioned that the use of 2 central electrodes considerably increased the signal-to-interference ratio. Concerning the amplification levels, their instrumentation amplifier (preamplifier) did not implement directly some filters. The filters are added after the intrumentation amplifier. The filter is composed of 2 bandpass and 2 low-pass filters. Two programmable gain amplifiers amplify the signal and finally a blanking circuit is put at the end.

The comparison between this work and other similar studies of Table 5.2 is discussed in the following items:

- This work only takes the **recording** of signals into account.
- The SIR_{out} is comparable to the results obtained in the other works.
- The **power consumption** is slightly bellow the value of the other works. Neverthless, it is important to remind that the computed power consumption does not take the output of the signal into account. Since on this Nucleo board, the ADC is not available in low-power mode and the sleep mode wakes up at each DMA request, further lowering the power consumption on this microcontroller will be complicated. Neverthless, the power consumption can probably be lowered by using a microcontroller more adapted to long-term biological implants. The choice of the operational amplifier for the discrete IA could also be better by not limiting the type to DIP operational amplifiers.

  In order to compare the obtained power consumption with other typical biological implants, Table 5.3 of [77] summarises different implants with their typical power consumption.

Implant	Power consumption
Cochlear	5.16 mW
Drug Pump	400 μW
Neurostimulator	50 μW
Muscle stimulator	1.3 mW
Pacemaker	8 μW

Table 5.3: *Power consumption comparison of different biological implants.*

- The **sampling rate** is comparable to the data recording rate of the other works except [9]. The sampling rate directly influences the power consumption. Since the data processing time is fixed, increasing the sampling rate reduces the time where the micro-controller acquires data in sleep mode. Lowering the sampling rate would deterior the output signal since the ENG signal goes up to $10kHz$.

More specifically to this work the following points are interesting to highlight:

- The **noise** is relatively high compared to the signal amplitude. The noise level can be lowered by reducing the band pass frequency. The frequency band has been chosen large enough in order to have a flat gain at the peak power ENG frequency. The frequency band may probably be smaller, but this has to be confirmed with real epileptic signal values.

- The **imbalance computation** can also be optimised with real tests. The time to completely change of cuff imbalance is now fixed at 1.64s. To change this value, the number of elements in the storage vector has to be changed. The number of computations of x_{imb} per for loop can also be changed. The time of the imbalance computation depends of this value as wel as the power consumption and the type of value must also be adapted.

- The digital implementation can also be enhanced by **calibrating the half-of-range value**. This value is initially fixed at 2048 but this offset can vary from device to device and between the different ADC inputs of a same device.

- The **discrete IA gain** can also be modified in function of the real voltage difference between two electrodes. The gain bandwidth of the MCP624 operational amplifier is $550kHz$, keeping the same cut-off frequency (13.4 kHz) the maximum gain of one operational amplifier is $41V/V$ this means that the maximal gain of the differential IA is:

$$\max(G_{DIA}) = (41V/V \cdot 2 + 1) \cdot 41V/V = 3.4 \cdot 10^3 V/V \tag{5.2}$$

  To determine the best suited gain value, tests have to be performed with signals closer to the reality.

Chapter 6

Conclusion

Epilepsy is a handicapping disorder due to disturbed electrical rhytms in the central nervous system and causes seizures. Typical symptoms as convulsions, blackouts or uncontrolled movements can lead to severe complications for the patient. One third of the cases cannot be cured with ASD. An alternative for those patients is to lower the number of seizures with VNS.

In actually commercialised medical VNS systems, 3 modes of working are available [8]:

- The normal mode: an open-loop mode with a determined stimulation pattern
- The magnet mode: mangnet on-demand stimulation
- The auto-stimulation mode: seizures are detected by an increasing heart rate, this mode is often combined with the normal mode

To improve the impact of VNS, detecting the start of seizures on neural activity recordings of the vagus nerve activity seems to be a solution [9].

The main issue of the recording of the neural activity of a peripheral nerve (in this case: the vagus nerve) is the very low signal-to-interference ratio. The neural signal is in the μV range while the interfering artefacts (linked to breath, cardiac rhythm and muscular activity) are in the mV range.

The cuff electrode has a linearization effect on the artefacts, the tripolar model uses this characteristic to remove the artefacts and the neural signal can be retrieved. The ideal cuff model considers that the distances between the electrodes are perfectly equal and that the cuff and nerve impedances between the electrodes are equal to. This is not verified in real applications, the imperfections linked to the cuff electrodes are called **cuff imbalances**. To take those imbalances into account, an adaptive tripole implementation has been proposed in [12] and tested in [13].

The inovation of this thesis is to propose a digital implementation of the adaptive tripole. A continuous data acquisition runs in background while the data processing

is computed each time the DMA sends a callback interrupt.

The ADC acquires the signals on 12 bits with an input voltage range of 1.8V. The cuff electrode signals have been amplified with a total gain of $4.77 \cdot 10^3 V/V$. The different amplifier stages are summarised in table 6.1.

	gain [V/V]	filter	cut-off frequency [Hz]
integrated IA	63.8	-	-
discrete IA	75	high-pass filter	159
Sallen-Key	1	low-pass filter	13.4k

Table 6.1: *Summary of the different amplifier stages with their gain and filter function.*

To verify the working of the different blocks, some tests have been performed on the discrete IA and the microcontroller. Due to the Covid 19, the available material was restricted, so performing tests on the whole circuit was not possible. Neverthless, a simulation has been performed in order to get a global idea of the evolution of the signals through the circuit. The following items summarise the different obtained results.

- The total **gain** of the analog amplification is $4.77 \cdot 10^3 V/V$
- The **input referred noise** is $2.5 \mu V_{RMS}$.
- The total **power consumption** is 3.8 mW. (Microcontroller: 2.59mW + discrete IA : 0.28mW + integrated IA : 0.023mW)
- The **signal-to-interference ratio** (SIR_{out}) simulation output ratio is of 4 dB.

The digital implementation can thus further be improved by :

- **Reducing the noise and interference**: by reducing the band-pass filter in function of the frequency range of the epileptic signal.
- **Lowering the power consumption**:
  - by finding a micro-controller that works with a reduced power consumption at high frequencies (for the data processing) and that works in low power mode in combination with the ADC.
  - by searching a more suited operational amplifier without taking the DIP-type into account.

Finally, the digital adaptive tripole implementation can also be used to record neural signals on other peripheral nerves. In this study, the specific case of refractory has been studied, nevertheless, other peripheral nerve recording applications could benefit from this work.

Bibliography

[1] Association of Neurological Surgeons American. *Epilepsy*, accessed July 2020. https://www.aans.org/en/Patients/Neurosurgical-Conditions-and-Treatments/Epilepsy.

[2] Mayo Clinic. *Epilepsy*, (accessed July 17, 2020). https://www.mayoclinic.org/diseases-conditions/epilepsy/symptoms-causes/syc-20350093.

[3] Dr. Henri RUBINSTEIN. *Chiffres clés et prévalence de l'épilépsie*, 05/08/2018 (accessed July 17, 2020). https://www.carenity.com/infos-maladie/epilepsie/chiffres-cles-et-prevalence-381.

[4] Patrick Kwan and Martin J. Brodie. Early identification of refractory epilepsy. *New England Journal of Medicine*, 342(5):314–319, 2000. PMID: 10660394.

[5] WebMD. *Help When Epilepsy Treatment Doesn't Work*, (accessed July 17, 2020). https://www.webmd.com/epilepsy/refractory-epilepsy?prop16=vb4t&tex=vb4t.

[6] Masoud Farivar Joyel Almajano Amirhossein Shahshahani Alexandre Schmid Anatol Bragin Yusuf Leblebici Azita Emami Mahsa Shoaran, Masoud Shahshahani. A 16-channel 1.1mm2 implantable seizure control soc with sub-µw/channel consumption and closed-loop stimulation in 0.18µm cmos. 6 2016.

[7] et al. Boon P. *A prospective, multicenter study of cardiac-based seizure detection to activate vagus nerve stimulation*, 2015. https://www.seizure-journal.com/article/S1059-1311(15)00218-6/fulltext.

[8] VNS Therapy. Sentiva technical guide. 2019.

[9] Lars Stumpp, Hugo Smets, Simone Vespa, Joaquin Cury, Pascal Doguet, Jean Delbeke, Emmanuel Hermans, Christian Sevcencu, Thomas N. Nielsen, Antoine Nonclercq, and Riem El Tahry. Recording of spontaneous vagus nerve activity during pentylenetetrazol-induced seizures in rats. *Journal of Neuroscience Methods*, 343:108832, 2020.

[10] J. J. Struijk, M. Thomsen, J. O. Larsen, and T. Sinkjaer. Cuff electrodes for long-term recording of natural sensory information. *IEEE Engineering in Medicine and Biology Magazine*, 18(3):91–98, 1999.

[11] W. M. Grill and J. T. Mortimer. Stability of the input-output properties of chronically implanted multiple contact nerve cuff stimulating electrodes. *IEEE Transactions on Rehabilitation Engineering*, 6(4):364–373, 1998.

[12] Mouhamed Saleh Rahal. Optimisation of nerve cuff electrode recordings for functional electrical stimulation applications. July 2001.

[13] Iasonas F.Triantis. An adaptive amplifier for cuff imbalance and interference reduction in nerve signal recording. (6), 6 2005.

[14] STMicroelectronics. *Ultra-low-power STM32L0x3 advanced Arm®-based 32-bit MCUs*, 12 2017. Reference manual.

[15] Renata Van Woensel Güngör Karakaya, Rudy Van Tielen. L'épilepsie en belgique. *Mutualités Libres*, pages 8–10, 1 2017.

[16] La rédaction de Doctissimo. *Qu'est-ce que l'épilepsie ?*, accessed July 2020. `https://www.doctissimo.fr/html/dossiers/epilepsie/sa_3687_epilepsie_definition.htm`.

[17] Bauer B. Tang F, Hartz AMS. Drug-resistant epilepsy: Multiple hypotheses, few answers. *Frontiers in Neurology*, July 2017.

[18] Kenneth D. Laxer, Eugen Trinka, Lawrence J. Hirsch, Fernando Cendes, John Langfitt, Norman Delanty, Trevor Resnick, and Selim R. Benbadis. The consequences of refractory epilepsy and its treatment. *Epilepsy Behavior*, 37:59 – 70, 2014.

[19] B.N.Harding M.V.Squier S.M. Sisodiya, W.-R. Lin and M. Thom. Drug resistance in epilepsy: expression of drug resistance proteins in common causes of refractory epilepsy. *Med Biol Eng Comput*, pages 22–31, 2002.

[20] *CardiovascularNervous System*, accessed July 2020. `https://sites.google.com/site/cvsns123/nervous-system/peripheral-nervous-system`.

[21] lumencandela. *Introduction to the Nervous System*, Accessed July 2020. `https://courses.lumenlearning.com/boundless-ap/chapter/introduction-to-the-nervous-system/`.

[22] Magdalena R. *Epilepsy, active and impaired functions of the nervous system*, July 2014 (accessed July 17, 2020). `https://www.slideshare.net/MagdalenaReszke/epi-37166883`.

[23] Fitzpatrick D et al. editors. Purves D, Augustine GJ. Summation of synaptic potentials. *Neuroscience. 2nd edition.*, 2001.

[24] Molecular Devices. *What is an action potential?*, (accessed July, 2020). `https://www.moleculardevices.com/applications/patch-clamp-electrophysiology/what-action-potential`.

[25] Alexander Schmid. In *Bioelectronics and biomedical microelectronics EE-519*, chapter 3-5-6-8. Academic Press, EPFL, Switzerland, 2019.

[26] Neil V. Watson and S. Marc Breedlove. *The Mind's Machine, Second Edition*, 2016. https://2e.mindsmachine.com/figures/03/03.07.html.

[27] Kendra Cherry. *How Many Neurons Are in the Brain?*, April 10, 2020. https://www.verywellmind.com/how-many-neurons-are-in-the-brain-2794889.

[28] Francesco PAVONE Sabine BRADLER Katrin AMUNTS, Jean-Francois MANGIN. Human brain organization. *HBP SCIENCE MARKET*, July 2017.

[29] Mayo Clinic. *EEG electrodes*, (accessed July 2020). https://www.mayoclinic.org/tests-procedures/eeg/multimedia/eeg-electrodes/img-20005916.

[30] Encyclopædia Universalis. *Électrocorticogramme*, accessed July 2020. https://www.universalis.fr/dictionnaire/electrocorticogramme/.

[31] L. Sales Ferreira Caboclo, E. Garzon, F. Saori Miyashira, Henrique Carrete Jr, Ricardo da Silva Centeno, Elza M. Targas Yacubian, and Americo Ceiki Sakamoto. Temporal lobe epilepsy with unilateral hippocampal sclerosis and contralateral temporal scalp seizure onset: report of four patients with "burned-out hippocampus". *Journal of Epilepsy and Clinical Neurophysiology*, 11:79 – 86, 00 2005.

[32] Jodi Cohen. *Vagus Nerve Infection Hypothesis*, accessed July 2020. https://vibrantblueoils.com/vagus-nerve-infection/.

[33] Robert H. Howland. Vagus nerve stimulation. *Current behavioral neuroscience reports*, 1,2:64–73, 10 2014.

[34] Riem El Thary Annelies Grimonprez Ine Dauwe Veerle De Herdt Alfred Meurs Wytse Wadman Paul Boon Lies Mollet, Robrecht Raedt Jean Delbeke and Kristl Vonck. Electrophysiological responses from vagus nerve stimulation in rats. *International Journal of Neural Systems Vol. 23, No. 6*, (8), 8 2013.

[35] Ligue fracophone belge contre l'épilepsie. *Traitement*, accessed July 2020. https://ligueepilepsie.be/+-Traitement-+.html.

[36] National Institute of Neurological Disorders and Stroke. *The Epilepsies and Seizures: Hope Through Research*, June 2020. https://www.ninds.nih.gov/Disorders/Patient-Caregiver-Education/Hope-Through-Research/Epilepsies-and-Seizures-Hope-Through#top.

[37] Stella Manta. Effets neurophysiologiques de la stimulation du nerf vague : Implication dans le traitement de la dÉpression rÉsistante et optimisation des paramÈtres de stimulation. *International Journal of Neural Systems Vol. 23, No. 6*, 1 2012.

[38] American Association of Neurological Surgeons. *Deep Brain Stimulation*, accessed July 2020. https://www.aans.org/en/Patients/Neurosurgical-Conditions-and-Treatments/Deep-Brain-Stimulation.

[39] Cyberonics. *The Vagus Nerve Stimulator*, June 2017. https://www.epilepsy.org.uk/sites/epilepsy/files/images/advice/vns_cyberonics.jpg.

[40] Nicolò Lago ID and Andrea Cester. Flexible and organic neural interfaces: A review. *Applied sciences*, December 2017.

[41] L. Diambra, J.C.Bastos de Figueiredo, and C.P. Malta. Epileptic activity recognition in eeg recording. *Physica A: Statistical Mechanics and its Applications*, 273(3):495 – 505, 1999.

[42] Nobukazu Nakasatp, Michel F. Levesque, Daniel S. Barth, Christoph Baumgartner, Robert L. Rogers, and William W. Sutherling. Comparisons of meg, eeg, and ecog source localization in neocortical partial epilepsy in humans. *Electroencephalography and Clinical Neurophysiology*, 91(3):171 – 178, 1994.

[43] Christopher E. Larson and Ellis Meng. A review for the peripheral nerve interface designer. *Journal of Neuroscience Methods*, 332:108523, 2020.

[44] T Stieglitz, H Beutel, and J.-U Meyer. A flexible, light-weight multichannel sieve electrode with integrated cables for interfacing regenerating peripheral nerves. *Sensors and Actuators A: Physical*, 60(1):240 – 243, 1997. Proceedings of Eurosensors X.

[45] Brian Wodlinger, Yazan Dweiri, and Dominique M. Durand. Chapter 9 - biochips: Electrical biosensors: Peripheral nerve sensors. In Swarup Bhunia, Steve J.A. Majerus, and Mohamad Sawan, editors, *Implantable Biomedical Microsystems*, pages 203 – 214. William Andrew Publishing, Oxford, 2015.

[46] Andreu D Azevedo-Coste C Stieglitz T Navarro X Badia J, Boretius T. Comparative analysis of transverse intrafascicular multichannel, longitudinal intrafascicular and multipolar cuff electrodes for the selective stimulation of nerve fascicles. *Journal of neural engineering*, June 2011.

[47] J.J. Struijk. The extracellular potential of a myelinated nerve fiber in an unbounded medium and in nerve cuff models. *Biophysical Journal*, 72(6):2457 – 2469, 1997.

[48] Jean Gotman Maeike Zijlmans, Danny Flanagan. Heart rate changes and ecg abnormalities during epileptic seizures: prevalence and definition of an objective clinical sign. (8), 8 2002.

[49] Health news review. *Understanding medical tests: sensitivity, specificity, and positive predictive value*, accessed July 2020. https://www.healthnewsreview.org/toolkit/tips-for-understanding-studies/understanding-medical-tests-sensitivity-specificity-and-positive-predictive-val

[50] Thea Gutter Constantin Ungureanu Pierre Cluitmans Johannes Van Dijk Judith van Andel Francis Tan Al de Weerd Ben Vledder Wytske Hofstra Richard Lazeron Ghislaine van Thiel Kit C B Roes Frans Leijten the Dutch Tele-Epilepsy Consortium Johan Arends, Roland D Thijs. Multimodal nocturnal seizure detection in a residential care setting: A long-term prospective trial. *National Library of Medicine*, November 2018.

[51] Scott E Krahl James McNamara Alan Frazer Thomas R Henry Mark S George Dennis S Charney Stephen K Brannan Neuropsychopharmacology volume Charles B Nemeroff, Helen S Mayberg. Vns therapy in treatment-resistant depression: Clinical evidence and putative neurobiological mechanisms. *Neuropsychopharmacology volume*, 31:pages1345–1355, 2006.

[52] Wissam Deeb, James J. Giordano, Peter J. Rossi, Alon Y. Mogilner, Aysegul Gunduz, Jack W. Judy, Bryan T. Klassen, Christopher R. Butson, Craig Van Horne, Damiaan Deny, Darin D. Dougherty, David Rowell, Greg A. Gerhardt, Gwenn S. Smith, Francisco A. Ponce, Harrison C. Walker, Helen M. Bronte-Stewart, Helen S. Mayberg, Howard J. Chizeck, Jean-Philippe Langevin, Jens Volkmann, Jill L. Ostrem, Jonathan B. Shute, Joohi Jimenez-Shahed, Kelly D. Foote, Aparna Wagle Shukla, Marvin A. Rossi, Michael Oh, Michael Pourfar, Paul B. Rosenberg, Peter A. Silburn, Coralie de Hemptine, Philip A. Starr, Timothy Denison, Umer Akbar, Warren M. Grill, and Michael S. Okun. Proceedings of the fourth annual deep brain stimulation think tank: A review of emerging issues and technologies. *Frontiers in Integrative Neuroscience*, 10:38, 2016.

[53] globenewswire. *Medtronic Receives CE Mark Approval for the Percept™ PC Neurostimulator DBS System with BrainSense™ Technology*, January 09, 2020. `https://www.globenewswire.com/news-release/2020/01/09/1968375/0/en/Medtronic-Receives-CE-Mark-Approval-for-the-Percept-PC-Neurostimulator-DBS-Sys` `html`.

[54] Medtronics. *FDA Approves First-Of-Its-Kind Percept™ PC Neurostimulator with BrainSense™ Technology*, June 25, 2020. `http://newsroom.medtronic.com/news-releases/news-release-details/fda-approves-first-its-kind-percepttm-pc-neurostimulator/`.

[55] Medtronics. *PERCEPT™ PC NEUROSTIMULATOR, Neurostimulator for Deep Brain Stimulation Therapy.*

[56] Andreas Demosthenous, John Taylor, Iasonas Triantis, Robert Rieger, and N. Donaldson. Design of an adaptive interference reduction system for nerve-cuff electrode recording. *Circuits and Systems I: Regular Papers, IEEE Transactions on*, 51:629 – 639, 05 2004.

[57] Joaquin Hoffer. *Techniques to Study Spinal-Cord, Peripheral Nerve, and Muscle Activity in Freely Moving Animals*, volume 21, pages 65–145. 02 2008.

[58] Lotte Struijk and Johannes Struijk. Signal strength versus cuff length in nerve cuff electrode recordings. *Biomedical Engineering, IEEE Transactions on*, 49:1045 – 1050, 10 2002.

[59] Andreas Demosthenous Iasonas F.Triantisa. Electrophysiological responses from vagus nerve stimulation in rats. *Medical engineering and physics*, 30, 6 2008.

[60] N. Donaldson M. Rahal, J. Taylor. The effect of nerve cuff geometry on interference reduction: a study by computer modeling. *IEEE Transactions on Biomedical Engineering*, 30, 1 2000.

[61] D. M. Durand W. Tesfayesus, P. Yoo. Blind source separation of nerve cuff recordings. (9), 9 2003.

[62] Johannes Struijk and M. Thomsen. Tripolar nerve cuff recording: stimulus artifact, emg and the recorded nerve signal. volume 2, pages 1105 – 1106 vol.2, 10 1995.

[63] ST. *STM32 Nucleo-64 development board with STM32L073RZ MCU, supports Arduino and ST morpho connectivity*, accessed July 2020. `https://www.microchip.com/wwwproducts/en/MCP6001`.

[64] Electronics Tutorials. *The Differential Amplifier*, Accessed July 2020. `https://www.electronics-tutorials.ws/opamp/opamp_5.html`.

[65] Microchip. *MCP6001/1R/1U/2/4 1 MHz, Low-Power Op Amp*, accessed July 2020. `https://www.stmicroelectronics.com.cn/en/evaluation-tools/nucleo-l073rz.html`.

[66] Microchip. *MCP621/1S/2/3/4/5/9 20 MHz, 200 µV Op Amps with mCal*, accessed July 2020. `https://www.microchip.com/wwwproducts/en/MCP624`.

[67] Microchip. *MCP601/1R/2/3/4 2.7V to 6.0V Single Supply CMOS Op Amps*, accessed July 2020. `https://www.microchip.com/wwwproducts/en/MCP604`.

[68] Farnell Texas Instruments. *LM6132BIN/NOPB Operational Amplifier, 2 Amplifier, 10 MHz, 14 V/µs, 1.8V to 24V, DIP, 8 Pins*, accessed July 2020. `https://be.farnell.com/texas-instruments/lm6132bin-nopb/op-amp-dual-10mhz-14v-us-dip-8/dp/3004643`.

[69] Texas Instruments. *LM614 Quad Operational Amplifier and Adjustable Reference.* `https://www.ti.com/product/LM614-MIL`.

[70] Texas Instruments. *LM10CLN/NOPBOperational Amplifier, 2 Amplifier, 0.05 MHz, 0.2 V/µs, 1.1V to 7V, DIP, 8 Pins*, accessed July 2020. `https://be.farnell.com/texas-instruments/lm10cln-nopb/ic-op-amp-single-570ma-8-dip/dp/3116991?st=LM10CLN/NOPB`.

[71] ANALOG DEVICES. *OP90GPZ Operational Amplifier, Single, 1 Amplifier, 20 kHz, 0.012 V/µs, 1.6V to 36V, DIP, 8 Pins*, accessed July 2020. `https://be.farnell.com/analog-devices/op90gpz/ic-op-amp-precision-dip8/dp/9604669?st=OP90GPZ`.

[72] ANALOG DEVICES. *OP290GPZ Operational Amplifier, Dual, 2 Amplifier, 20 kHz, 0.012 V/µs, 1.6V to 36V, DIP, 8 Pins*, accessed July 2020. https://be.farnell.com/analog-devices/op290gpz/op-amp-dual-micropower-20khz-8dip/dp/9604731?ost=OP290GPZ.

[73] R. Sarpeshkar, T. Delbruck, and C. A. Mead. White noise in mos transistors and resistors. *IEEE Circuits and Devices Magazine*, 9(6):23–29, 1993.

[74] STMicroelectronics. *Ultra-low-power Arm Cortex-M0+ MCU with 192 Kbytes Flash, 32 MHz CPU, USB, LCD*, 2019. Datasheet.

[75] Ahnsei Shon, Jun-Uk Chu, Jiuk Jung, Hyungmin Kim, and Inchan Youn. An implantable wireless neural interface system for simultaneous recording and stimulation of peripheral nerve with a single cuff electrode. *Sensors*, 18(1), 2018.

[76] Koripalli M.K. Jia Y. et al. Lee, B. An implantable peripheral nerve recording and stimulation system for experiments on freely moving animal subjects. *Sci Rep*, 8, 2018.

[77] Meriam Gay Bautista, Eryk Dutkiewicz, and Michael Heimlich. Subthreshold energy harvesters circuits for biomedical implants applications. In *BODYNETS*, 2015.

[78] E.S.F epilepsy.seizures.fits. *Epilepsy Seizure Symptoms*, accessed July 2020. https://epilepsyseizuresfits.wordpress.com/symptoms/.

[79] electronicsnotes. *Op Amp Slew Rate: details; formula; calculator*, accessed July 2020. https://www.electronics-notes.com/articles/analogue_circuits/operational-amplifier-op-amp/slew-rate.php.

Appendix A

Illustration of epicenter-related symptoms

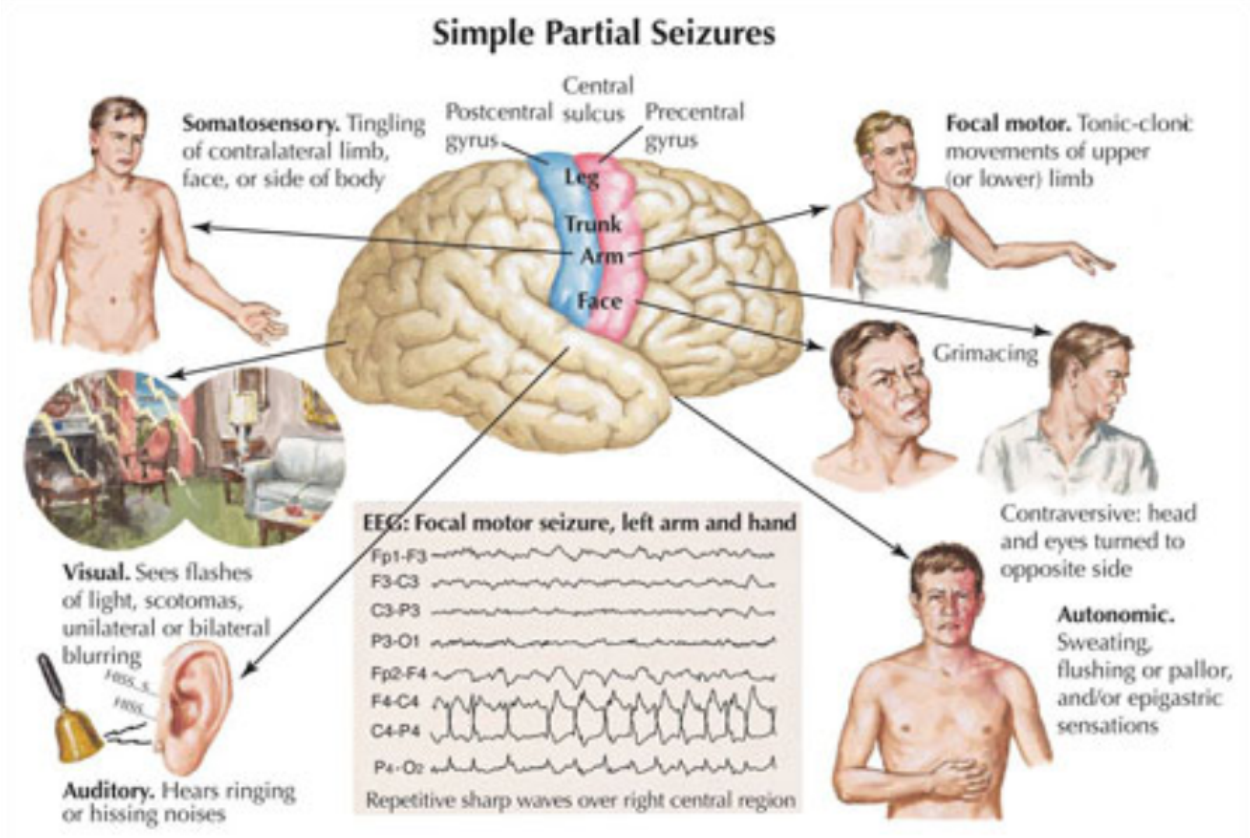

Figure A.1: Examples of different symptoms in function of the seizure initiation region (Source: [78]).

Appendix B

Adaptive tripole shematic

The analog implementation of the adaptive tripole used in the thesis of Rahal [12] and Triantis [13] is presented in Figure B.1. The feedback loop directly adapts the gains inside the G_1 and G_2 operational amplifiers thanks to feedback voltage $V_{fb}(t)$.

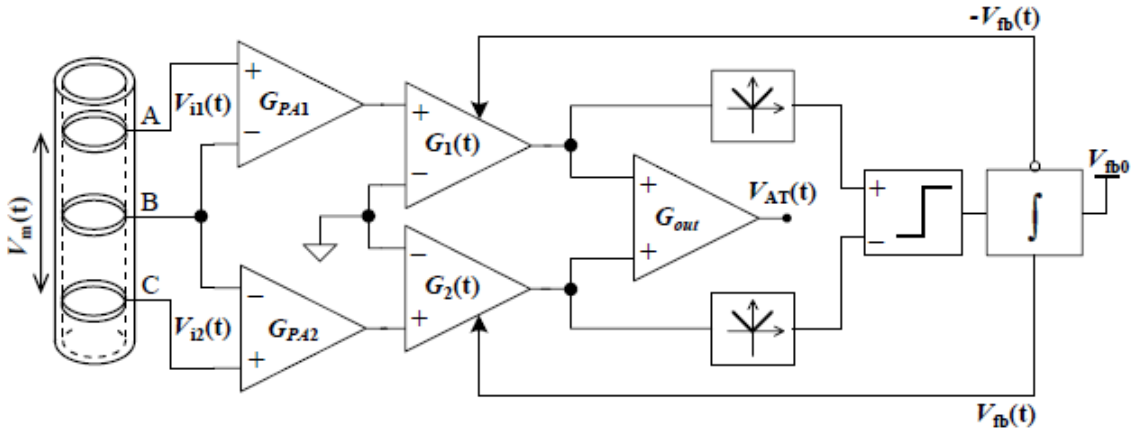

Figure B.1: Adaptive tripole solution to compensate the cuff imbalance (Source: [12, 13]).

Appendix C

Implementation of cuff imbalance computation on microcontroller in C++

The code in the callback function is the following:

```
void HAL_ADC_ConvHalfCpltCallback(ADC_HandleTypeDef* hadc){
    /* Callback initialisation*/

    // index incrementation of the storage vector SV
    if (j<32)
        j = j+1;
    else
            j = 0;

    // Initialisation of SumOfG1 this corresponds to 32*G0
    SumOfG1 = 32000;

    /* For Loop */
    for (i = 0; i<ADC_BUF_LEN/2; i = i+2){
        if(i%16==0){
            //x_imb computation
            SumOfG1 = SumOfG1 + ((abs(input_buf[i] - 2048) -
                abs(input_buf[i+1] - 2048))*1000)/(abs(input_buf[i]
                - 2048) + abs(input_buf[i+1] - 2048));
        }
        output_buf[i/2] = 2048 + (G_1*input_buf[i] -
            G_2*input_buf[i+1])/1000;
    }

    /* Gain computation*/
    // New sum value computation
    sum = sum - SV[j] + SumOfG1;
    // Storage of new value in the Storage Vector (SV)
    SV[j] = SumOfG1;
    // Gain computation
    G_2 = sum/1024;
    G_1 = 2000 - G_2 ;
}
```

As mentionned in the software cuff imbalance implementation part, the sum of G_1 values are computed instead of x_{imb} to avoid negative values. Besides, the values are multiplied by 1000 to keep the uint16_t type and avoid float values. Float values are of size 32 or 64 and the type conversion takes an important percent of the computation time. By multiplying by 1000, 3 decimals are kept while keeping the same variable type.

Another point to be aware of is the the fact that the value of the index must be adapted in function of the callback function, in order to select the right half of the input buffer.

Appendix D

Comparison of frequency and amplitude specifications of similar works

	Rahal [12]	Triantis [13]	Shon [75]	Stumpp [9]	This work
ENG frequency range [Hz]	800-10k	500 - 10k	3 - 5k	12 - 12k	159 - 13k
Peak power ENG frequency range [Hz]	800 - 2k	1k - 3k	300 - 5k	-	800 - 3k
Simulation ENG frequency [Hz]	1.2k	1k	1.5k	-	1k
ENG amplitude [V]	1 - 10μ	2 - 7 μ	-	5.5 - 11.4 μ	1 - 10 μ
Simulation ENG amplitude [V]	10μ	1 μ	10 μ	-	1μ
Artefact frequency range [Hz]	0 - 3k	1 - 3k	-	1 - 7k	0 - 3k
Peak power artefact frequency range [Hz]	100 - 200	100 - 250	-	-	100 - 250
Simulation artefact frequency [Hz]	100 - 150	100	-	-	200
Artefact amplitude between 2 electrodes [V]	0.1 - 1m	100 μ	-	-	100 - 130 μ
Simulation artefact amplitude difference [V]	1m	0.1 - 1m	-	-	100 - 130 μ

Table D.1: Comparison of the frequency and amplitude specifications of the ENG asa wel as the artefact signals.

Appendix E

Noise gain factor computation detail

E.1 Discrete IA

E.1.1 Voltage noise density

- The noise gain factor at the input of the input buffer opamp corresponds to the global gain of the circuit $\frac{2Z_2+Z_1}{Z_1}\frac{Z_4}{Z_3}$

$$V_{RMS} = \sqrt{v_n^2 \cdot \Delta f \cdot (\frac{2Z_2 + Z_1}{Z_1}\frac{Z_4}{Z_3})^2} = 439.5\mu V_{RMS} \tag{E.1}$$

- The noise gain factor at the input of the input of the differential amplifier is given by: $\frac{Z_4+Z_3}{Z_3}$

$$V_{RMS} = \sqrt{v_n^2 \cdot \Delta f \cdot (\frac{Z_4 + Z_3}{Z_3})} = 47.3\mu V_{RMS} \tag{E.2}$$

The total voltage noise at the input of the IA can be computed as follow:

$$V_{RMS,in,tot} = \sqrt{\sum_i (V_{rms,i} \cdot \text{noise gain factor}/G_{tot})^2} \tag{E.3}$$

The total input reffered voltage noise at the input of the discrete IA is $8.3\mu V_{RMS}$.

E.1.2 Current noise density

- The noise gain factor at the positive input of the op-amp of the input buffers corresponds to the output resistance of the integrated IA: $193k\Omega$. The input reffered noise can directly be computed:

$$V_{RMS} = \sqrt{i_{in}^2 \cdot \Delta f \cdot (193k\Omega)^2} = 88nV_{RMS} \tag{E.4}$$

- The noise gain factor at the negative input of the op-amp of the input buffers corresponds to $\frac{Z_2 Z_4}{Z_3}$

$$V_{RMS} = \sqrt{i_{in}^2 \cdot \Delta f \cdot (\frac{Z_2 Z_4}{Z_3})^2}/G_{tot} = 148nV_{RMS} \tag{E.5}$$

- The noise gain factor at both the positive and negative input of the differential amplifier corresponds to Z_4.

$$V_{RMS} = \sqrt{i_{in}^2 \cdot \Delta f \cdot (Z_4)^2}/G_{tot} = 8.6nV_{RMS} \tag{E.6}$$

Total input reffered current noise : 0.34 μV_{RMS}

E.1.3 Component noise density

The noise of the different components are grouped per impedance. The equivalent circuits are drawn in Figure E.1. The obtained equation is given by:

$$v_{n,Z} = \frac{1}{1 + j\omega RC}[v_{n,C} + j\omega RC v_{n,R}] \tag{E.7}$$

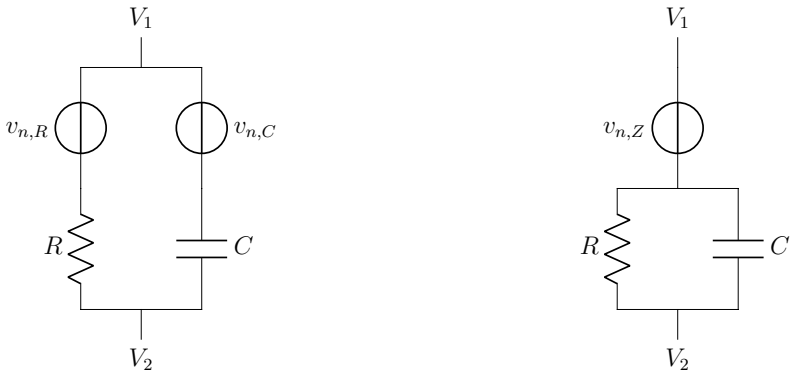

Figure E.1: Equivalent noise circuits

	R $[M\Omega]$	$v_{n,R}$	C $[nF]$	$v_{n,C}$	Z $[k\Omega]$	$\lvert v_{n,Z}\rvert$	ngf	$\lvert v_{n,out}\rvert$	$\lvert v_{n,in}\rvert$
Z_1	10	4.35	3.3	1.12	0.23 -48,23i	4.35	68.8	299.0	3.99
Z_2	2.7	2.26	0.47	2.97	41.81 - 333.38i	2.27	4.94	11.2	0.15
Z_3	-	-	5	0.91	-31.83i	0.91	4.94	4.5	0.06
Z_4	1	1.37	1	2.04	24.70 - 155.22i	1.39	1	1.4	0.02
$v_{n,tot}$								299.2	3.99

Table E.1: D

The noise gain factor are given by the following equations:

$$ngf(Z_1) = \frac{2Z_2 Z_4}{Z_1 Z_3} \tag{E.8}$$

$$ngf(Z_2) = ngf(Z_3) = \frac{Z_4}{Z_3} \tag{E.9}$$

$$ngf(Z_4) = 1 \tag{E.10}$$

E.2 Sallen-Key

For the Sallen-Key, the equations to compute the noise are similar to the ones used for the discrete IA, the only difference is the noise gain factor.

E.2.1 Voltage noise

Noise gain factor:

$$ngf = \frac{(j\omega RC + 1)(j\omega RC + 2) - 1}{(j\omega RC + 1)^2} \tag{E.11}$$

E.2.2 Voltage noise

Noise gain factor:

$$ngf(i_{n,+}) = \frac{R}{(j\omega RC + 1)^2} \tag{E.12}$$

$$ngf(i_{n,-}) = R_{out,MCP624} \tag{E.13}$$

E.2.3 Component gain factor

Noise gain factor:

$$ngf(R_1) = \frac{1}{(j\omega RC + 1)^2} \tag{E.14}$$

$$ngf(R_2) = \frac{1}{(j\omega RC + 1)} \tag{E.15}$$

$$ngf(C_1) = \frac{j\omega RC(j\omega RC + 2)}{(j\omega RC + 1)^2} \tag{E.16}$$

$$ngf(C_2) = \frac{1}{(j\omega RC + 1)} \tag{E.17}$$

$$\tag{E.18}$$

E.3 Histogram of the half-of-range voltage value measured with the ADC.

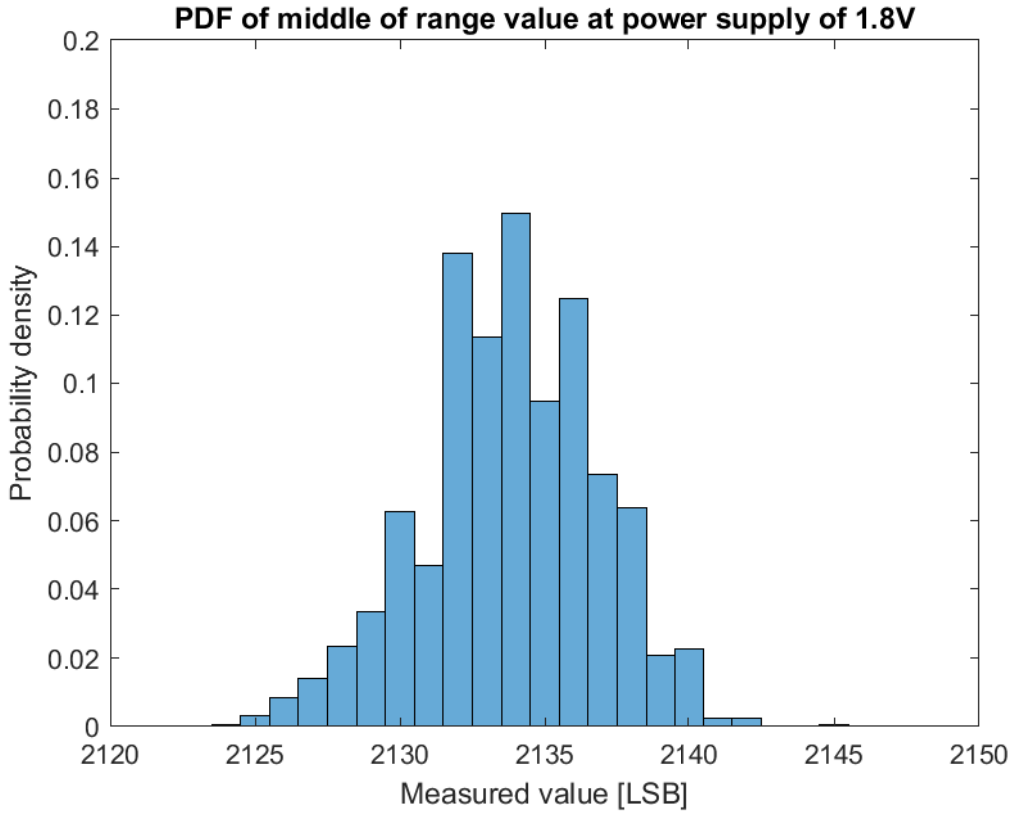

Figure E.2: Histogram of the measured ADC values for an input voltage around 0.9 V. The mean is 2134 LSB and the variance is 3.0 LSB. In the datasheet, the typical total unadjusted error is 2 LSB and the maximum value is 5 LSB [74].

Appendix F

Circuit adaptation for the test measures

F.1 circuit adaptations

In order to perform the tests, some adaptations had to be done: the available material was composed of one function generator, one DC-generator and one source meter unit (SMU).

The input signals $v_{in,+}$ and $v_{in,-}$ normally are 2 waveforms. Since there was only one waveform generator and that the result is expressed in function of $v_{in,+} - v_{in,-}$, only the voltage difference had to be taken into account. One input ($v_{in,-}$) could thus be fixed with a DC value (DC generator) and the other input ($v_{in,+}$) was then fixed with the function generator with the initial amplitude multiplied by 2 as illustrated on Figure F.1. An additional problem concerning the input signals was the amplitude. The minimal amplitude of the Function/waveform generator was of $300mV$ (V_{pp}). While the amplitude of the considered signal was supposed to be of $2 \cdot 8.3mV$. An additional voltage divider had thus to be added. A resistive voltage divider could not be used, because the offset of 0.6 could not be that much amplified. This is why a capacitor had to be added in order to fix the gain linked to the offset to one and the gain of the input waveform could be fixed with the ratio of the resistances. By putting a capacitor between the voltage divider and the ground (see Figure F.2), the

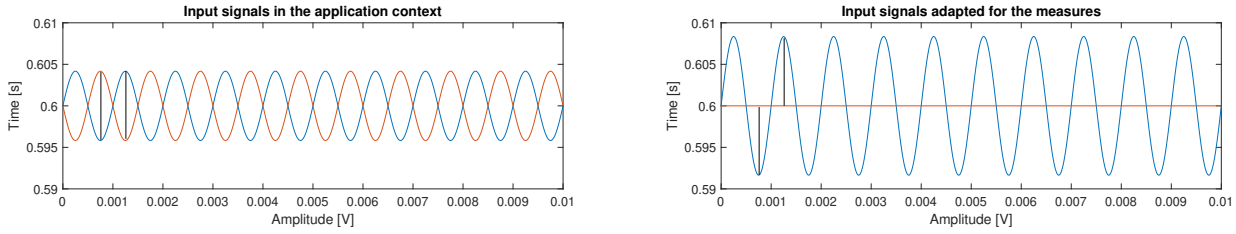

Figure F.1: Input signals of analog amplifier in the acquisition platform context and the measurement context. The figures highlights the voltage difference between the two inputs that has to be the same.

transfer function could be written as follow:

$$H(j\omega) = \frac{1 + j\omega C_1 R_1}{1 + j\omega C_1 (R_1 + R_2)} \tag{F.1}$$

Figure F.2 represents the proposed circuit solution and the corresponding bode diagram. From this equation, the following specifications can be determined:

- The low cut-off frequency is fixed at $\frac{1}{C_1(R_1+R_2)}$
- The high cut-off frequency is fixed at $\frac{1}{C_1 R_1}$
- The offset gain is equal to 1
- The signal gain is fixed at $\frac{R_1}{R_1+R_2}$ V/V

		Target value or target range	Obtained value	Unit
Target specifications	DC Gain	1	1	V/V
	AC Gain	1/36[1]	1/34	V/V
	High cut-off frequency	<100	16	Hz
	Low cut-off frequency	<100	0.46	Hz
Components	R_1	10	10	$k\Omega$
	C_1	1	1	μF
	R_2	350	330	$k\Omega$

Table F.1: Input signal adaptation circuit specifications

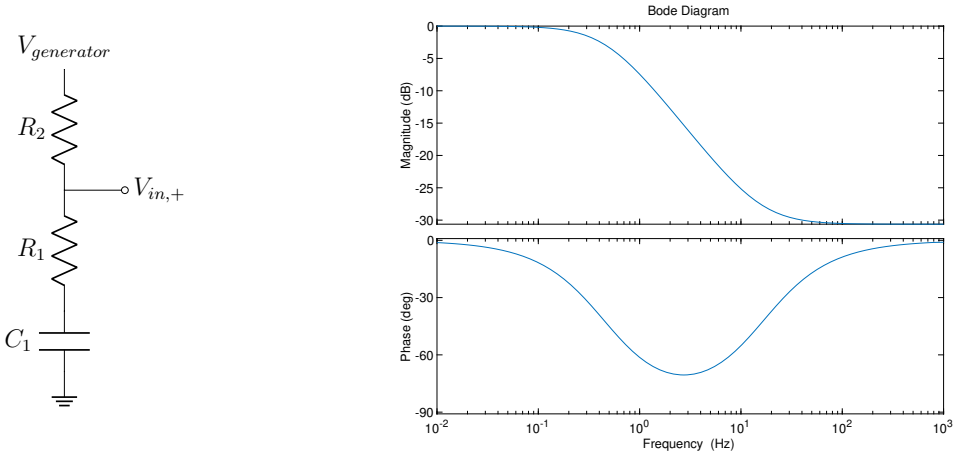

Figure F.2: Input Voltage adaptation circuit and the corresponding bode diagram.

Next to this input voltage adaptation, two voltage sources have to be fixed: the V_{DD} voltage at 1.8V and the V_{ref} voltage. Since 2 of the 3 voltage sources are already used, those 2 voltages have to be fixed with the SMU. Since the 2 sources are continuous voltages, they can be fixed with a voltage divider. To avoid interference with the rest of the circuit, the voltage divider is combined with a voltage follower (see Figure F.3). This way, the voltages over the circuit do not interfer with the reference voltage. Since resistances in the $M\Omega$-range are used in the circuit, the voltage follower allows us to use resistances of 330 $k\Omega$ for the voltage divider.

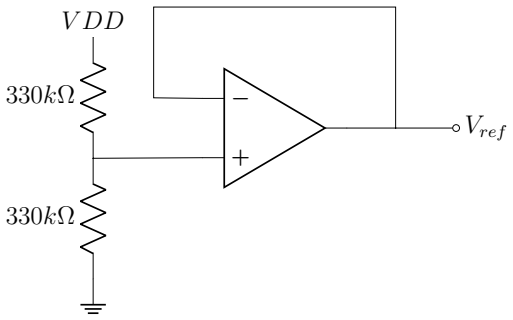

Figure F.3: Voltage reference circuit

F.1.1 Measure sheme

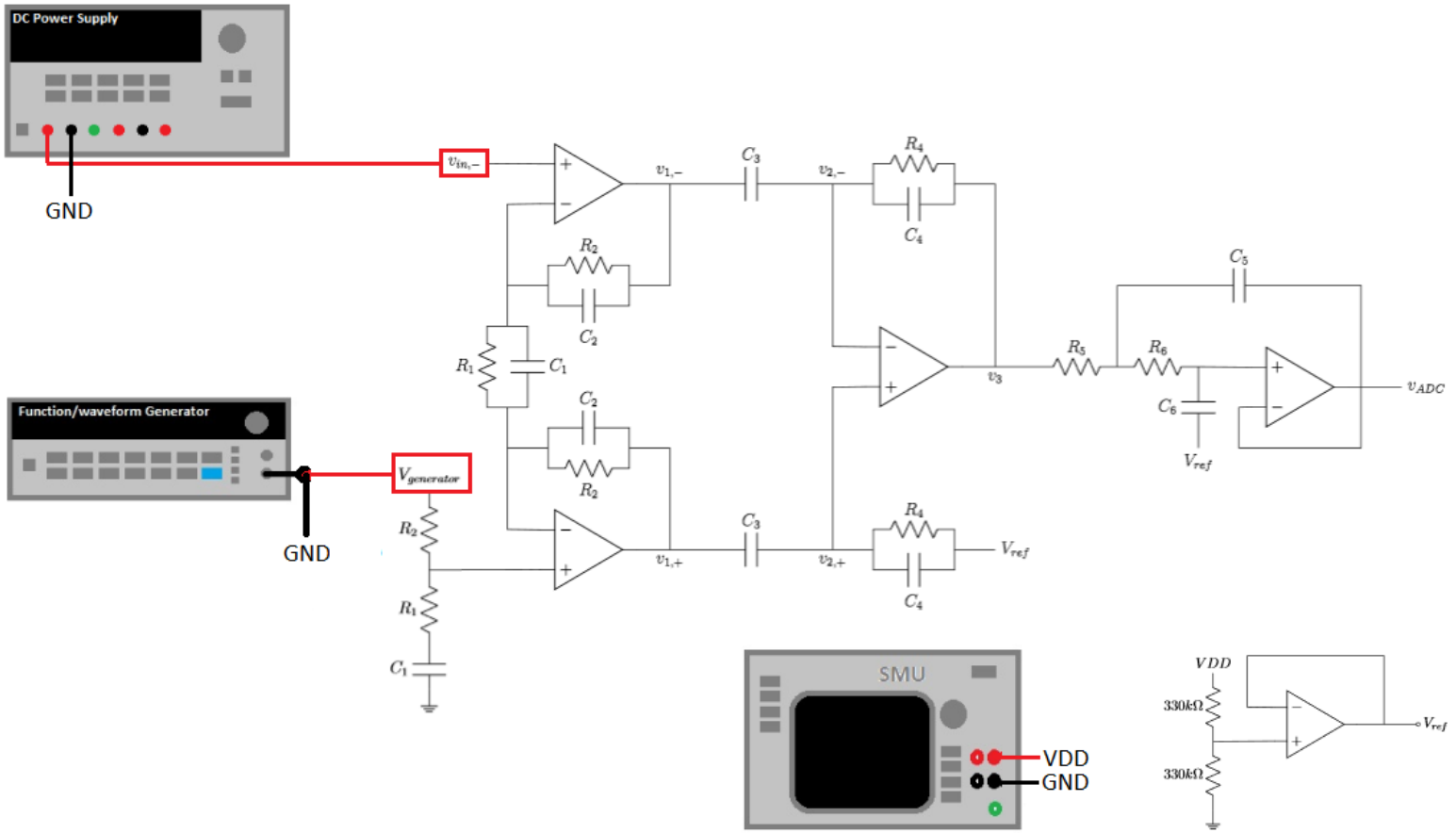

Figure F.4: Measurment scheme containing the adapted circuit, the DC power supply, the waveform generator and the SMU.

F.2 Measure of the signals at different points of the circuit.

This subsection compares the measured signals (with the oscilloscope) with the signals simulated in LT-spice. First the input signals are analysed, then the signals at different places inside the circuit are compared and finally a bode diagram compares the measured output signal and the simulated output signal at different frequencies. The measurement scheme is given on Figure F.4

F.2.1 Input signals

Concerning the inputs, the first comparison is done between the waveform generator ($V_{generator}$) and the $v_{in,+}$-signal in Figure F.5 (The circuit with the indication of $V_{generator}$ and $v_{in,+}$ are given on Figure F.2).

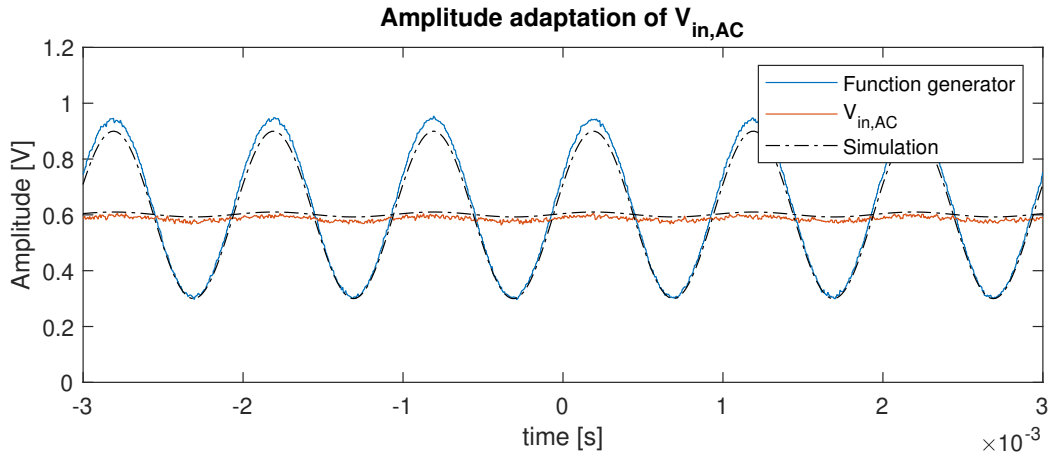

Figure F.5: Circuit measures compared to LT-spice simulation of the adaptation of the input amplitude between the voltage generator and the positive input of the instrumentation amplifier. The amplitude of the waveform generator is fixed at 300mV, the amplitude of the signal at 8.3mV and the offset at 0.6V. As expected, the offset is kept while the signal amplitude is divided by 34.

The input signals $v_{in,+}$ and $v_{in,-}$ are shown on Figure F.6 each subfigure represents one input signal $v_{in,+}$ or $v_{in,-}$ each of them at the inverting and non-inverting input of the corresponding operational amplifiers (see on the global circuit on Figure 4.2).

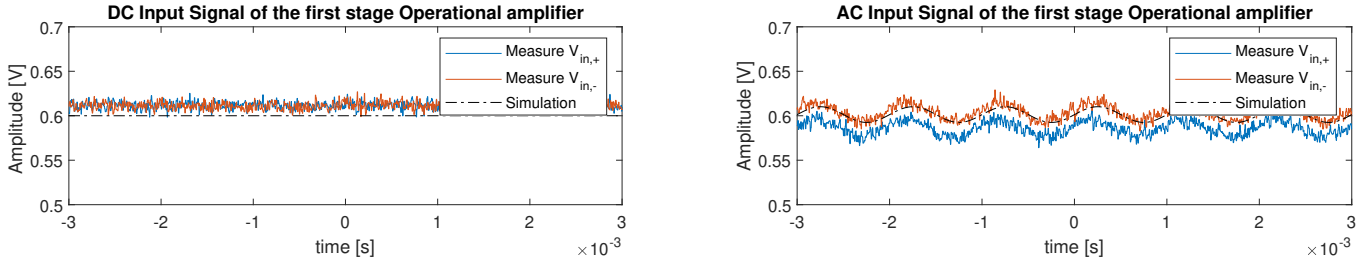

Figure F.6: Input of the first stage operational amplifiers compared to the non-inverting inputs and the LT-spice simulations. This is done in orther to verify if the input signal is well copied at the $v_{in,-}$ input of the two differential amplifiers. On the right figure, an offset is present between the two inputs of the differential amplifiers for example.

F.2.2 Signal comparison inside the circuit

In order to verify the good working of the circuit signals obtained at different points in the circuit are compared to the signals obtained with the LT-spice simulation. Referring to the circuit on Figure 4.2, the measured signals are $v_{1,+}$, $v_{1,-}$, $v_{2,+}$, $v_{2,-}$ and v_3. The signals are shown compared with the LT-Spice simulation on Figure F.7.

The first graph shows the output of the input buffers ($v_{1,+}$ and $v_{1,-}$), the second graph shows the signals at the two inputs of the differential amplifier ($v_{2,+}$ and $v_{2,-}$). The feedback loop ensures that both signals are equal. The third graph shows the output of the differential amplifier together with the measures of VDD and V_{ref}.

It is interesting to compare the results with the mathematical expressions computed in subsection H.1. First $v_{1,-}$ and $v_{1,+}$ were expressed in function of $v_{in,-}$ and $v_{in,+}$:

$$v_{1,-} = -\frac{Z_2}{Z_1}(v_{in,+} - v_{in,-}) + v_{in,-} \tag{F.2}$$

$$v_{1,+} = \frac{Z_2}{Z_1}(v_{in,+} - v_{in,-}) + v_{in,+} \tag{F.3}$$

Equations F.3 and F.2 amplify $v_{in,+} - v_{in,-}$ with a gain fixed by $\frac{Z_2}{Z_1}$. At $1kHz$, following approximation may be done:

$$\frac{Z_2}{Z_1} = \frac{R_2}{R_1}\frac{1 + j\omega R_1 C_1}{1 + j\omega R_2 C_2} \approx \frac{C_1}{C_2} = 7,02 \tag{F.4}$$

Finally, $v_{in,-}$ and $v_{in,+}$ are respectively added, this contributes to the offset of 0.6 V on both signals and also explains the fact that the amplitudes two signals are not approximately and not perfectly symmetric.

By using equations H.1,H.2,H.4 and H.3, $v_{2,+}$ and $v_{2,-}$ can be computed in function of $v_{in,+} - v_{in,-}$.

$$v_{2,+} = \frac{Z_4}{Z_3 + Z_4}\frac{Z_2}{Z_1}(v_{in,+} - v_{in,-}) + \frac{Z_4}{Z_3 + Z_4}v_{in,+} + \frac{Z_3}{Z_3 + Z_4}V_{ref} \tag{F.5}$$

$$v_{2,-} = \frac{Z_4}{Z_3 + Z_4}\frac{Z_2}{Z_1}(v_{in,+} - v_{in,-}) + \frac{Z_4}{Z_3 + Z_4}v_{in,+} + \frac{Z_3}{Z_3 + Z_4}V_{ref} \tag{F.6}$$

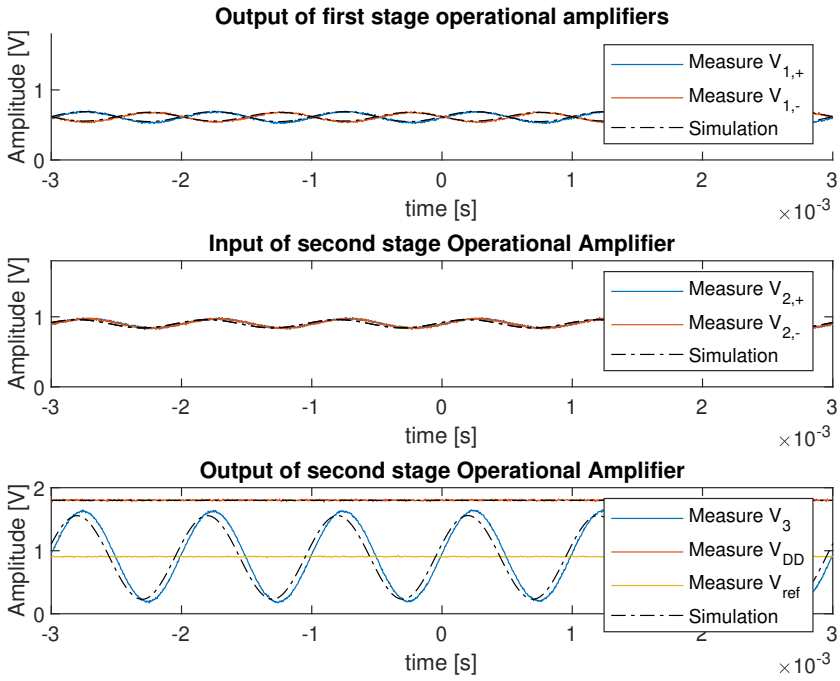

Figure F.7: Comparison between measured signals and signals simulated with LTspice. With respect to the circuit on Figure 4.2, the first graph shows $v_{1,+}$ and $v_{1,-}$, the second graph shows $v_{2,+}$ and $v_{2,-}$ and graph shows v_3 together with VDD and V_{ref}.

Equations F.5 and F.6 amplify $v_{in,+} - v_{in,-}$ at a frequency of $1kHz$ with a gain of:

$$\frac{Z_4}{Z_3+Z_4}\frac{Z_2}{Z_1} = \frac{1+j\omega C_4 R_4}{1+j\omega(C_3+C_4)R_4}\frac{R_2}{R_1}\frac{1+j\omega R_1 C_1}{1+j\omega R_2 C_2} \approx \frac{C_3}{C_3+C_4}\frac{C_1}{C_2} = 5.83 \qquad \text{(F.7)}$$

The offset can be expressed in function of $v_{in,+}$ (= 0.6V) and V_{ref} (=0.9).

$$\frac{Z_4}{Z_3+Z_4}v_{in,+} + \frac{Z_3}{Z_3+Z_4}V_{ref} = \underbrace{\frac{j\omega C_3 R_4}{1+j\omega(C_3+C_4)R_4}}_{\approx 0 \text{ for DC-signal}} v_{in,+} + \underbrace{\frac{1+j\omega C_4 R_4}{1+j\omega(C_3+C_4)R_4}}_{\approx 1 \text{ for DC-signal}} V_{ref} \approx V_{ref} \qquad \text{(F.8)}$$

The v_3 equation was already written in function of $v_{in,-} - v_{in,+}$ and V_{ref}:

$$v_3 = \underbrace{\frac{2Z_2+Z_1}{Z_1}}_{\text{IB}}\underbrace{\frac{Z_4}{Z_3}}_{\text{DA}}(v_{in,+} - v_{in,-}) + V_{ref} \qquad \text{(F.9)}$$

Appendix G

Operational Amplifier criteria details

The choice of the differential amplifier is done on a serie of criteria. Those criteria are detailed in the following points. Then a comparison table has been made to chose the best suited amplifier.

- Minimum supply Voltage Range: since the ADC requirements work at least in a voltage range of 1.8 V, the lowest supply voltage of the amplifiers is 1.8 V. The closest the supply voltage of the amplifiers is of 1.8V, the less power it needs.
- Slew rate: the minimal value of the slew rate is computed as follow:

  $$\text{Slew rate} = 2\pi f V$$

  Where f represents the maximum frequency (12kHz) and V represents the maximum voltage peak (1.52V - 0.28 V) [79].

  $$\text{Slew rate} = 0.0935 V/\mu s$$

- Input impedance: The output impedance of the Instrumentation amplifier is $139k\Omega$. In order to avoid a huge voltage drop at the output of the instrumentation amplifier, a non-inverting amplification configuration has been chosen. Nevertheless, the input impedance has to be large enough to maintain this advantage of the non-inverting amplifier.
- Maximum noise Density: in order to avoid a to large input referred noise, knowing that the neural signal remains in the μV range, 0.1 μV has been chosen as limit. For this amount of input referred noise combined with a second pole low-pass filter, the maximum noise density is computed in the following equations:

$$V_{rms} = \text{Noise Density}[V/\sqrt{Hz}] \cdot \sqrt{f \cdot 1.22} \quad \text{(G.1)}$$

$$\text{Noise Density}[V/\sqrt{Hz}] = \frac{V_{rms}}{\sqrt{f \cdot 1.22}} \quad \text{(G.2)}$$

$$= 52.75 nV/\sqrt{Hz} \quad \text{(G.3)}$$

- Gain bandwith: for the chosen analog amplifier implementation (with 2 stages and DISO configuration), the maximum Gain is of 15. The corresponding gain bandwidth is 180 kHz.

$$GBW = f \cdot Gain \tag{G.4}$$
$$= 180kHz \tag{G.5}$$

  To amplify the signal with only one amplifier stage, the gain bandwidth should be 10 times larger.

- Package: in order to test the analog amplifier on a breadboard, the package must be a DIP. This constraint eliminates a lot of low power operational amplifiers. For an implementation on PCB, this constraint can be removed and a better amplifier can be found. Moreover, the analysed operational amplifiers are the ones who are available on Farnell. For real implementation, other providers with more specific and adapted operational amplifiers can be found.

Appendix H

Discrete IA

H.1 Equations Instrumentation amplifier

In order to have a clear view on the impact of the different stages, it is interesting to first compute the transfer function $\frac{v_3}{(v_{in,+}-v_{in,-})}$ and then to discuss the different gain levels.

First $v_{1,-}$ and $v_{1,+}$ are computed in function of $v_{in,-} - v_{in,+}$:

$$v_{1,-} = \frac{Z_2}{Z_1}(v_{in,-} - v_{in,+}) + v_{in,-} \tag{H.1}$$

$$v_{1,+} = \frac{Z_2}{Z_1}(v_{in,+} - v_{in,-}) + v_{in,+} \tag{H.2}$$

Then $v_{2,+}$ and $v_{2,-}$ can be computed in function of $v_{1,-}$, $v_{1,+}$, v_3 and V_{ref}:

$$v_{2,+} = \frac{Z_4}{Z_3 + Z_4}v_{1,+} + \frac{Z_3}{Z_3 + Z_4}V_{ref} \tag{H.3}$$

$$v_{2,-} = \frac{Z_4}{Z_3 + Z_4}v_{1,-} + \frac{Z_3}{Z_3 + Z_4}v_3 \tag{H.4}$$

Considering the operational amplifier's gain as ideal, the signals $v_{2,+}$ and $v_{2,-}$ have the same value. By combining the equations H.1,H.2,H.4 and H.3, v_3 can be expressed in function of $v_{in,-} - v_{in,+}$. The equation can be splitted in 2 parts: the input buffer (IB) and the differential amplifier (DA):

$$v_3 = \underbrace{\frac{2Z_2 + Z_1}{Z_1}}_{\text{IB}}\underbrace{\frac{Z_4}{Z_3}}_{\text{DA}}(v_{in,+} - v_{in,-}) + V_{ref} \tag{H.5}$$

H.2 Input buffer

Input buffer stage (see equation H.5) is a non-inverting amplification stage. This means that the gain of the signal can not be bellow one for whatever frequency. Supposing that Z_1 and Z_2 are both composed of resistors and/or capacitors, this purpose is verified by the following equation:

$$\frac{2Z_2 + Z_1}{Z_1} \geq 1 \tag{H.6}$$

		Target value or target range	Obtained value	Unit
Target specifications	high frequency gain	15	15.04	V/V
	low frequency gain	1-2	1.54	V/V
	high frequency cut-off frequency	100 - 150	125.4	Hz
	low frequency cut-off frequency	< 100	12.8	Hz
Components	R_1	11.29	10	$M\Omega$
	C_1	3.29	3.3	nF
	R_2	2.82	2.7	$M\Omega$
	C_2	0.47	0.47	nF

Table H.1: Input buffer specifications and choice of the components.

By putting a capacitor and a resistor in parallel for Z_1 and Z_2, two cut-off frequencies as wel as the gain levels can be fixed. The transfer function becomes:

$$\frac{2Z_2 + Z_1}{Z_1} = \frac{2R_2 + R_1}{R_1} \frac{j\omega(2C_1 + C2)R_2 \frac{R_1}{2R_2+R_1} + 1}{j\omega R_2 C_2 + 1} \tag{H.7}$$

From this equation some specifications can be determined:

- the high frequency gain is fixed by $\frac{2C_1+C_2}{C_2}$
- the low frequency gain is fixed by $\frac{2R_2+R_1}{R_1}$
- the low frequency cut-off frequency is fixed by $\frac{2R_2+R_1}{2\pi(2C_1+C_2)R_2R_1}$
- the high frequency cut-off frequency is fixed by $\frac{1}{2\pi R_2 C_2}$

H.3 Differential amplifier

The differential amplifier is determined by Z_3 and Z_4 (see equation H.5). If the filter introduced by the differential amplifier level is a low-pass filter, the low-frequency (containing the artefacts) will furter be amplified by the chosen gain. This is why a second high-pass filter is configured.

$$\frac{Z_4}{Z_3} = \frac{j\omega C_3 R_4}{1 + j\omega C_4 R_4} \tag{H.8}$$

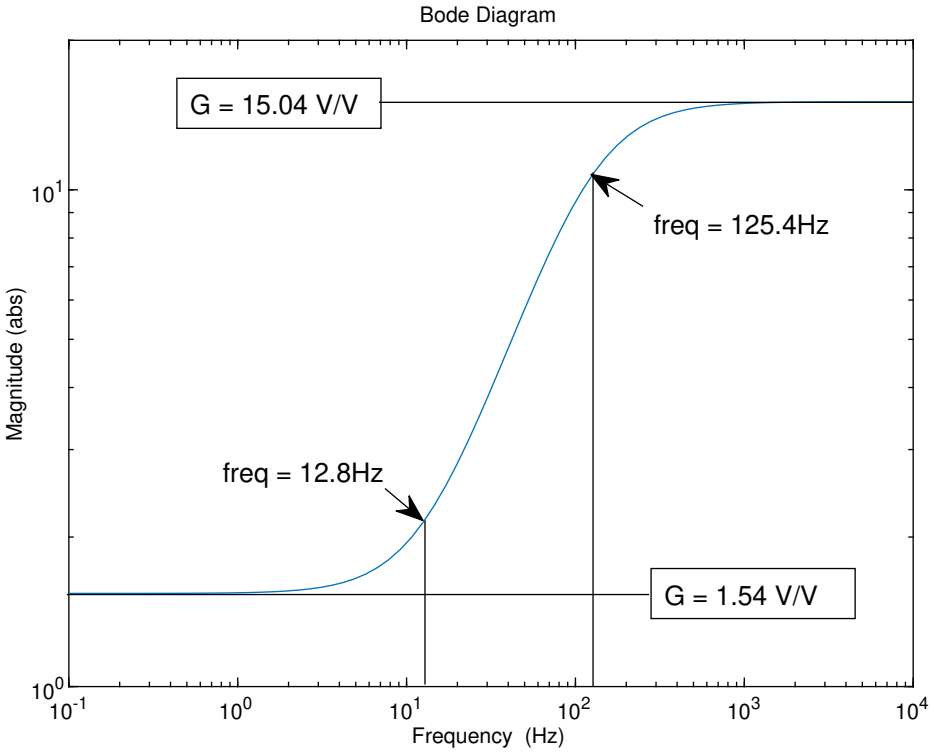

Figure H.1: Bode diagram of the Input Buffer transfer function

From this equation some specifications can be determined:

- the AC-gain is fixed by $\frac{C_3}{C_4}$
- the AC cut-off frequency is fixed by $\frac{1}{2\pi R_2 C_2}$

		Target value or target range	Obtained value	Unit
Target specifications	high frequency gain	5	5	V/V
	high frequency cut-off frequency	100 - 200	159	Hz
Components	C_3	5	5	nF
	R_4	1	1	$M\Omega$
	C_4	1	1	nF

Table H.2: Differential amplifier specifications and choice of the components.

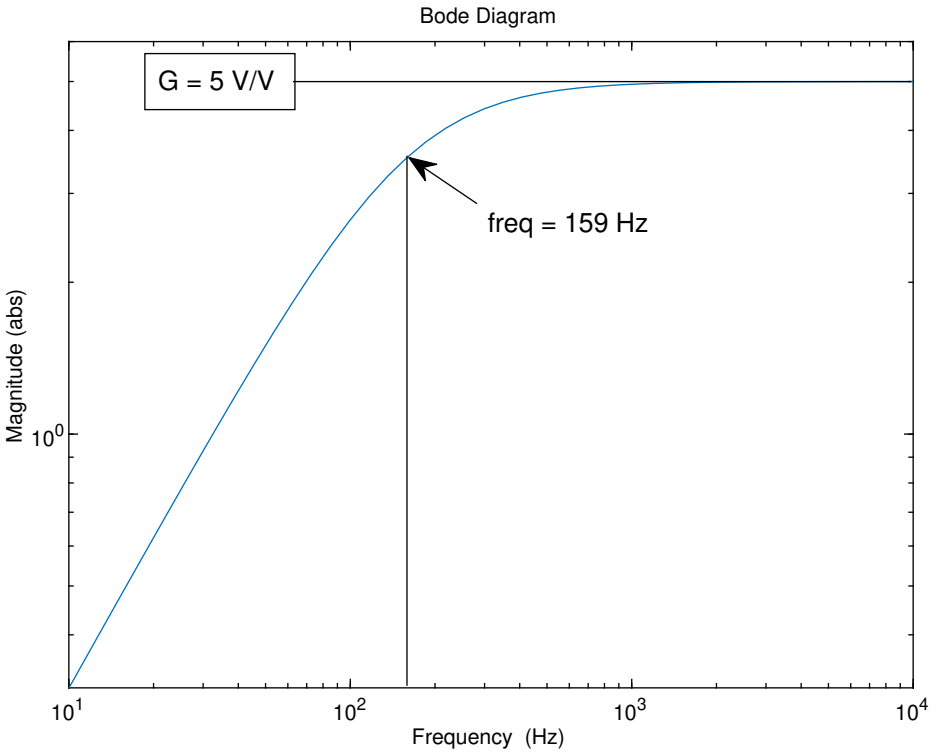

Figure H.2: Bode diagram of the Differential Amplifier transfer function

		Target value or target range	Obtained value	Unit
Target specifications	cut-off frequency	12	13.2	kHz
Components	R_5	1.1	1.2	$M\Omega$
	C_5	10	10	nF
	R_6	1.1	1.2	$M\Omega$
	C_6	10	10	nF

Table H.3: Sallen Key specifications and choice of the components.

H.4 Equations Sallen Key low pass filter

To limit the noise addition at frequencies who are much larger than the signal, a 2 pole sallen key low-pass filter is added to the circuit. Concerning the sallen key implementation, the result of the computation of V_{ADC} in function of v_3 and V_{ref} is given by:

$$V_{ADC} = \frac{1}{1 + j\omega C_6(R_5 + R_6) + j\omega C_5 C_6 R_5 R_6} v_3 + \frac{j\omega C_6(R_5 + R_6) + j\omega C_5 C_6 R_5 R_6}{1 + j\omega C_6(R_5 + R_6) + j\omega C_5 C_6 R_5 R_6} V_{ref} \quad \text{(H.9)}$$

By replacing v_3 by equation H.5, V_{ADC} can be written in function of $v_{in,+} - v_{in,-}$ and V_{ref}:

$$V_{ADC} = \frac{1}{1 + j\omega C_6(R_5 + R_6) + j\omega C_5 C_6 R_5 R_6} \frac{2Z_2 + Z_1}{Z_1} \frac{Z_4}{Z_3}(v_{in,+} - v_{in,-}) + V_{ref} \quad \text{(H.10)}$$

Equation H.10 shows that the final result is an amplification of $v_{in,+} - v_{in,-}$ and an addition of a continuous V_{ref} voltage. The signal at the input of the microcontroller had to be centered around 0.9V. This is why V_{ref} is fixed at that value. The transfer function linked to the sallen key filter is:

$$\frac{1}{1 + j\omega C_6(R_5 + R_6) + j\omega C_5 C_6 R_5 R_6} \quad \text{(H.11)}$$

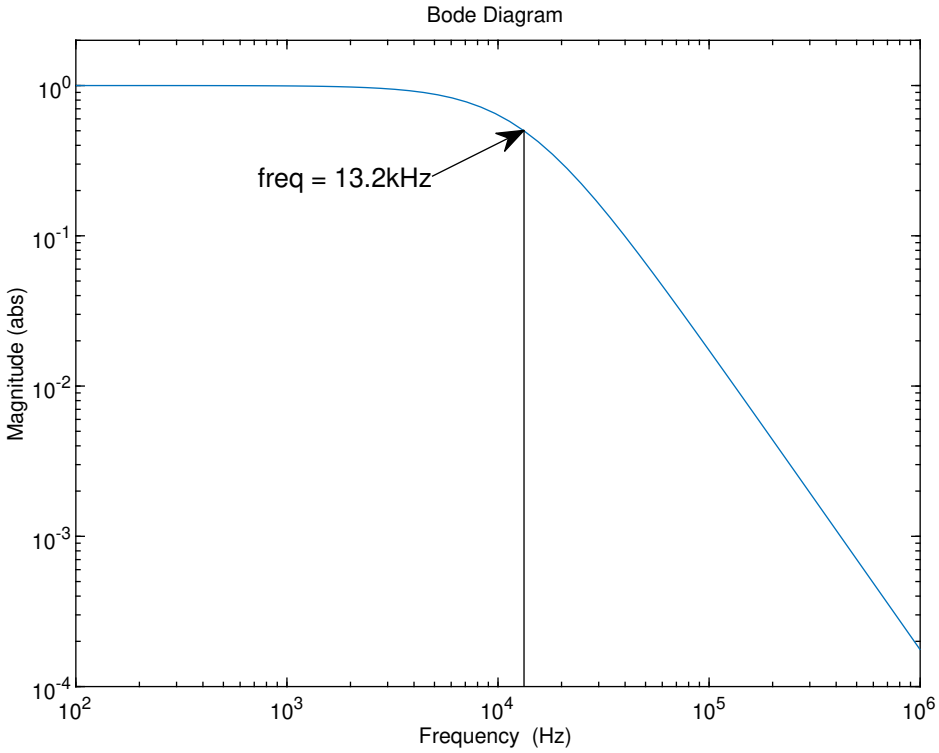

Figure H.3: Bode diagram of the Sallen Key low pass filter transfer function

UNIVERSITÉ CATHOLIQUE DE LOUVAIN
École polytechnique de Louvain
Rue Archimède, 1 bte L6.11.01, 1348 Louvain-la-Neuve, Belgique | **www.uclouvain.be/epl**